NASA

Technical Memorandum 83917

PULSED MULTIWAVELENGTH LASER RANGING SYSTEM

J. B. Abshire

MARCH 1982

National Aeronautics and Space Administration

Goddard Space Flight Center
Greenbelt, Maryland 20771

PULSED MULTIWAVELENGTH LASER RANGING SYSTEM

by
James Brice Abshire

Dissertation submitted to the Faculty of the Graduate School
of the University of Maryland in partial fulfillment
of the requirements for the degree of
Doctor of Philosophy
1982

ABSTRACT

Title of Dissertation: Pulsed Multiwavelength Laser Ranging System

James Brice Abshire, Doctor of Philosophy, 1982

Dissertation directed by: Leonard S. Taylor, Professor, Department of Electrical Engineering

A pulsed multiwavelength laser ranging system for measuring atmospheric delay has been built and tested, and its theoretical performance limits have been calculated. The system uses a dye-modelocked ND:YAG laser, which transmits 70 psec wide pulses simultaneously at 1064, 532, and 355 nm. The differential delay of the 1064 and 355 nm pulses is measured by a specially calibrated waveform digitizer to estimate the dry atmospheric delay. The delay time of the 532 nm pulse is used to measure the target distance. Static crossed-field photomultipliers are used as detectors for all wavelengths.

Theoretical analysis shows that path curvature and atmospheric turbulence are fundamental limits to the ranging accuracy of both single and multicolor systems operating over horizontal paths. For two color systems, an additional error is caused by the uncertainty in the path averaged water vapor. The standard deviation of the multicolor instrument's timing measurements is shown to be directly proportional to the laser pulse width plus photomultiplier jitter divided by the square root of the received photoelectron number. The prototype system's maximum range is calculated to be 25 km, which is limited by atmospheric and system transmission losses at 355 nm. System signal detection and false-alarm calculations are also presented.

Multicolor ranging measurements over round-trip horizontal path lengths of 193, 921, and 4760 m show occasional receiver biases as large as 80 psec. These biases are caused by

optical spot misadjustments in the receiver. More typical receiver biases of 10 to 15 psec cause atmospheric delay prediction errors at the 1.5 to 2cm level. A redesign of the receiver optics is expected to reduce these bias errors to 5 psec, which will result in an atmospheric delay prediction error of less than 1 cm. Several suggestions for future work and applications for the modified system are discussed.

TABLE OF CONTENTS

CONTENTS (Continued)

LIST OF TABLES

LIST OF TABLES (Continued)

LIST OF FIGURES

LIST OF FIGURES (Continued)

LIST OF FIGURES (Continued)

LIST OF FIGURES (Continued)

ACKNOWLEDGEMENTS

I would like to express sincere thanks to Prof. Leonard S. Taylor of the Department of Electrical Engineering, University of Maryland for his generous guidance of this research.

Since 1971, I have been very fortunate to have been associated with many talented and inspiring people in the Electro-Optics Branch of NASA's Goddard Space Flight Center. Dr. Michael W. Fitzmaurice first introduced my dissertation topic to me, and since then has been a very valuable source of knowledge and encouragement. Dr. Jack L. Bufton contributed encouragement, his detailed knowledge of atmospheric turbulence, as well as many helpful suggestions for this research. Dr. John J. Degnan also contributed encouragement, and his knowledge of lasers and optics. I am also very grateful to Mr. H. Edward Rowe for the contributions he made to the experimental phase of this research.

Mr. David E. Kotecki of Lawrence-Livermore Laboratories, made many important contributions to the early experimental phase and to the early computer software of the instrument while he was a Co-op student at Goddard. The talented contributions made by Ms. Leslie E. Fuhr of the Laboratory for Physical Sciences, while she worked at Goddard were indispensable in developing the numerous minicomputer programs for the experiment.

It is also a pleasure to acknowledge the many helpful conversations I have had with both Dr. Moody C. Thompson, Jr., of Cripple Creek Colorado, and Dr. George M. Resch of the Jet Propulsion Laboratory. Their expertise and detailed knowledge of atmospheric refraction influenced many areas of this research.

Most of all, I would like to thank my wife, Jean. Throughout the years of part-time and weekend study required to earn my graduate degrees, her encouragement, support, sense-of-humor, and understanding have been invaluable.

CHAPTER 1

INTRODUCTION AND SUMMARY

Many applications in surveying, geophysical research, and positioning require accurate long distance measurements. Since the delay times of optical or microwave signals are used to infer the distance, atmospheric refraction is a limiting error source for all these applications. For example, in NASA's satellite laser ranging systems [1.1], the uncorrected atmospheric refractive delays cause an error of 2.6 m at zenith, and 7.8 m at an elevation angle of 20 degrees. These errors can be reduced to approximately 2 cm at 20 degrees by using atmospheric refraction models [1.2], [1.3]. This residual error has become a dominant one in the system error budget with recent improvements in ranging instrumentation [1.4].

There is considerable interest in developing instrumentation which can improve the estimates of atmospheric delay in both ground-based and in ground-to-space applications. This improvement can occur either by using the instrumentation to directly estimate the atmospheric delay in each measurement, or by making representative delay measurements, which then can be used to improve atmospheric delay models.

The technique of using atmospheric dispersion to estimate atmospheric delay was first proposed by Bender and Owens [1.5]. Since then several continuous wave (cw) dual-wavelength systems using this principle have been built for operating over horizontal paths [1.6], [1.7]. However, these systems have had limited distance capability and cannot be used over quickly changing paths. Three-wavelength cw systems have used two optical colors and a microwave 'color' to measure both the dry delay and the 'wet' delay caused by the water vapor in the path [1.8]. Unfortunately, the larger angular width of the microwave beam makes the wet delay determination susceptible to multipath errors from the ground reflection.

Pulsed optical multiwavelength systems do not have these constraints. High power, mode-locked laser transmitters are convenient sources of short (70 psec) pulses. Part of this energy can be converted to shorter wavelengths by using nonlinear optical crystals. The resulting pulses of differing wavelengths can be used with fast optical detectors and timing electronics to measure the atmospheric delay over long atmospheric paths. Since doppler effects are negligible with direct-detection receivers, pulsed systems are very insensitive to target motion. Preliminary work on pulsed multi-wavelength systems recently has been reported [1.9], [1.10]. However, no detailed analysis of theoretical or actual system performance yet has been given.

A pulsed multi-color laser ranging system has been built, and its performance over horizontal paths has been analyzed for this dissertation. First, the physical principles which cause refractive atmospheric delays are reviewed in Chapter 2. The resulting Lorentz-Lorenz equation expresses the relationship between gas density and refractive index. The refractive properties of gas mixtures then are reviewed, and the measured indices and densities of the gases which compose air are used to compute its phase refractive index. This result then is extended to compute the group refractive index of air.

The theories of single and multiwavelength ranging systems operating over horizontal paths are derived in Chapter 3. The results show that the dominant atmospheric error source in single wavelength systems is the error in estimating the integrated path temperature. Other error sources are path curvature and turbulence. Three color systems are found to require approximately thirty times more accurate differential delay estimates than two-color systems, when using the wavelengths of the prototype system. Limiting error sources for three-color systems are shown to be path curvature and turbulence. Two-color systems have these same errors, as well as errors in estimating integrated path water vapor. However, they require much less accurate differential delay measurements than three color systems.

In Chapter 4, the prototype pulsed multicolor system is described. The laser transmitter is a dye-modelocked ND:YAG, whose 70 psec wide output pulse at 1064 nm is both frequency doubled and tripled. The 355 and 1064 nm pulses are used to measure the atmospheric delay in the system, while the 532 nm pulse is used to measure the distance to the target corner reflector. Static crossed-field photomultipliers are used as detectors for all colors. A specially calibrated waveform digitizer is used to measure the differential delay between the 355 and 1064 nm pulses caused by dispersion in the atmospheric path. A photodiode, discriminators, and a time-interval unit are used to measure the 532 nm path delay.

In Chapter 5, the single-measurement accuracy of ideal pulsed ranging systems is shown to be directly proportional to the laser pulse width, and inversely proportional to the square root of the number of received photoelectrons on each laser firing. These results then are extended to the technique of recovering the atmospheric delay from subtracting averaged sets of reference and atmospheric path measurements. This method is used in the prototype system. Subsequent analysis includes the effects of the timing biases and jitters contributed by the photomultipliers and waveform digitizer in the prototype system. Calculation of the signal detection and false-alarm probabilities also are presented, along with calculations of the maximum range of the prototype system.

The measured performance of the prototype system is reviewed in Chapter 6. System measurements of the dispersive atmospheric delay in three horizontal paths show that bias errors as large as 80 psec occur when the optical beam in the receiver is not carefully adjusted. When properly adjusted, the biases are reduced to the 10 to 15 psec level. Suboptimum magnetic-field conditions within the detectors are postulated as the cause of the receiver's sensitivity to the optical spot position. This condition also causes an increase in the detector's single photoelectron jitter to 100 psec, which is three times larger than when the detectors are correctly biased. Measurements of the single-dependent system jitter confirm the theoretical receiver model. The residual system bias is 5 psec, which is the bias level of the calibrated waveform digitizer.

In Chapter 7, several suggestions are made for future theoretical and experimental research. They include extending both the ranging theory to include multipath effects and the detection probability calculations to include laser energy fluctuations. Further suggestions are to modify the prototype system to alleviate the detector problem and to minimize misalignments and motions between the reference and atmospheric path optical beams. Once these are completed, the prototype system should have sufficient accuracy for 1 cm atmospheric delay measurements. Such a system then could be used to verify the ranging theory.

The modified prototype system should be useful in several applications. They include length measurements of extended horizontal paths which are used for geophysical monitoring. Another use is for measuring the atmospheric delay over slant paths to airborne targets. With cube-corner reflectors mounted on weather balloons or high altitude aircraft, these measurements could be used to investigate the accuracy of atmospheric delay models currently used in satellite laser ranging systems.

Chapter 1 References

1.1 M. W. Fitzmaurice, "Ground-Based and Space-Based Laser Ranging Systems," NASA Technical Paper 1149, (Jan. 1978).

1.2 J. W. Marini and C. W. Murray, Jr., "Correction of Laser Range Data for Atmospheric Refraction at Angles above 10 Degrees," NASA X-Document 591-73-351 (Nov. 1973).

1.3 C. S. Gardner, Appl. Opt., Vol. 16, 2427 (1977).

1.4 T. W. Zagwodzki, H. E. Rowe, J. J. Degnan, and D. A. Premo, "Mobile Laser Upgrade Tests," Presented at the Fourth Annual Conf. on the NASA Geodynamics Program, Greenbelt, MD (Jan. 1982).

1.5 P. L. Bender and J. C. Owens, J. Geophys. Res., Vol. 70, 2461 (1965).

1.6 K. B. Earnshaw and J. C. Owens, IEEE J. Quantum Electron., Vol. QE-3, 544 (1967).

1.7 M. C. Thompson Jr., J. Geophys. Res., Vol. 73, 3097 (1968).

1.8 L. E. Slater and G. R. Huggett, J. Geophys. Res., Vol. 81, 6299 (1976).

1.9 B. Querzola, Appl. Opt., Vol. 18, 3055 (1979).

1.10 J. B. Abshire, Appl. Opt., Vol. 19, 3436 (1980).

CHAPTER 2

THE REFRACTIVE PROPERTIES OF AIR

In this chapter the propagation characteristics of an electro-magnetic field through a medium consisting of a single gas will be reviewed. This review will follow the general outline given in Born and Wolf [2.1]. These results then will be generalized for a substance which is a mixture of individual gases, such as air. Next, a formula for the refractive index of air will be derived from these results and the measured indices and densities of the atmospheric gases. The phase velocity will be shown to depend on the index of refraction of the medium, and the relationship between the index and the number density of the molecules will be derived. Finally, a general formula will be derived for the group refractivity of air which can be used with measurements of temperature (T), total pressure (P), and relative humidity (Rh).

2.1 Electromagnetic Vector and Scalar Potentials

In atomic theory, matter is assumed to be composed of interacting atoms and molecules embedded in a vacuum. The local electromagnetic fields produced by these atoms and molecules have large variations. However, the internal atomic and molecular fields are modified by externally applied ones, and the average electromagnetic properties of the material can be derived by spatially averaging the sum of the externally applied and the local fields.

As long as the averaging region is large with respect to the particle dimensions, the electromagnetic properties of the particles can be accurately described by considering them to be simple electric and magnetic dipoles. Since the atoms and molecules are polarizable, most substances show these electric and magnetic moments only under the influence of externally applied fields. For the gas molecules considered in this chapter, the induced moments are linearly related to the polarizing component of the incident field. For materials in general, however, the moment vector does not always coincide with the direction of the field.

The vector and scalar potentials of an electromagnetic wave can be reviewed by starting with Maxwell's Equations,

$$\nabla \times \underline{E} = -\partial \underline{B}/\partial t, \tag{2.1}$$

$$\nabla \times \underline{H} = \underline{j} + \partial \underline{D}/\partial t, \tag{2.2}$$

$$\nabla \cdot \underline{D} = \rho, \tag{2.3}$$

and

$$\nabla \cdot \underline{B} = 0. \tag{2.4}$$

The electric displacement and magnetic induction also can be defined by

$$\underline{D} \equiv \epsilon_0 \underline{E} + \underline{P} \tag{2.5}$$

and

$$\underline{B} \equiv \mu_0 (\underline{H} + \underline{M}). \tag{2.6}$$

By using the above equations and simplifying,

$$\nabla \cdot \underline{E} = \rho'/\epsilon_0,$$

and

$$\nabla \times \underline{B} - \mu_0 \epsilon_0 \frac{\partial \underline{E}}{\partial t} = \mu_0 \underline{j}. \tag{2.7}$$

Here the modified charge and current densities are defined by

$$\rho' \equiv \rho - \nabla \cdot \underline{P}$$

and

$$\underline{j}' \equiv \underline{j} + \frac{\partial \underline{P}}{\partial t} + \nabla \times \underline{M}. \tag{2.8}$$

Now if the vector and scalar potentials $\underline{A}$ and ϕ are defined by

$$\underline{B} \equiv \nabla \times \underline{A} \tag{2.9}$$

and

$$\underline{E} \equiv -\nabla \phi - \frac{\partial \underline{A}}{\partial t}, \tag{2.10}$$

and the Lorentz Gauge is chosen, then

$$\nabla \cdot \underline{A} + \mu_0 \epsilon_0 \frac{\partial \phi}{\partial t} = 0. \tag{2.11}$$

Furthermore, $\underline{A}$ and ϕ must satisfy the inhomogeneous wave equations

$$\nabla^2 \underline{A} - \mu_0 \epsilon_0 \frac{\partial^2 \underline{A}}{\partial t^2} = -\mu_0 \underline{j} \tag{2.12}$$

and

$$\nabla^2 \phi - \mu_0 \epsilon_0 \frac{\partial^2 \phi}{\partial t^2} = -\rho'/\epsilon_0. \tag{2.13}$$

These conditions are consistent provided that $\partial \rho'/\partial t + \nabla \cdot \underline{j} = 0$.

The solutions to (2.12) and (2.13) are

$$\underline{A}(\underline{r}, t) = \frac{\mu_0}{4\pi} \int_V \frac{[\underline{j}']}{R} \, dv' \tag{2.14}$$

and

$$\phi(\underline{r}, t) = \frac{1}{4\pi\epsilon_0} \int_V \frac{[\rho']}{R} \, dv'. \tag{2.15}$$

In these equations, $[\underline{j}'] = \underline{j}'(\underline{r}', t - R/C)$ and $[\rho'] \equiv \rho'(r', t - R/C)$, and the square brackets indicate evaluation at the retarded time $t - R/C$. Throughout this chapter, the notation is used where $\underline{r}'$ is the vector from the origin to the source point (x', y', z'), $\underline{r}$ is the vector from the origin to the field point (x, y, z), and $R \equiv |\underline{r} - \underline{r}'|$.

2.2 Polarization Potentials and Dipole Fields

If the polarization potentials [2.1], [2.2] $\underline{\pi}_e$ and $\underline{\pi}_m$ are defined by

$$\underline{A} = \mu_0 \epsilon_0 \dot{\underline{\pi}}_e + \mu_0 \nabla \times \underline{\pi}_m, \tag{2.16}$$

and

$$\phi = -\nabla \cdot \underline{\pi}_e, \tag{2.17}$$

then the Lorentz condition in equation (2.13) is satisfied. Here the (˙) operator denotes differentiation with respect to time. Equations (2.12) and (2.13) also are satisfied [2.3] if $\mathbb{\pi}_e$ and $\mathbb{\pi}_m$ are chosen to satisfy the wave equations,

$$\nabla^2 \mathbb{\pi}_e - \mu_0 \epsilon_0 \ddot{\mathbb{\pi}}_e = -\mathbb{P}/\epsilon_0 \tag{2.18}$$

and

$$\nabla^2 \mathbb{\pi}_m - \mu_0 \epsilon_0 \ddot{\mathbb{\pi}}_m = -\mathbb{M}. \tag{2.19}$$

Here $\mathbb{P}$ denotes the density distribution of electric polarization and $\mathbb{M}$ is the density distribution of the magnetic moment.

The solution to these equations can be expressed in terms of the retarded electric polarization and magnetic moment by

$$\mathbb{\pi}_e = \frac{1}{4\pi\epsilon_0} \int_V \frac{[\mathbb{P}]}{R} \, dv' \tag{2.20}$$

and

$$\mathbb{\pi}_m = \frac{1}{4\pi} \int_V \frac{[\mathbb{M}]}{R} \, dv'. \tag{2.21}$$

The electric field due to the sources $\mathbb{P}$ and $\mathbb{M}$ can be found by substituting (2.16) and (2.17) into (2.10), yielding

$$\mathbb{E} = \nabla(\nabla \cdot \mathbb{\pi}_e) - \mu_0 \epsilon_0 \ddot{\mathbb{\pi}}_e - \mu_0 \nabla \times \dot{\mathbb{\pi}}_m. \tag{2.22}$$

Using a vector identity in this equation gives

$$\mathbb{E} = \nabla \times \nabla \times \mathbb{\pi}_e - \mu_0 \nabla \times \dot{\mathbb{\pi}}_m + (\nabla^2 \mathbb{\pi}_e - \mu_0 \epsilon_0 \ddot{\mathbb{\pi}}_e). \tag{2.23}$$

Now by using (2.18) and (2.23) in (2.5), the electric displacement vector can be written as

$$\mathbb{D} = \epsilon_0 \nabla \times \nabla \times \mathbb{\pi}_e - \mu_0 \epsilon_0 \nabla \times \dot{\mathbb{\pi}}_m. \tag{2.24}$$

Similarly, $\mathbb{H}$ can be found by substituting (2.16) into (2.9) and using (2.6), yielding

$$\mathbb{H} = \nabla \times \epsilon_0 \dot{\mathbb{\pi}}_e + \nabla \times \nabla \times \mathbb{\pi}_m - \mathbb{M}. \tag{2.25}$$

Now by using (2.19),

$$\underline{H} = \nabla \times (\epsilon_0 \dot{\underline{\Pi}}_e + \nabla \times \underline{\Pi}_m) + (\nabla^2 \underline{\Pi}_m - \mu_0 \epsilon_0 \ddot{\underline{\Pi}}_m). \tag{2.26}$$

Equations (2.24) and (2.26) give the field vectors $\underline{E}$ and $\underline{H}$ due to the polarization potentials $\underline{\Pi}_e$ and $\underline{\Pi}_m$. These are in turn related to the electric polarization and magnetic moment by (2.20) and (2.21).

Now consider the electric polarization from a single electric dipole located in a material at a point $\underline{r}_0$ with an orientation unit vector $\hat{n}$,

$$\underline{P}^{(d)}(\underline{r}, t) = p(t)\, \delta(\underline{r} - \underline{r}_0)\, \hat{n} \equiv \underline{p}(t)\, \delta(\underline{r} - \underline{r}_0).$$

From (2.20), the polarization potential for this dipole is

$$\underline{\Pi}_e^{(d)} = \frac{1}{4\pi\epsilon_0} \frac{\underline{p}(t - R_0/c)}{R_0}, \tag{2.27}$$

where $R_0 = |\underline{r} - \underline{r}_0|$.

Now if the remainder of the medium surrounding this dipole has no permanent electric polarization, $\underline{P} = 0$. Furthermore, if the medium has no permanent magnetic moment, $\underline{M} = 0$. From (2.21), this implies $\underline{\Pi}_m = 0$. Therefore, by using (2.27), (2.23) simplifies to

$$\underline{E}^{(d)} = \nabla \times \nabla \times \frac{1}{4\pi\epsilon_0} \frac{\underline{p}(t - R_0/c)}{R_0}. \tag{2.28}$$

In a similar way, (2.25) simplifies to

$$\underline{H}^{(d)} = \frac{1}{4\pi R_0} \nabla \times \dot{\underline{p}}(t - R_0/c). \tag{2.29}$$

These results for the fields from a single dipole will be used in the next section to derive the electromagnetic interaction of the medium with an incident wave.

2.3 Dipole Interactions with Propagating Waves

Let $\underline{E}'_j$ and $\underline{H}'_j$ be fields acting on the j^{th} dipole in the medium. These fields can be separated into the sum of the fields of the incident wave, $\underline{E}^{(i)}$ and $\underline{H}^{(i)}$, which are

propagated with phase velocity c, and the fields from all other dipoles, such that,

$$\underset{\sim}{E}'_j = \underset{\sim}{E}^{(i)} + \sum_{\ell \neq j} \underset{\sim}{E}'_{j\ell} \tag{2.30}$$

and

$$\underset{\sim}{H}'_j = \underset{\sim}{H}^{(i)} + \sum_{\ell \neq j} \underset{\sim}{H}'_{j\ell}. \tag{2.31}$$

Here the summation is extended over all dipoles in the medium except for the j^{th} one. At the point $\underset{\sim}{r}_j$, where the j^{th} dipole is located, the fields of the ℓ^{th} dipole are given by using (2.28) and (2.29), yielding

$$\underset{\sim}{E}'_{j\ell} = \underset{\sim}{\nabla}_j \times \underset{\sim}{\nabla}_j \times \underset{\sim}{p}_\ell (t - R_{j\ell}/c)/(4\pi\epsilon_0 R_{j\ell}) \tag{2.32}$$

and

$$\underset{\sim}{H}'_{j\ell} = \underset{\sim}{\nabla}_j \times \dot{\underset{\sim}{p}}_\ell (t - R_{j\ell}/c)/(4\pi R_{j\ell}). \tag{2.33}$$

Here $\underset{\sim}{p}_\ell$ denotes the dipole moment of ℓ^{th} dipole, $R_{j\ell} = |\underset{\sim}{r}_j - \underset{\sim}{r}_\ell|$, and $\nabla_j \times ( )$ is the curl operation on the j^{th} coordinate of the dipole.

If both the dipole number density and the molecular dipole moment are written as possibly discontinuous functions of $\underset{\sim}{r}$, then the total dipole moment per unit volume within the medium can be written as

$$\underset{\sim}{P}(\underset{\sim}{r}) = N(\underset{\sim}{r})\, \underset{\sim}{p}(\underset{\sim}{r}). \tag{2.34}$$

If the polarizability, α, of the medium is defined by $\underset{\sim}{p}(\underset{\sim}{r}) \equiv \alpha\epsilon_0 \underset{\sim}{E}'(\underset{\sim}{r})$, then (2.34) can be rewritten as

$$\underset{\sim}{P}(\underset{\sim}{r}) = N(\underset{\sim}{r})\, \epsilon_0\, \alpha\, \underset{\sim}{E}'(\underset{\sim}{r}). \tag{2.35}$$

The total fields at the j^{th} dipole can be given by substituting (2.32) and (2.33) into (2.30) and (2.31) respectively, and by using (2.35). The resulting summations can be re-written as integrals, since the number density is a discontinuous function of position, yielding

$$\mathbf{E}'(\mathbf{r}, t) = \mathbf{E}^{(i)} + \int_{\Sigma} \nabla \times \nabla \times \frac{N\alpha}{4\pi R} [\mathbf{E}'] \, dv' \tag{2.36}$$

and

$$\mathbf{H}'(\mathbf{r}, t) = \mathbf{H}^{(i)} + \int_{\Sigma} \nabla \times \frac{N\alpha\epsilon_0}{4\pi R} [\dot{\mathbf{E}}'] \, dv'. \tag{2.37}$$

Note that if the field point $\mathbf{r}$ is outside the medium, the integral boundary Σ will be that of the medium. If the field point is inside the medium, the small domain including the polarized atom or molecule must be excluded from the integration. This can be done considering the atom to be a small sphere with boundary σ and radius a. The integral value can be found by integrating the over Σ excluding the small region σ, and then taking the limit as $a \to 0$.

Within the medium, (2.35) can be written as

$$\mathbf{P} = N\alpha\epsilon_0 (\mathbf{E}^{(i)} + \mathbf{E}^{(d)}), \tag{2.38}$$

where $\mathbf{E}^{(d)}$ denotes the contribution to the field from the dipoles. From (2.28),

$$\mathbf{E}^{(d)} = \frac{1}{4\pi\epsilon_0} \int_{\sigma}^{\Sigma} \nabla \times \nabla \times \frac{[\mathbf{p}]}{R} \, dv'. \tag{2.39}$$

This intermediate result will be used later in the analysis.

If the incident field is monochromatic with angular frequency ω, then

$$\mathbf{E}^{(i)} \equiv \mathbf{E}^{(i)}(\mathbf{r})e^{-i\omega t}. \tag{2.40}$$

Also assume as a trial solution for $\mathbf{P}$ a monochromatic wave of the same frequency, but with velocity of propagation c/n. Then

$$\mathbf{P} \equiv \beta\mathbf{Q}(\mathbf{r})e^{-i\omega t}, \tag{2.41}$$

where

$$\beta \equiv (n^2 - 1)/k_0^2 \tag{2.42}$$

and $k_0 \equiv \omega_0/c$.

Although, at this point, the value of the constant n is completely unknown, finding it's value is one of the goals of this section.

The vector function $\underset{\sim}{Q}$ also must satisfy the wave equation,

$$\nabla^2 \underset{\sim}{Q} + n^2 k_0^2 \underset{\sim}{Q} = 0. \tag{2.43}$$

Assuming that $\underset{\sim}{Q}$ has no sources in the medium, then

$$\nabla \cdot \underset{\sim}{Q} = 0. \tag{2.44}$$

By substituting the trial solution (2.41) into (2.38), and by rewriting the equation in its time free form,

$$\underset{\sim}{Q} = N\alpha\varepsilon_0 \left\{ \underset{\sim}{E}^{(i)}/\beta + \underset{\sim}{E}^{(d)} \right\}. \tag{2.45}$$

In this equation,

$$\underset{\sim}{E}^{(d)} \equiv \frac{1}{4\pi\varepsilon_0} \int_{\sigma}^{\Sigma} \nabla \times \nabla \times \underset{\sim}{Q}(\underset{\sim}{\xi}') \, G(R) \, dv', \tag{2.46}$$

$G(R) \equiv e^{ikoR}/R$, and $\underset{\sim}{E}^{(d)} \equiv \beta \, \underset{\sim}{E}^{(d)} \, e^{-i\omega t}$.

In this derivation G(R) represents a unit amplitude spherical wave propagating in the vacuum between the dipoles. Therefore it must satisfy the wave equation,

$$\nabla^2 G + k_0^2 G = 0. \tag{2.47}$$

It has been shown [2.4] that for sufficiently small σ,

$$\int_{\sigma}^{\Sigma} \nabla \times \nabla \times \underset{\sim}{Q}(\underset{\sim}{\xi}') \, G(R) \, dv' = \nabla \times \nabla \times \int_{\sigma}^{\Sigma} \underset{\sim}{Q}(\underset{\sim}{\xi}') \, G(R) \, dv' - \frac{8\pi}{3} \underset{\sim}{Q}(\underset{\sim}{\xi}). \tag{2.48}$$

Therefore by rewriting (2.43) and (2.48) by using (2.42),

$$\nabla^2 G/G - \nabla^2 \underset{\sim}{Q}/\underset{\sim}{Q} = \beta \tag{2.49}$$

and

$$G\underset{\sim}{Q} = \frac{1}{\beta} \left[\underset{\sim}{Q} \nabla^2 G - G \nabla^2 \underset{\sim}{Q} \right]. \tag{2.50}$$

Then by using these intermediate results and Green's Theorem,

$$\int_{\sigma}^{\Sigma} \underset{\sim}{Q}(\underset{\sim}{r}')G(R)\,dv' = \frac{1}{\beta}\int_{\Sigma}\left(\underset{\sim}{Q}\frac{\partial}{\partial n'}G - G\frac{\partial}{\partial n'}\underset{\sim}{Q}\right)ds' - \frac{1}{\beta}\int_{\sigma}\left(\underset{\sim}{Q}\frac{\partial}{\partial n'}G - G\frac{\partial}{\partial n'}\underset{\sim}{Q}\right)ds'. \quad (2.51)$$

Here $\frac{\partial}{\partial n'}$ denotes differentiation of the source coordinates along an outward normal to the volume boundary.

The right most integral in (2.51) has been shown [2.5] to approach the value $-4\pi Q(r)$ as $a \to o$. Using this result with (2.48) and (2.46) yields

$$\lim_{\sigma \to 0} \underset{\sim}{E}^{(d)} = \frac{1}{4\pi\epsilon_0\beta}\nabla\times\nabla\times\int_{\Sigma}\left(\underset{\sim}{Q}\frac{\partial G}{\partial n'} - G\frac{\partial}{\partial n'}\underset{\sim}{Q}\right)ds' + \left\{\frac{1}{\epsilon_0\beta}\nabla\times\nabla\times\underset{\sim}{Q}(\underset{\sim}{r}) - \frac{2}{3\epsilon_0}\underset{\sim}{Q}(\underset{\sim}{r})\right\}. \quad (2.52)$$

Now by using a vector identity with (2.44) and (2.43), the second term on the right hand side of (2.52) becomes

$$\frac{1}{\epsilon_0\beta}\nabla\times\nabla\times\underset{\sim}{Q}(\underset{\sim}{r}) = \frac{n^2k_0^2}{\epsilon_0\beta}\underset{\sim}{Q}(\underset{\sim}{r}). \quad (2.53)$$

By summing this with the last term of (2.52) and by using (2.42), the bracketted value in (2.52) becomes

$$\left\{\ \right\} = \frac{n^2+2}{3\epsilon_0(n^2-1)}\underset{\sim}{Q}. \quad (2.54)$$

Substituting this result back into (2.52) gives

$$\underset{\sim}{E}^{(d)} = \frac{1}{3\epsilon_0}\left(\frac{n^2+2}{n^2-1}\right)\underset{\sim}{Q} + \frac{1}{4\pi\epsilon_0\beta}\nabla\times\nabla\times\int_{\Sigma}\left(\underset{\sim}{Q}\frac{\partial}{\partial n'}G - G\frac{\partial}{\partial n'}\underset{\sim}{Q}\right)ds'. \quad (2.55)$$

Denoting the second term on the RHS of (2.55) by ξ, and substituting (2.55) into (2.45) gives

$$\underset{\sim}{Q} = \frac{N\alpha}{3}\left(\frac{n^2+2}{n^2-1}\right)\underset{\sim}{Q} + \frac{N\alpha\epsilon_0}{\beta}\underset{\sim}{E}^{(i)} + N\alpha\epsilon_0\,\xi. \quad (2.56)$$

From the assumptions which led to (2.45), the first term in the equation above is a wave propagating with phase velocity c/n, while the second and third terms represent waves propagating with a phase velocity c.

Since the terms of (2.56) with the same propagation velocities must be equal,

$$\underset{\sim}{Q} = \frac{N\alpha}{3}\left(\frac{n^2 + 2}{n^2 - 1}\right)\underset{\sim}{Q}$$

and

$$\underset{\sim}{E}^{(i)}/\beta + \xi = 0.$$

Substituting the value for ξ into these equations and simplifying gives the final results of this section,

$$\frac{N\alpha}{3} = (n^2 - 1)/(n^2 + 2) \tag{2.57}$$

and

$$\underset{\sim}{E}^{(i)} + \frac{1}{4\pi\epsilon_0}\nabla \times \nabla \times \int_{\Sigma}\left(\underset{\sim}{Q}\frac{\partial G}{\partial n'} - G\frac{\partial}{\partial n'}\underset{\sim}{Q}\right) ds' = 0. \tag{2.58}$$

Equation (2.57) expresses the index of refraction n, in terms of the number density of the dipoles N and their polarizability α. This equation is known as the Lorentz-Lorenz formula. Equation (2.58) shows that the wave $\underset{\sim}{E}^{(i)}$ incident into the medium is extinguished at any point in the medium due to part of the dipole field. The incident wave is replaced by another wave,

$$\underset{\sim}{E}' = \frac{1}{N\alpha\epsilon_0}(n^2 - 1)\, k_0^2\, \underset{\sim}{Q}(\underset{\sim}{r})e^{-i\omega t},$$

which has phase velocity c/n. This result is known as the Ewald-Oseen extinction theorem. It implies that the index of refraction of the medium must be known in order to find the velocity of electromagnetic waves traveling through the medium. Equation (2.57) gives the relationship between the needed index and the material's density and polarizability. These results will be used in the following sections to derive the propagation velocity of optical signals through the mixture of gases which constitute the atmosphere.

2.4 Refractive Properties of Mixtures

The results in the previous section are applicable to substances with only one type of polarizable atom or molecule. However, the atmosphere is a mixture of many gases, the most prevalent ones being nitrogen, oxygen and argon. Therefore the relation between the index of refraction of a mixture and its constituents must be found in order to express the refractivity of the atmospheric gas mixture.

For any gas, the relationship between the number density and mass density is given by

$$N = N_0 \rho/M, \tag{2.59}$$

where N is the number of molecules per unit volume, N_0 is Avogadro's number, ρ is the density, and M is the molecular weight of the gas. If (2.57) is solved for the polarizability α, and (2.59) is used, then the molar refractivity can be defined by

$$A \equiv M\gamma/\rho. \tag{2.60}$$

Here the index term is defined by

$$\gamma \equiv (n^2 - 1)/(n^2 + 2). \tag{2.61}$$

Assuming that the polarization properties of the constituents do not change when gases are mixed, the molar refractivity of a mixture of ℓ gases is given [2.6] by

$$A_m = \frac{1}{N_m} \sum_{i=1}^{\ell} N_i A_i'. \tag{2.62}$$

Here $N_m = \sum_{i=1}^{\ell} N_i$. The specific refraction of the i^{th} component can be defined by

$$R_i \equiv A_i'/M_i = \gamma_i'/\rho_i'. \tag{2.63}$$

Here the prime denotes that the index term γ' is evaluated at the fixed gas density ρ_i'.

The index term of the mixture can be found by using (2.60) and (2.63) in (2.62), yielding

$$\gamma_m = \frac{\rho_m}{M_m}\left\{\frac{1}{N_m}\sum_{i=1}^{\ell} N_i M_i R_i'\right\}. \tag{2.64}$$

In this equation, ρ_m is the density of the mixture.

By using (2.59) for each component in (2.64), the index term of the mixture can be simplified to

$$\gamma_m = \sum_{i=1}^{\ell} \rho_i R_i. \tag{2.65}$$

For the case of three atmospheric constituents, (2.65) can be expressed by using (2.61) and (2.63) as

$$\left(\frac{n^2 - 1}{n^2 + 2}\right)_m = \sum_{i=1}^{3} \frac{\rho_i}{\rho_i'}\left(\frac{n_i^2 - 1}{n_i^2 + 2}\right)'. \tag{2.66}$$

This result shows that the index term of the mixture at an arbitrary density can be found from the index terms of the components. However these component index terms need only be given at the measured densities ρ_i', and not under the actual gas densities ρ_i in the mixture. This result separates the problem of finding the index term of the mixture into finding the index terms of the gas component under some measured conditions, and then determining how the component densities vary with the conditions.

Since most measurements of the index are in terms of the refractivity, the relationship between it and the index term also should be reviewed. By first defining the refractivity as

$$r \equiv (n - 1), \tag{2.67}$$

and then by using (2.61), the index term can be rewritten as

$$\gamma = \frac{r(r + 2)}{r(r + 2) + 3}. \tag{2.68}$$

Expanding this equation to second order in r gives

$$\gamma \approx \frac{2r}{3}(1 - r/6). \tag{2.69}$$

For air under standard conditions and for λ in the visible part of the spectrum, $r \approx 3 \times 10^{-4}$. Therefore, for these conditions, (2.69) should be accurate to better than 10^{-10} in n.

By using (2.69) in (2.66) and simplifying, the mixture refractivity becomes

$$r_m = \sum_{i=1}^{3} \frac{\rho_i}{\rho_i'} \left[\frac{1 - r_i'/6}{1 - r_m/6} \right] r_i'. \tag{2.70}$$

Now since $r_i'/6$ is small relative to 1, the refractivity can be approximated by its wavelength averaged value in the square bracketted terms. A further approximation can be made, since dry, CO_2-free air is the dominant term in (2.70). Therefore,

$$1 - r_m/6 \approx 1 - \langle r_m \rangle/6 \approx 1 - \frac{\langle r_1' \rangle}{6} \frac{\rho_1}{\rho_1'}. \tag{2.71}$$

Using these approximations in (2.70) gives the final result,

$$r_m = \sum_{i=1}^{3} \frac{\rho_i}{\rho_i'} \left[\frac{1 - \langle r_i' \rangle/6}{1 - \langle r_1' \rangle \rho_1/6\rho_1'} \right] r_i'. \tag{2.72}$$

This formula will be used with the expressions for ρ_i and r_i which will be developed in the next section.

2.5 The Phase Refractive Index of Air

The most accurate investigation of the dependence of the index of refraction of air on wavelength, composition and density has been given by Owens [2.7]. He states the common assumption made in index studies, which is that air may be considered to consist of only three components: dry air without CO_2, water vapor, and CO_2. In this section the wavelength dependence of the index terms and the density dependence on temperature and pressure given by Owens will be reviewed.

A second term "standard air" is used in the remainder of this thesis. It is defined as air without water vapor at a pressure of 1013.25 mbar, at a temperature of 15°C, and

containing the following components in molar percentages = 78.09% N_2, 20.95% O_2, 0.93% Ar, and 0.03% CO_2. The concentrations of the first three atmospheric constituents are very stable. However, the amount of water vapor varies both spatially over km distances and over hourly time spans. The amount of CO_2 has been slowly increasing over the past decades due to the burning of fossil fuels.

Dry CO_2 Free Air

Owens derived the refractivity value of CO_2-free standard air, by taking Edlen's 1966 formula [2.8] and compensating it for the effects of CO_2. The result was

$$r_1 \times 10^8 = a_1' + \frac{b_1'}{c_1' - \sigma^2} \frac{+d_1'}{e_1' - \sigma^2}, \tag{2.73}$$

where the value of the constants are given in Table 2.1. In this expression, $\sigma^2 \equiv 1/\lambda^2$, and λ is the optical vacuum wavelength in microns. The error introduced by compensating the earlier data for CO_2 was estimated to be less than 3×10^{-10} in n over the wavelength range of 0.3650 to 0.6328 microns. Equation (2.73) was estimated to be accurate to 1×10^{-9} in n for λ from 0.2303 to 2.0586 microns.

The density of dry, CO_2-free air was found by fitting experimental data [2.9] to a general equation of the form $\rho = MPZ^{-1}/RT$. Here M is the average molecular weight of the gas sample, R is the ideal gas constant, and Z is the inverse compressibility factor of the gas. The final form of Z^{-1} chosen after fitting the experimental data to formulas with increasing complexity in T and P was

$$Z_1^{-1} = 1 + P(b_1 + c_1 T^{-1} + d_1 T^{-2}). \tag{2.74}$$

The constants chosen by performing a least squares fit to the experimental data are given in Table 2.2.

Table 2.1
Refractivity Constants

Constant	i = 1	i = 2	i = 3	i = 4	i = 5
a_i'	8,340.78	295.235	22,822.1	2,371.34	–
b_i'	2,405,640.0	2.6422	117.8	683,939.7	–
c_i'	130.0	-0.032380	2.406,030.0	4,547.3	–
d_i'	15,994.0	0.004028	–	6,487.31	–
e_i'	38.9	–	–	58.058	174.174
f_i'	–	–	15,997.0	0.71150	-3.55750
g_i'	–	–	–	0.08851	0.61957

Table 2.2
Density Constants

Constant	i = 1	i = 2	i = 3	i = 4
a_i	348.328	216.582	529.37	–
b_i	57.90E-8	3.7E-4	–	57.90E-8
c_i	-9.4581E-4	-2.37321E-3	–	-9.3250E-4
d_i	0.25844	2.23366	–	0.25844
e_i	–	-710.792	–	–
f_i	–	77,514.1	–	–

To complete the evaluation, the ratio M/R was evaluated from the density of standard air from [2.9], then the result was adjusted to compensate for the effect of CO_2 in the standard air. The result,

$$\rho_1 = a_1 \frac{P}{T} Z_1^{-1}, \tag{2.75}$$

is in units of g/m^3, when P is given in mbar, and T is given in deg. K. The values of the constants above are given in Table 2.2. Owens compared the density values given by

(2.75) to those of the original experimental data. He found the error to be less than 3×10^{-6} in density for P in the range from 0 to 4 atmospheres, and T from 240 to 330°K.

Water Vapor

Owens found the absolute refractivity of water vapor by multiplying Erickson's [2.10] experimental values for the relative refractivity of water vapor by the refractivity value given by Barrell and Sears at $\lambda = 4679.46$ Å. The resulting equation for the refractivity of water vapor under the conditions of P = 13.33 mbar and T = 10°C was,

$$r_2 \times 10^8 = a_2' + b_2' \sigma^2 + c_2' \sigma^4 + d_2' \sigma^6. \tag{2.76}$$

The values of the constants in this expression are given in Table 2.1. This equation is accurate for n to 1×10^9 over the wavelength range of 0.3611 to 0.6440 microns. The value of water vapor refractivity is plotted versus wavelength in Figure 2.1.

The derivation of the formula for density of water vapor was carried out in the same way as that for dry air, except that calculated values were used for the compressibility factor of water vapor at low temperatures. Polynomial functions were fit to the temperature and pressure dependence of the inverse compressibility factor by using the equation of state given in [2.11] and the formula for the saturation pressure of water vapor given in [2.12].

The resulting expression for the density of water vapor at a pressure P_w was

$$\rho_2 = a_2 \frac{P_w}{T} [1 + P_w \beta(P_w) \gamma(T)], \tag{2.77}$$

where

$$\beta(P_w) = 1 + b_2 P_w$$

and

$$\gamma(T) = c_2 + d_2 T^{-1} + e_2 T^{-2} + f_2 T^{-3}.$$

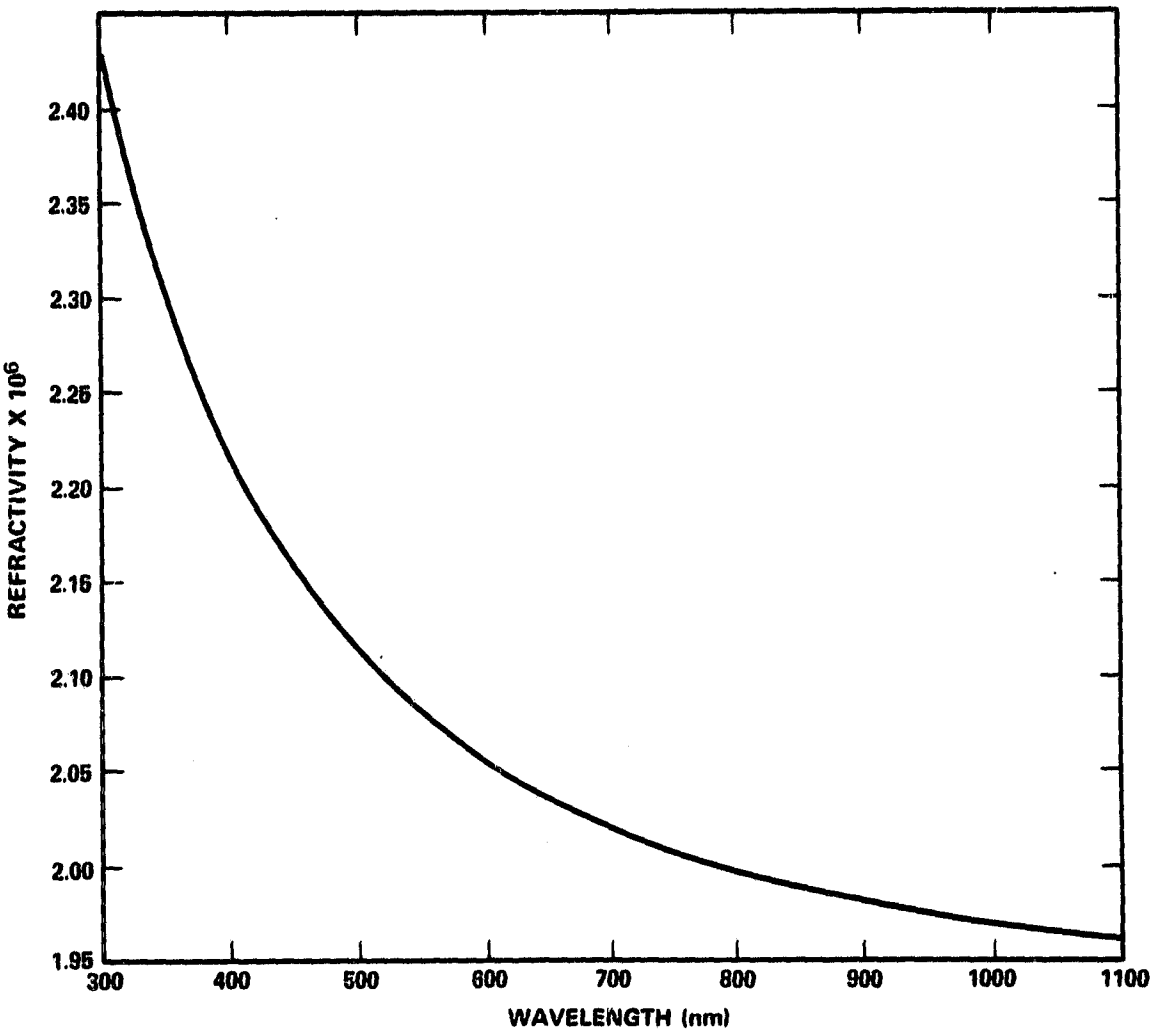

Figure 2.1. Water vapor group refractivity at 15°C, 50% Rh, (8.534 mb water vapor partial pressure).

Here ρ_2 is given in g/m^3 when P_w is given in mb and T is given in deg. K. The values of the constants in (2.77) are given in Table 2.2. The accuracy of the above formula was estimated by Owens to be not less than a few parts in 10^{-6}, relative to 1 atmosphere. The value of water vapor density given in (2.77) is plotted versus temperature in Figure 2.2.

Carbon Dioxide

The influence of CO_2 on atmospheric refractivity is usually small due to its low concentration in the atmosphere. However the refractivity of CO_2 was treated separately by Owens, since there can be situations (such as in polluted air) where an abnormally high CO_2 concentration will cause noticeable refraction errors.

The expression for the dispersion of CO_2 was taken from [2.8] and evaluated at 15°C and 1013.25 mbar. The result was

$$r_3 \times 10^8 = a_3' + b_3' \sigma^2 + \frac{c_3'}{(d_1' - \sigma^2)} + \frac{f_3'}{(e_1' - \sigma^2)}, \qquad (2.78)$$

where the values of the constants are given in Table 2.1. This result is accurate to 1 × 10^{-9} in n, for λ in the range of 0.2379 to 0.6910 microns.

Since the partial density of CO_2 is low, Owens assumed it behaved as an ideal gas. By taking Hilsenrath's data at 10^{-2} atmosphere, he found the density of CO_2 to be given by

$$\rho_3 = a_3 P_{CO_2}/T. \qquad (2.79)$$

The value of a_3 is given in Table 2.2, and ρ_3 is in units of g/m^3. This equation gives the density to an accuracy of 10^{-6} relative to 1 atmosphere.

Combined Formula

By using these results, Owens has evaluated (2.72) for air with 0.03% CO_2 and dry and wet partial pressures of P_D and P_W. The result was

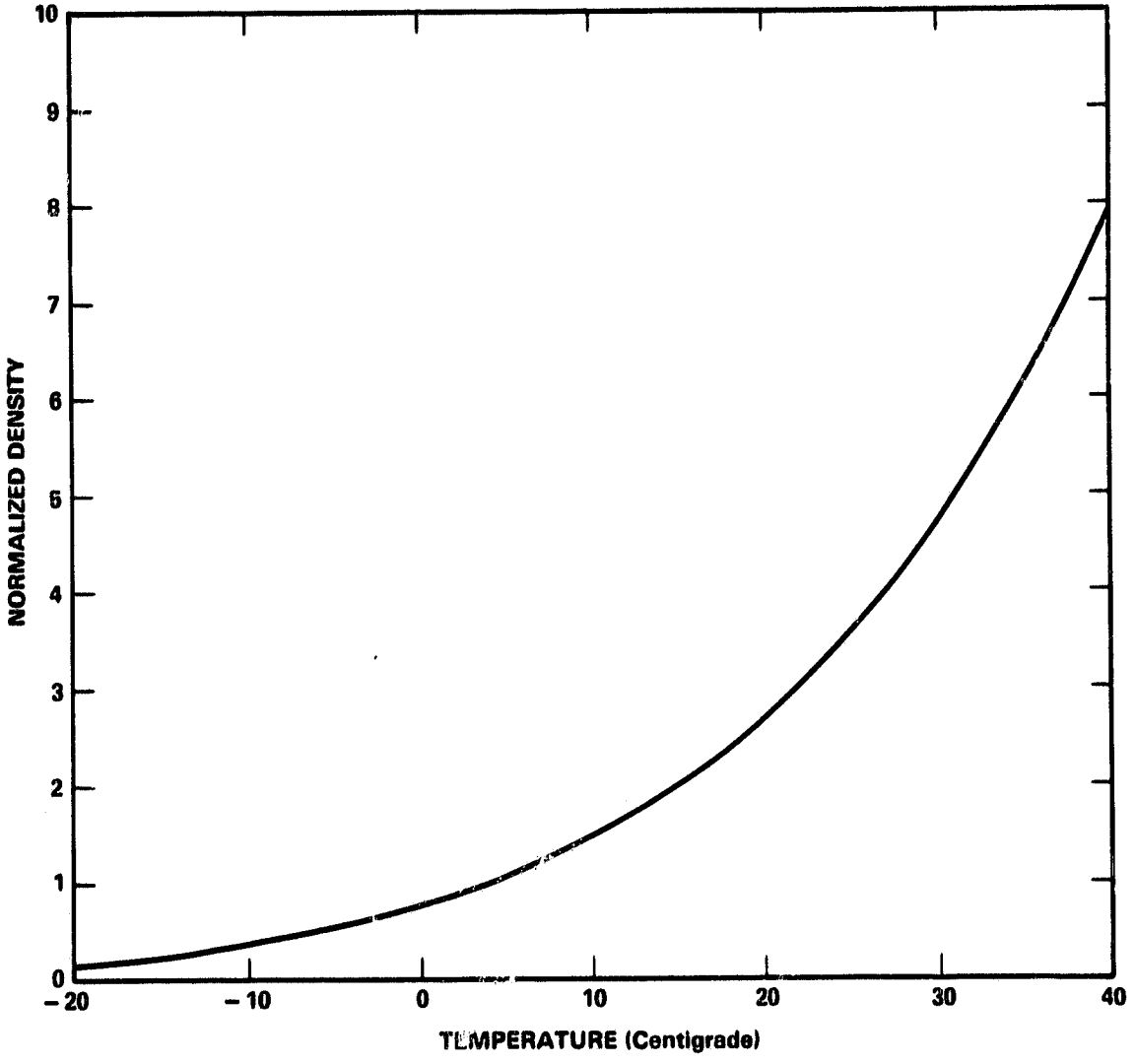

Figure 2.2. Saturated water vapor density versus temperature, normalized to ρ_w(15°C, 50% Rh) = 1.

$$r_{air} \times 10^8 = \left\{a'_4 + \frac{b'_4}{(d'_1 - \sigma^2)} + \frac{c'_4}{(e'_1 - \sigma^2)}\right\} D_D + \left\{d'_4 + e'_4\,\sigma^2 + f'_4\,\sigma^4 + g'_4\,\sigma^6\right\} D_W. \quad (2.80)$$

Here the density factors for the dry and wet air are given by

$$D_D = \frac{P_D}{T}\left\{1 + P_D(b_4 + c_4 T^{-1} + d_4 T^{-2})\right\} \quad (2.81)$$

and

$$D_W = \frac{P_W}{T}\left\{1 + P_W(1 + b_2 P_W)(c_2 + d_2 T^{-1} + e_2 T^{-2} + f_2 T^{-3})\right\}. \quad (2.82)$$

The values of the constants in (2.80) are given in Table 2.1 and the values in (2.81) and (2.82) are given in Table 2.2.

The final formula (2.80) can be used with commonly measured meteorological parameters of P, T, and relative humidity (Rh) by first using the law of partial pressures,

$$P = P_D + P_W. \quad (2.83)$$

Then by using the formula given by Marini & Murray [2.13],

$$P_W = \left(\frac{Rh}{100\%}\right)(6.11)\,10^{7.5(T-273.15)/(T-36)}. \quad (2.84)$$

The value of saturated water vapor pressure is plotted versus temperature in Figure 2.3. Therefore by using the measured values of P, T, and Rh for a sample of air with (2.84) and (2.83), the partial pressures of the dry and wet air can be found. These values substituted into (2.81) and (2.82) give the dry and wet density factors for the air sample. The refractive index of the air sample can then be computed by substituting these values into (2.80).

2.6 The Group Refractive Index of Air

For electronic distance measurements, modulated light commonly is used. The modulation envelope of the light travels at the group velocity v_g.

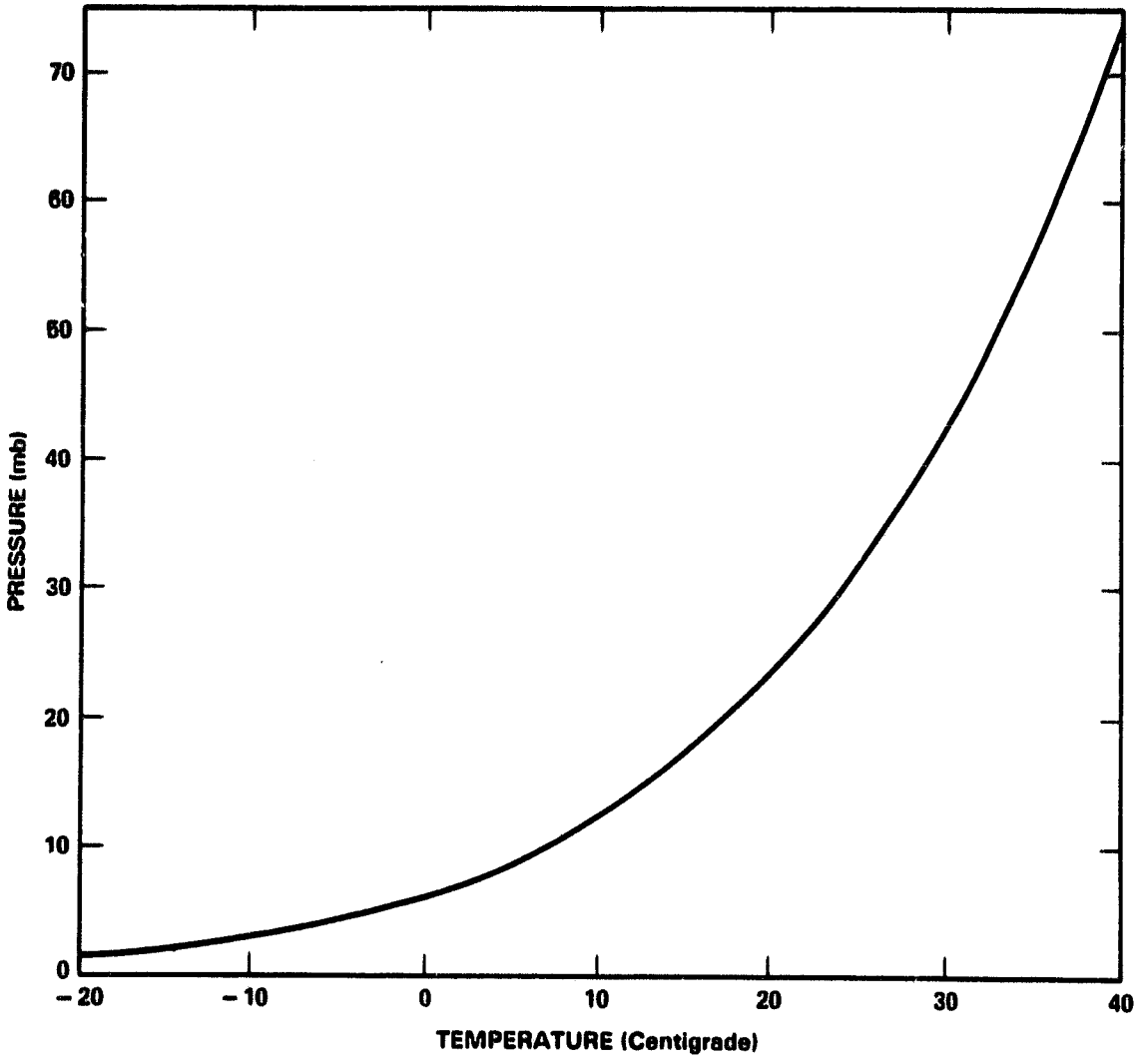

Figure 2.3. Saturated water vapor pressure versus temperature.

If the group index of refraction is defined by

$$n_g \equiv c/v_g, \tag{2.85}$$

then the group refractivity can be found by using

$$r_g = r + \sigma \left(\frac{\partial r}{\partial \sigma}\right). \tag{2.86}$$

By differentiating (2.80) and substituting the result into (2.86), Owens obtained

$$r_g \times 10^8 = \left\{a'_4 + b'_4 \frac{(c'_1 + \sigma^2)}{(c'_1 - \sigma^2)^2} + c'_4 \frac{(e'_1 + \sigma^2)}{(e'_1 - \sigma^2)^2}\right\} D_D + \left\{d'_4 + e'_5 \sigma^2 + f'_5 \sigma^4 + g'_5 \sigma^6\right\} D_W. \tag{2.87}$$

Here the values of the refractivity constants are given in Table 2.1.

A plot of r_g versus wavelength is shown in Figure 2.4 for standard air with 50% Rh. The values of the wet and dry refractivities under these conditions at the wavelengths of the prototype system are given in Table 2.3. The final results in (2.87), (2.81), and (2.82) will be used in the remainder of this dissertation for the group refractivity of air.

Table 2.3
Group Refractivities in ppm for Air at P = 1013.25 mbar, T = 15°C, Rh = 50% for the Wavelengths of the Prototype System.

λ(nm)	1064	532	355
Dry	274.40	287.30	311.34
Wet	1.967	2.100	2.357

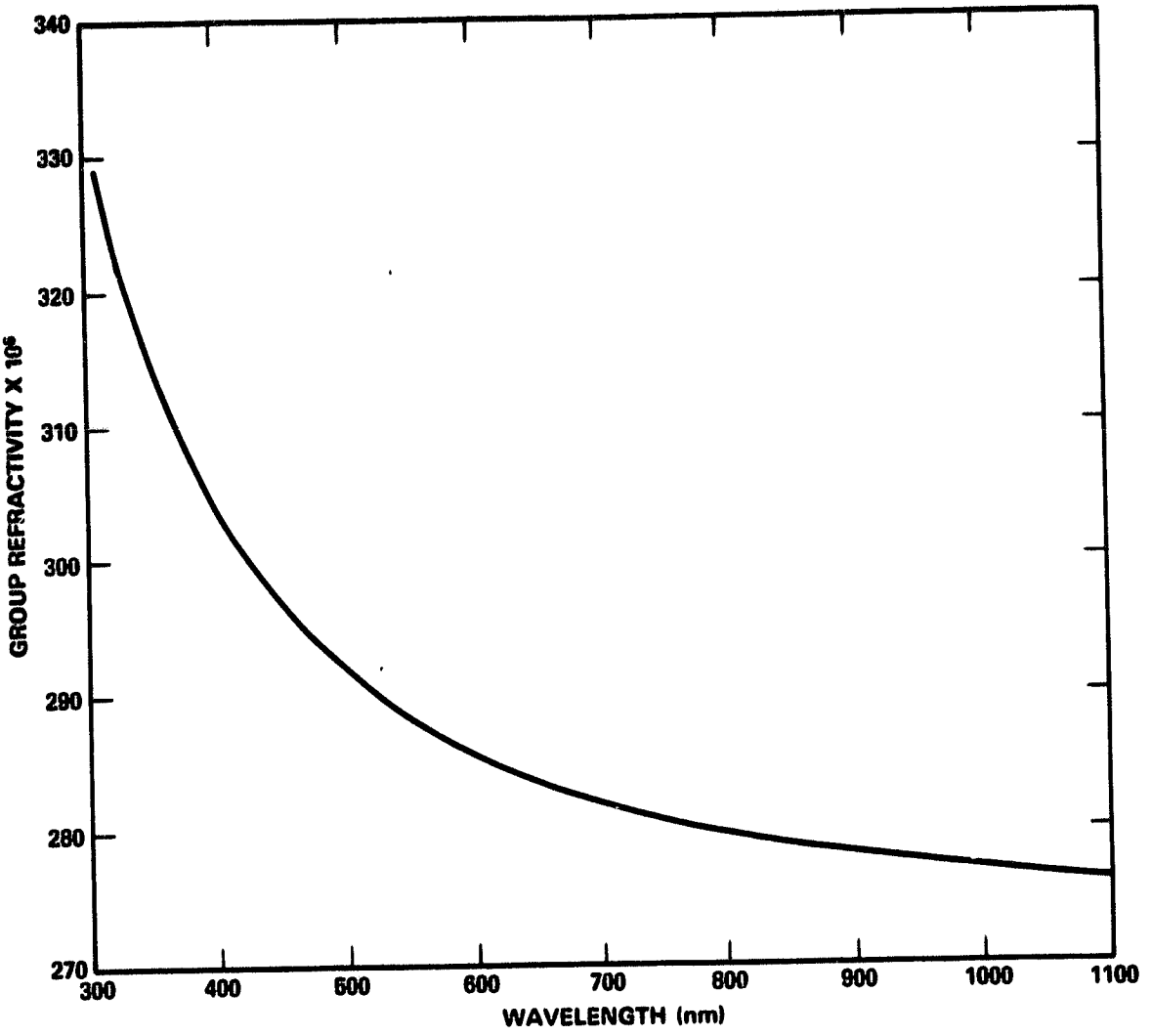

Figure 2.4. Group refractivity versus wavelength of std. air with 50% Rh.

Chapter 2 References

2.1 M. Born and E. Wolf, Principles of Optics, Pergamon Press, Oxford, 1975, p. 79.

2.2 J. Stratton, Electromagnetic Theory, McGraw Hill, New York, 1941, p. 29.

2.3 Ibid., p. 30.

2.4 Born & Wolf, op. cit. appendix 5.

2.5 Ibid., p. 375.

2.6 Ibid., p. 89.

2.7 J. Owens, Applied Optics, Vol. 6, 51 (1967).

2.8 B. Edlén, Metrologia, Vol. 2, 12 (1966).

2.9 J. Hilsenrath, et al., "Tables of Thermal Properties of Gases", NBS Circular 564, (November 1955).

2.10 K. Erickson, J. Opt. Soc. Amer., Vol. 52, 777 (1962).

2.11 J. Goff and S. Gratch, Trans. Am. Soc. Heat. Vent. Engr., Vol. 52, 95 (1946).

2.12 J. Goff, Humidity and Moisture, A. Wexler Editor, Rheinhold Publishing, New York, Vol. 3, 280 (1965).

2.13 J. Marini and C. Murray, "Correction of Laser Range Tracking Data for Atmospheric Refraction at Elevation Above 10 Degrees", NASA Goddard X-document 591-73-351, (November 1973).

CHAPTER 3

MULTIWAVELENGTH RANGING THEORY

Atmospheric refraction causes errors in the measurements of an optical ranging instrument in two ways. The greatest error is caused by the variable velocity of the signal as it traverses atmospheric regions with differing refractive indices. This causes the measured distance to exceed the actual geometrical distance to the target by a variable amount. A much smaller error is caused by deviations in the signal path geometry. These are caused by gradients in the refractive index which are perpendicular to the propagation direction. The gradients cause the optical path to deviate from a straight line, which also increases the measured range. Atmospheric turbulence causes both the refractive delays and the path deviations to change randomly in both space and time. Since these errors are present whenever ranging over an atmospheric path, they are irreducible error sources for both single and multicolor ranging systems.

The propagation theories for both single and multiple wavelength laser ranging systems operating over horizontal paths are derived in this chapter. The geometrical optics approximation is used for the path deviation calculations. This method is adequate for light to moderate turbulence, since the optical wavelength is much smaller than the smallest refractive atmospheric elements. This approximation is not expected to be valid for strong atmospheric turbulence, when multipath effects are evident. In the derivation the single wavelength theory is developed first, then it is extended for multiwavelength ranging.

The results show that the dry atmospheric delay errors can be measured and corrected by ranging with two optical wavelengths. Both the dry and the wet atmospheric delay errors can be measured and corrected by ranging with three colors, but this requires more accurate instrumentation. The magnitude of the limiting atmospheric error sources for both single and multicolor systems operating over long distances are derived in this chapter.

3.1 Single Wavelength Ranging

At any instant of time, the optical range to a target can be written as

$$L(\lambda) = |\underset{\sim}{p}| + \int_{\underset{\sim}{p}} r_g(\underset{\sim}{r}, \lambda)\, d\underset{\sim}{r}. \tag{3.1}$$

Here $\underset{\sim}{p}$ is the ray path, λ is the measurement wavelength, and r_g is the group refractivity of the atmosphere. The refractivity can vary along the path in both position and time due to fluctuations in atmospheric pressure, temperature, and water vapor. Since air is dispersive, r_g is wavelength dependent.

The ray path $\underset{\sim}{p}$ itself depends upon r_g. If the group index were known along the path, then $\underset{\sim}{p}$ could be found [3.1], [3.2] by solving

$$n_g(d\underset{\sim}{\ell}/ds) + \underset{\sim}{\ell}(\underset{\sim}{\ell} \cdot \underset{\sim}{\nabla} n_g) = \underset{\sim}{\nabla} n_g. \tag{3.2}$$

Here $\underset{\sim}{\ell} = d\underset{\sim}{r}/ds$ is the unit tangent to the ray path and $(\underset{\sim}{\ell} \cdot \underset{\sim}{\nabla} n_g) = dn_g/ds$ is the gradient of the group index in the direction of the propagating ray. Unfortunately, for almost all distance measurements, the detailed structure of n_g along the ranging path is not known, and (3.1) and (3.2) cannot be solved explicitly. Therefore, measurement systems must be used to estimate the path geometry and the atmospheric path delay. The following derivation reviews the physical basis for operation of these systems.

Thayer [3.3] has shown that $\underset{\sim}{p}$ can be closely approximated by a simple circular arc for propagation over horizontal paths near the earth's surface. Thayer also noted that since the path curvature error was small, the effect of the higher order curvature terms was negligible. The radius of curvature of the arc is given by

$$R = 1/\langle r_g' \rangle, \tag{3.3}$$

where $r_g' = dr_g/dh$ is the change of the refractivity with height above the earth's surface. The angle brackets in (3.3) denote averaging over the length of the path. Since the refractivity is most strongly dependent upon the atmospheric pressure and temperature.

$$r'_g \approx (dr_g/dP)(dP/dh) + (dr_g/dT)(d/dh) \approx r_g\left[\frac{(dP/dh)}{P} - \frac{(dT/dh)}{T}\right]. \quad (3.4)$$

The pressure lapse rate near the earth's surface has a nearly constant value of -0.12 mb/m. For temperature lapse rates of less than -0.34 deg. C/m the temperature lapse dominates in (3.4). Under these conditions, the air near the earth's surface is lower in refractivity than the air above it, and the ray curves upward. This effect is responsible for mirages, where the refracted image of the blue sky appears as water when viewed across a long hot surface. For temperature lapse rates of smaller magnitudes, the pressure term dominates in (3.5), and the ray curves downward from the source. Since in distance measuring, the angle of the transmitter is adjusted to the apparent position of the target, both these effects cause the ray to travel in an arc.

Using these results, (3.1) can be rewritten as

$$L(\lambda) = |\mathrm{arc}(R)| + \int_{\mathrm{arc}(R)} r_g(r, \lambda)dr. \quad (3.5)$$

The arc length can be written as $|\mathrm{arc}(R)| = L + \zeta(\lambda)$, where L is the straight line geometrical distance to the target. The 'excess' geometrical path length caused by the curvature in the path is given in [3.3] by

$$\zeta(\lambda) = L^3/(24\ R^2). \quad (3.6)$$

Plots of ζ versus L for λ = 532 nm are shown in Figure 3.1 for several temperature lapse rates. The plots show that the path curvature can cause 1 cm ranging errors for path lengths of 10 to 100 km. For roundtrip paths of one-way length L, the magnitude of the path curvature term in Figure 3.1 is doubled.

As a further simplification, the integral over the slightly curved arc-path in (3.5) can be replaced by an integral over a straight path of length $L + \zeta$, at the average height, $z(\lambda)$ of the arc. If the local vertical direction is denoted as z, Thayer showed that

$$z(\lambda) = L^2/(12\ R). \quad (3.7)$$

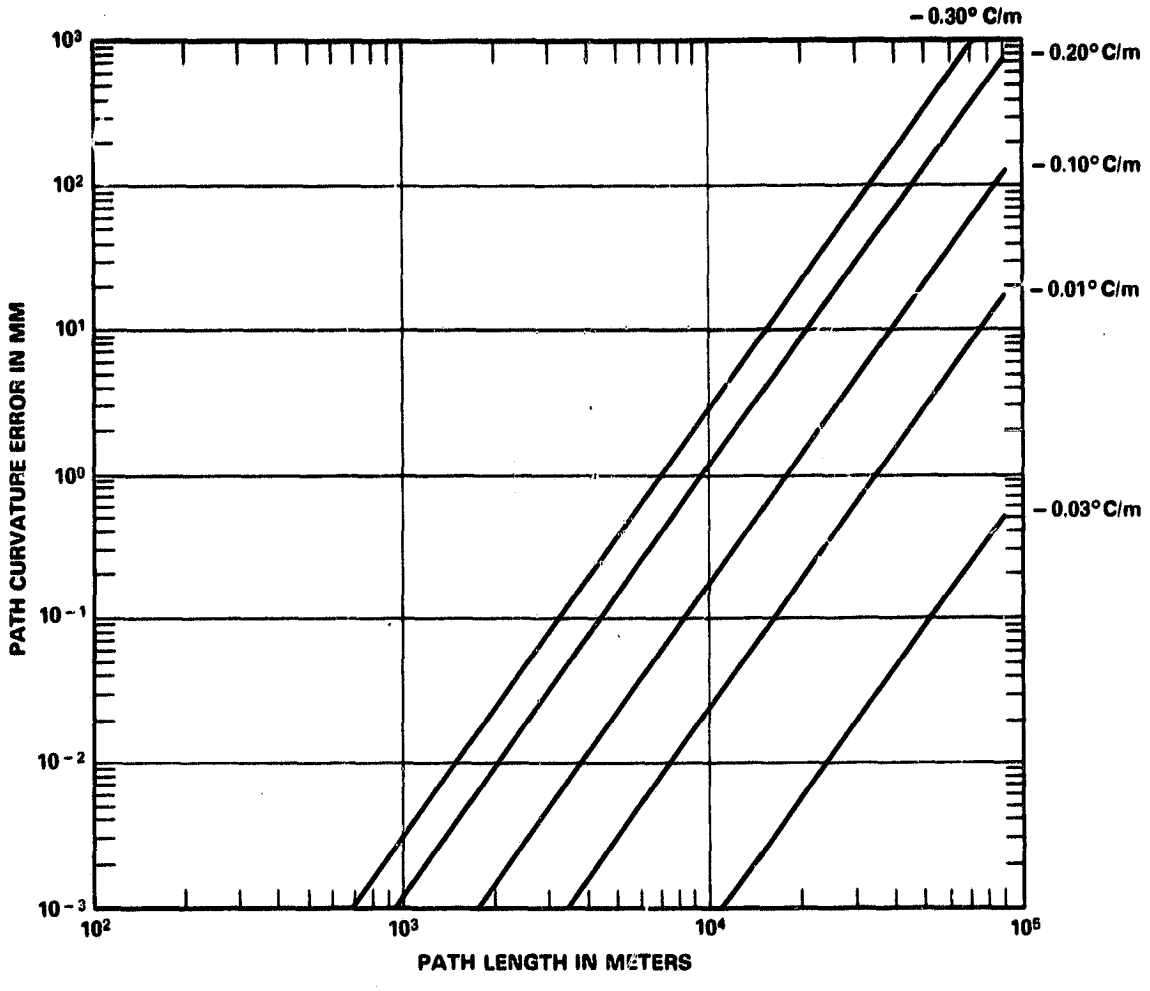

Figure 3.1. Path curvature error versus path length for single color ranging at a wavelength of 532 nm and various temperature lapse rates.

By further denoting the direction of propagation as x, (3.5) can be rewritten as

$$L(\lambda) = L + \zeta(\lambda) + \int_0^L r_g(x, z, \lambda)\, dx. \tag{3.8}$$

Here the very small term due to the refractivity in the excess path length has been neglected. This equation will be used as the basic ranging equation for this chapter.

The analysis in Chapter 2 showed that the group refractivity can be written as

$$r_g(\lambda) = D(\lambda)\, \rho_d(P_d, T) + W(\lambda)\, \rho_w(P_w, T). \tag{3.9}$$

Here the ρ's denote the densities of the dry and wet air components, and $D(\lambda)$ and $W(\lambda)$ denote the specific refractivities of the dry and wet air.

Substituting (3.9) into (3.8) gives

$$L(\lambda) = L + \zeta(\lambda) + D(\lambda)\, I_d(z, L) + W(\lambda)\, I_w(z, L) \tag{3.10}$$

where

$$I_d = \int_0^L \rho_d(x, z)\, dx \tag{3.11}$$

and

$$I_w = \int_0^L \rho_w(x, z)\, dx. \tag{3.12}$$

As was shown in Chapter 2, the terms $D(\lambda)$ and $W(\lambda)$ are well known from laboratory analysis. The dependence of ρ_d and ρ_w on atmospheric conditions is also well known, but the values of I_d and I_w are not known due to uncertainties in conditions along the path. For horizontal paths, the primary uncertainty is in the temperature structure.

In single color ranging, $L(\lambda)$ is measured by the instrument and the dry and wet refractive corrections are made from endpoint observations of P, T, and Rh. This technique has several inherent errors. One error is due to lack of correlation between endpoint density readings and path averaged ones. Another is caused by the error in estimating the path

averaged refractivity lapse rate. A third error is caused by turbulent fluctuations in the refractive index. These cause the measured path length to change with rates approaching $1\,k_n dz$.

All these errors limit single-color distance measuring accuracy to approximately 1 part per million. The average refractivity effects can be reduced by making aircraft measurements of refractivity near the ranging path, as has been reported by Berg and Carter [3.4]. However, this method is only applicable for paths well above the ground, and it makes distance determinations more complicated and expensive. The lack of correlation between the aircraft measured and the actual path conditions typically limit the improvement to a few parts in 10^7.

3.2 Three Color Ranging

Ranging simultaneously at several optical wavelengths can give substantial improvements in distance accuracy, and the single wavelength ranging theory can be readily extended for this case. Since the primary uncertainties in such measurements are L, I_d and I_w, three wavelengths are needed to estimate the unknowns from the ranging measurements.

For ranging over the same path simultaneously at wavelengths λ_1, λ_2, and λ_3, (3.10) can be rewritten as

$$L_1 = L + \zeta_1 + D_1 I_d(z_1) + W_1 I_w(z_1), \tag{3.13a}$$

$$L_2 = L + \zeta_2 + D_2 I_d(z_2) + W_2 I_w(z_2), \tag{3.13b}$$

and

$$L_3 = L + \zeta_3 + D_3 I_d(z_3) + W_3 I_w(z_3). \tag{3.13c}$$

Here all terms depending on λ_i have been denoted by the subscript i. The integrated density terms depend weakly upon wavelength, since both the average beam height and instantaneous delay depend upon the temperature and pressure lapse rates and the atmospheric turbulence. These equations can be solved simultaneously for the unknowns L,

I_d, and I_w from measurements of L_1, L_2, and L_3. The resulting expressions for the wet and dry air densities are

$$I_w(z_1) = (-b/d)(\Delta L_{31} - e_3) + (1/\Delta W_{32} + ba_w/d)(\Delta L_{32} - e_2), \tag{3.14}$$

and

$$I_d(z_1) = (1/d)(\Delta L_{31} - e_3) + (a_w/d)(\Delta L_{32} - e_2). \tag{3.15}$$

Here the ΔX_{ij} terms are defined as $X_i - X_j$. The intermediate terms in (3.14) and (3.15) are $a_w = \Delta W_{31}/\Delta W_{32}$, $b = \Delta D_{32}/\Delta W_{32}$, and $d = \Delta D_{31} - a_w \Delta D_{32}$.

The turbulence and path curvature are error terms in (3.14) and (3.15), since their values cannot be reliably predicted by endpoint measurements. Their values are

$$e_3 = \Delta\zeta_{31} + \Delta L'_{31}, \tag{3.16a}$$

and

$$e_2 = (\Delta\zeta_{31} - \Delta\zeta_{21}) + \Delta L'_{31} - \Delta L'_{21}. \tag{3.16b}$$

The differential path curvature term $\Delta\zeta_{31}$ is plotted versus L in Figure 3.2. The differential path curvature error can be seen to easily exceed 1 mm for moderate length (10 to 50km) horizontal paths. In two color ranging, the value of this term is magnified by the dispersion multiplier when solving for L. For the two wavelengths used in the figure, the multiplier value is 7.46. For two-way ranging, the magnitude of the path curvature values shown in Figure 3.2 should be doubled.

The differential turbulence terms in (3.16) are given by

$$\Delta L'_{31} = D_3 \Delta I_{d\,31} + W_3 \Delta I_{w\,31} \tag{3.17a}$$

and

$$\Delta L'_{21} = D_2 \Delta I_{d\,21} + W_2 \Delta I_{w\,21}. \tag{3.17b}$$

Differential turbulence errors are caused by the difference in the integrated path refractivities for the measurement colors. The values of these terms cannot be estimated without extensive measurements along the ranging path. In the absence of such data, these

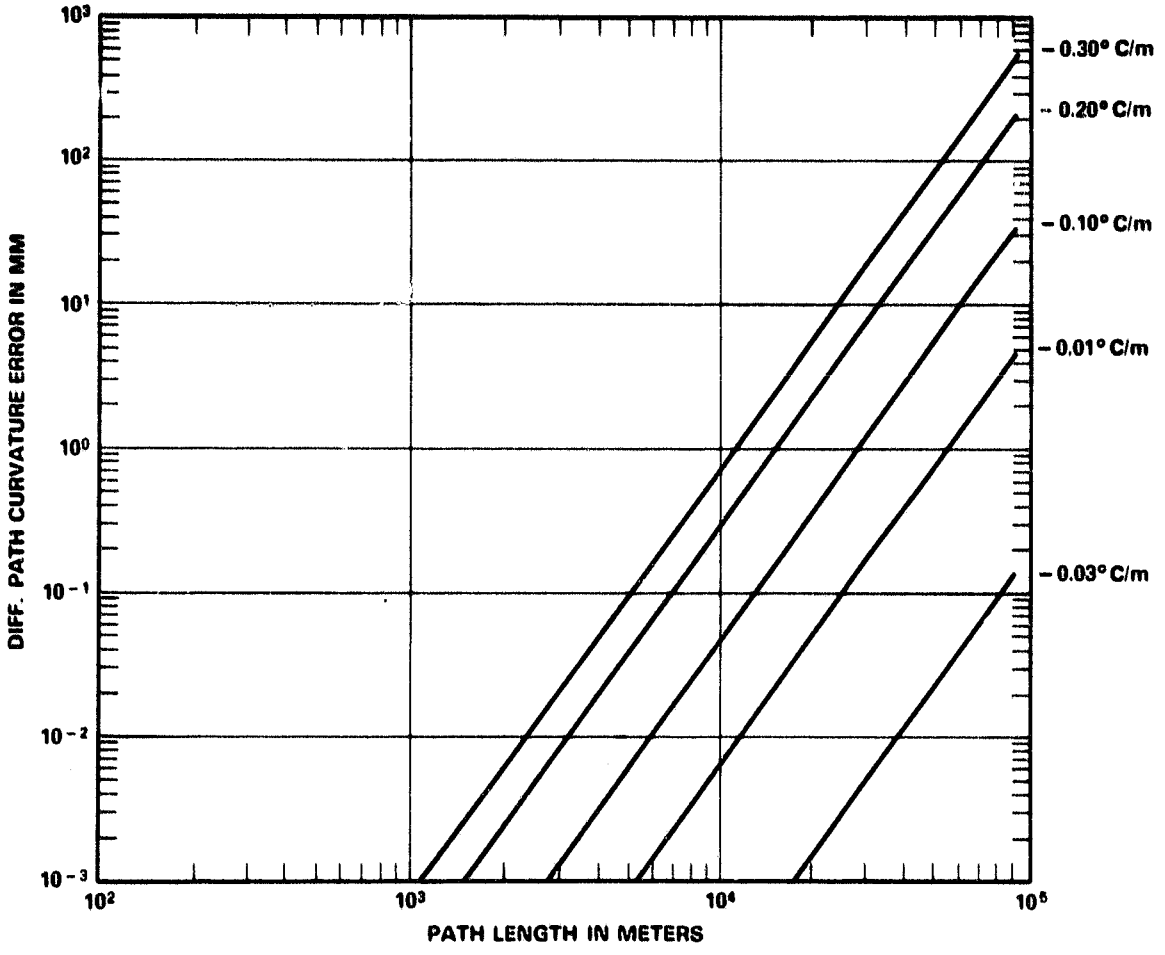

Figure 3.2. Differential path curvature error versus path length for two color ranging and various temperature lapse rates. The wavelengths used are 355 and 1064 nm.

terms constitute an irreducible error in the ranging system. The magnitude and statistics of this error will be discussed in a later section.

The total atmospheric path correction at λ_1 can be found by substituting (3.14) and (3.15) into (3.13a). The result is

$$D_1 I_{d1} + W_1 I_{w1} = f(\Delta L_{31} - e_3) + g(\Delta L_{32} - e_2). \tag{3.18}$$

In the above equation, the constants are given by

$$f = (D_1 - W_1 b)/d$$

and

$$g = (W_1/\Delta W_{32}) + (W_1 b\, a_w - D_1 a_w)/d.$$

These are a function of wavelength only.

Since the dispersion curves of dry air and water vapor in the near visible region have very similar shapes, accurate measurements of the ΔL's are required. For example, in the prototype system, $\lambda_1 = 1064$nm, $\lambda_2 = 532$nm, and $\lambda_3 = 355$nm. The total refractive correction at λ_1 for these wavelengths is

$$D_1 I_{d1} + W_1 I_{w1} = 167(\Delta L_{31} - e_3) - 245(\Delta L_{32} - e_2). \tag{3.19}$$

This result shows that the dispersive delays must be measured much more accurately than the single color range delay. For state-of-the-art systems, L_1 can be measured to about 1 cm. Therefore the ΔL's must be measured to 40μm for comparable accuracy in the delay correction. Unfortunately, this requirement exceeds the current capabilities of both pulsed and phase measurement systems operating over long paths.

3.3 Two Color Ranging

The accuracy requirements for measuring the differential path lengths can be relaxed by using a single ΔL measurement to estimate only the dry index term. The much smaller water vapor delay term then can be estimated by a single endpoint measurement of humidity. Such a system requires only two optical wavelengths.

The required performance can be calculated by first noting that with this approximation, (3.12) becomes

$$I_w \approx L\rho_w(0). \tag{3.20}$$

Here $\rho_w(0)$ is the water vapor density computed from measurements taken at the ranging site.

The simultaneous ranging equations are given by substituting (3.20) into (3.13a) and (3.13c), yielding

$$L_1 = L[1 + W_1\rho_w(0)] + \zeta_1 + D_1 I_{d1}, \tag{3.21a}$$

and

$$L_3 = L[1 + W_3\rho_w(0)] + \zeta_3 + D_3 I_{d3}. \tag{3.21b}$$

In these expressions $W_i\rho_w(0)$ is the endpoint group refraction of water vapor at wavelength i.

Next, solving (3.21) simultaneously for the integrated dry air density yields

$$I_{d1} = [\Delta L_{31} - \Delta W_{31}\, L_1\rho_w(0) - \Delta\zeta_{31}]/\Delta D_{31}. \tag{3.22}$$

In this equation, the approximation $L\, W_i\rho_w(0) \approx L_i W_i\rho_w(0)$ was used.

The target distance can be found by substituting (3.20) and (3.22) into (3.10). The result is

$$L = L_1 - L_1 W_1\rho_w(0) + L_1\rho_w(0)\Delta W_{31} a_d - a_d\Delta L_{31} + a_d\Delta L'_{31} + \zeta_c. \tag{3.23}$$

In this equation, the dry air dispersion factor,

$$a_d = D_1/\Delta D_{31}. \tag{3.24}$$

The first three terms on the right hand side of (3.23) are, respectively, the measured single color range, the water vapor delay correction, and the water vapor dispersion correction. The next term is the dry air delay correction which is based on the measured differential path length ΔL_{31}, and the following term is the error caused by atmospheric turbulence.

The magnitude and statistics of this error will be discussed in the next section.

The last term in (3.23) is the geometrical correction to both the dispersion and the single color measurement. Its value can be simplified by using (3.6) and by neglecting the small contribution of water vapor to path curvature. The result is

$$\zeta_c = \zeta_1[(D_1 + D_3)/D_1 - 1] \approx \zeta_1. \qquad (3.25)$$

This last approximation is valid to approximately 10%, since the dispersion of air is small relative to its refractivity. The approximation will not significantly effect the accuracy of (3.23), since ζ_c is already small.

For comparison with (3.19), the two color system range correction given in (3.23) can be evaluated by using $\lambda_1 = 1064$ and $\lambda_3 = 355$ nm. Under the conditions of P = 1013.25 mbar, T = 15 deg. C and Rh = 50%, the value of the refractive correction is

$$D_1 I_{d1} + W_1 I_{w1} = 7.43\,\Delta L_{31} - 0.928 \times 10^{-6}\, L_1 + 7.43\,\Delta L'_{31} + \zeta_1. \qquad (3.26)$$

Therefore thirty times less instrumental accuracy is required for measuring the differential delay with a two-color system than with a three-color system.

However, the two-color system is susceptible to errors in the water vapor estimate. The magnitude of this error is directly proportional to the water vapor density. A plot of the temperature dependence of this error is shown in Figure 3.3. For the atmospheric conditions listed above, an 11% error in estimating the path-averaged water vapor results in a fractional path length error of 10^{-7}. Therefore, high accuracy relative humidity readings should not be required under most circumstances.

The measured range also is used as an atmospheric correction term in (3.26). Since the accuracy required of L_1 for the water vapor correction is less than the accuracy required for the uncorrected delay measurement, no additional requirements are placed on the measurement system. Since this technique requires the least accurate differential delay measurement, it was used for the prototype system's operation.

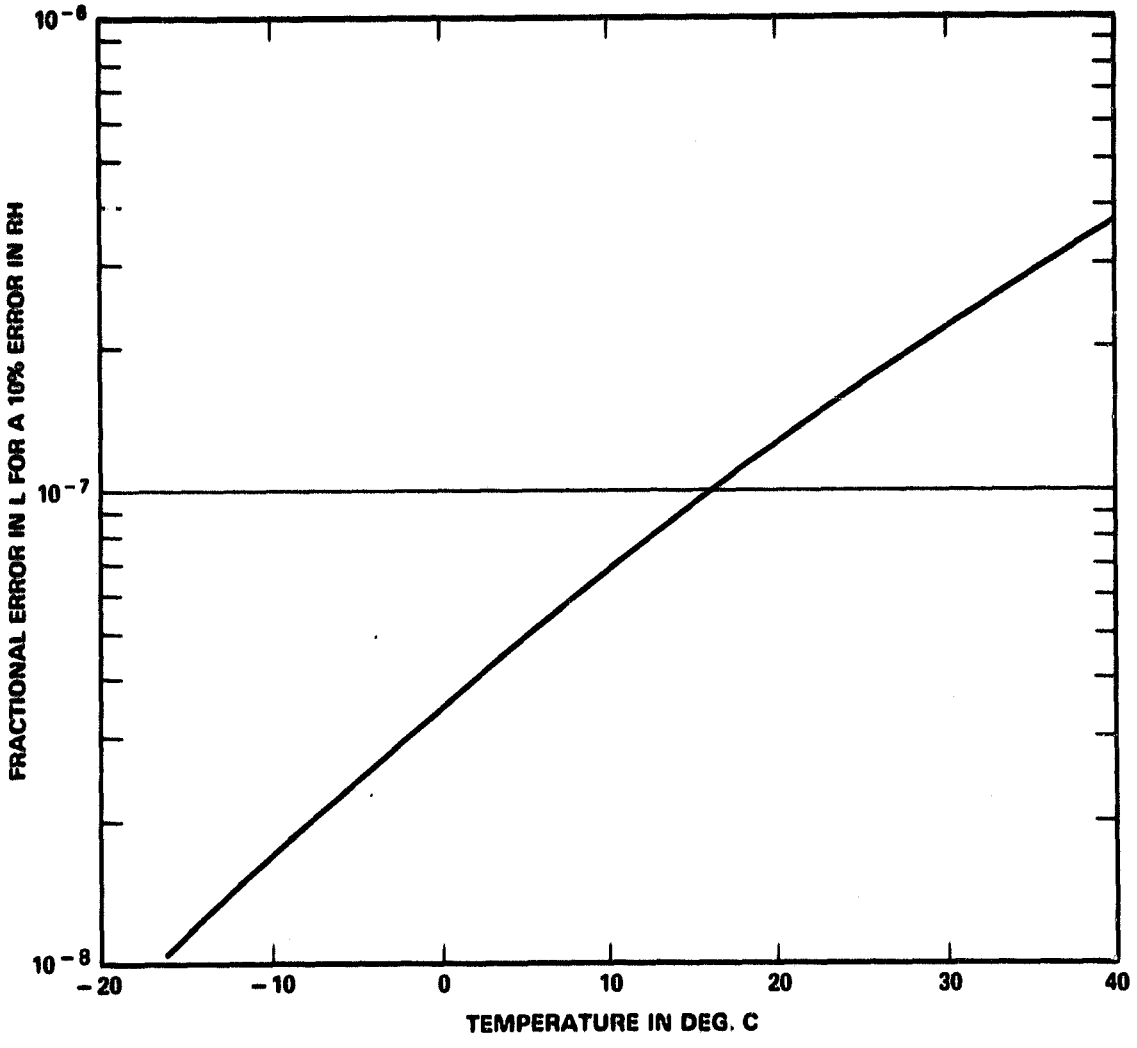

Figure 3.3. Sensitivity of two color ranging to errors in estimating the path averaged water vapor. P = 1013.25 mb and Rh = 50%.

3.4 Turbulence Effects on Ranging Accuracy

Atmospheric turbulence randomly changes the path delays measured by single and multicolor ranging systems. For multicolor ranging systems, the gradient in the index across the ranging path causes the colors to separate spatially, and the turbulence causes the separated paths to undergo slightly different delays. Paths which are separated by the outer scale of turbulence have nearly uncorrelated delay values, while paths separated by less than the inner scale have well correlated delay fluctuations. Gardner [3.5] has studied the effects of atmospheric turbulence on single and multiple wavelength ranging systems, and the analysis in this section follows his approach.

The two scale sizes mentioned above are important in characterizing turbulence. The outer scale, L_0, is a measure of the largest turbulent atmospheric elements. For horizontal paths, $L_0 \approx z/4$ [3.6]. The inner scale, ℓ_0, is the smallest size refractive eddy supported by the atmosphere. For near the earth's surface, the inner scale is typically several mm.

The magnitude of the average path separation for two color ranging can be computed by using (3.7) for the measurement wavelengths. This path separation is plotted versus length for various temperature lapse rates in Figure 3.4. The figure shows that even for moderate lapse rates, the average path separation can equal the outer scale of turbulence in 20 to 50km. The average beam separation for two-way ranging will be the same as in Figure 3.4.

The magnitude of the turbulent fluctuations in path length are described by the covariance function. For paths $\underline{\rho}_1$ and $\underline{\rho}_2$, the covariance of the length fluctuations $\Delta L'$ can be written as

$$B_{\Delta L'} = \int_{\underline{\rho}_1} d\underline{\xi}_1 \int_{\underline{\rho}_2} d\underline{\xi}_2 \langle n_1(\underline{\xi}_1)\, n_2(\underline{\xi}_2)\rangle. \qquad (3.27)$$

By assuming the refractive index fluctuations in each path are isotropic, the covariance function of the index fluctuations can be written as

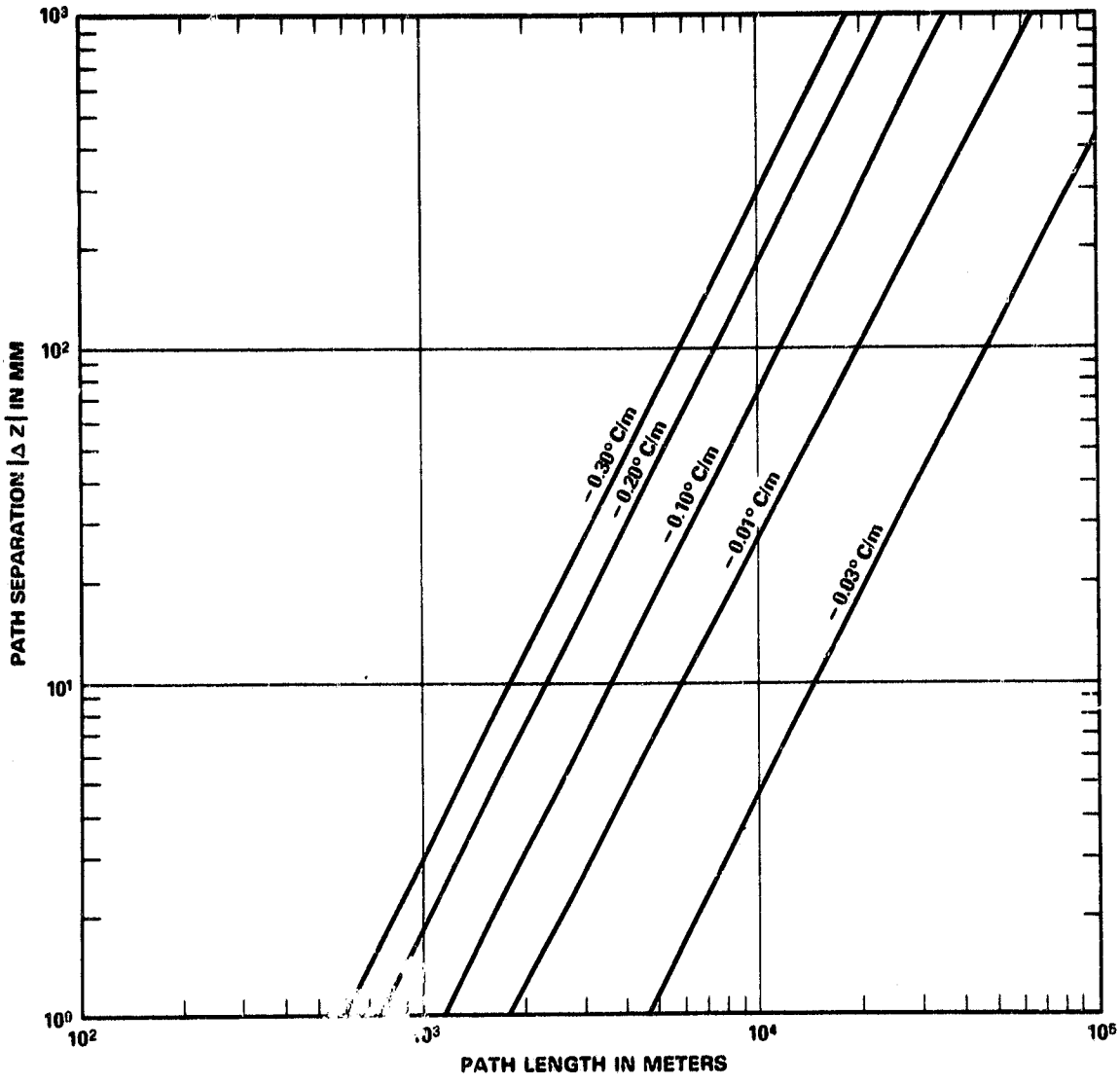

Figure 3.4. Path separation versus path length for two color ranging under various temperature lapse rates.

$$\langle n(\mathcal{L}_1)\, n(\mathcal{L}_2)\rangle = B_n^v[(\mathcal{L}_1 + \mathcal{L}_2)/2]\; B_n^0(|\mathcal{L}_1 - \mathcal{L}_2|). \tag{3.28}$$

Here B_n^v is a measure of the strength of the fluctuations in index at the average coordinate of the two paths, while B_n^0 is the correlation between fluctuations at points $\mathcal{L}_1$ and $\mathcal{L}_2$.

Gardner has shown for parallel paths of one-way length L, separated by a distance Δz, (3.27) can be rewritten as

$$B_{\Delta L'}(\Delta z) = 4 \int_0^L dx' \int_{x'/2}^{L-x'/2} dx\; B_n^v(x)\; B_n^0[(x'^2 + \Delta z^2)^{1/2}]. \tag{3.29}$$

Here x is the average coordinate along the direction of propagation, x′ is the difference value in the same direction, and z is the local vertical. For ranging to a corner reflector over a path length L, the beam will traverse a distance of 2L, and the value of (3.29) will be doubled.

For path lengths $L >> L_0$, the upper limit of the outer integral in (3.29) can be extended to ∞, since the additional turbulent elements included are uncorrelated. The limits of the inner integral in (3.29) also can be extended to (0, L), since the turbulence strength does not change significantly in the small additional path length. The error introduced by both these assumptions is approximately equal to L_0/L.

By using these assumptions, (3.29) can be rewritten as

$$B_{\Delta L'}(\Delta z) = 4 \int_0^L dx\; B_n^v(x) \int_0^\infty dx'\; B_n^0[(x'^2 + \Delta z^2)^{1/2}]. \tag{3.30}$$

The spatial correlation function B_n^0 can be described in terms of its spatial spectrum Φ_n^0 by

$$B_n^0(r) = 4\pi \int_0^\infty dk\; k^2\; \Phi_n^0(k)\; \sin(kr)/(kr). \tag{3.31}$$

Here k denotes the wave number. The covariance function for the path length fluctuations can be found by using (3.31) in (3.30). After simplifying, the result is

$$B_{\Delta L'}(\Delta z) = 8\pi^2 \int_0^L dx\; B_n^v(x) \int_0^\infty dk\; k\; \Phi_n^0(k)\; J_0(k\Delta z). \tag{3.32}$$

The refractive index variance at location x can be written in terms of the turbulence structure parameter [3.7] by

$$B_n^v(x) = [0.033\,\pi^{3/2}\Gamma(1/3)/\Gamma(1/6)]\; L_0^{2/3}\; C_n^2(x) = 0.523\; C_n^2(x)\; L_0^{2/3}. \tag{3.33}$$

The turbulence structure parameter is constant over statistically homogeneous horizontal paths, so that

$$B_n^v(x) \approx 0.523\; C_n^2(0)\; L_0^{2/3}. \tag{3.34}$$

The dependence of C_n^2 with z has been modeled by Hufnagel [3.8], as was reported by Brookner [3.9]. For horizontal paths 10m above the ground, C_n^2 was found to range from $2.15 \times 10^{-15}\,m^{-2/3}$ for the dawn-dusk minimum, to $5.4 \times 10^{-14}\,m^{-2/3}$ for a sunny day.

Gardner considered both the modified von Karman (VK) spectrum and the Greenwood and Tarazano (GT) spectrum [3.7] for Φ_n^0. For the VK spectrum,

$$\Phi_n^0(k) = \left\{\Gamma(11/6)\; L_0^3\; \pi^{-3/2}/\Gamma(1/3)\right\}\; \exp(-k^2/k_m^2)/(1 + k_m^2\, L_0^2)^{11/6}, \tag{3.35}$$

where the constant $k_m = 5.92\ell_0$.

For the GT spectrum,

$$\Phi_n^0(k) \propto (k^2 L_0^2 + k\, L_0)^{-11/6}. \tag{3.36}$$

The GT spectrum is a new model derived from atmospheric microtemperature measurements. It agrees well with the VK spectrum for $kL_0 > 1$, but has substantially more turbulent energy in the lower wave numbers. Therefore the refractive index fluctuations remain correlated over greater distances than for the VK spectrum. Since the GT spectrum was derived from actual atmospheric measurements, it is expected to be more accurate than the VK spectrum.

The mean square path deviation for ranging at one color can be computed by setting $\Delta z = 0$ in (3.32) and by using (3.34). For the VK spectrum, by using the results in (3.35),

$$\langle \Delta L'^2 \rangle_{VK} = 1.564\, C_n^2(0)\, L_0^{5/3} L. \tag{3.37}$$

Similarly, for the GT spectrum, by using (3.36),

$$\langle \Delta L'^2 \rangle_{GT} = 13.16\, C_n^2(0)\, L_0^{5/3} L. \tag{3.38}$$

These results show that the rms path deviation predicted by the GT spectrum is 2.9 times larger than that predicted by the VK spectrum. For two-way ranging, as in ranging to a corner reflector, the numerical coefficients in (3.37) and (3.38) will be doubled.

The rms ranging error in (3.38) is plotted versus length in Figure 3.5, for beam elevations of 1 and 10 meters above the ground. In this figure, $L_0 = z/4$, and the magnitude of C_n^2 was taken from [3.9]. It shows that the turbulent range deviations are larger at higher beam elevations, due to the larger value of L_0. On a sunny day, the range deviations can approach 0.2mm for a 10km path. For two-way ranging, the rms error in Figure 3.5 should be multiplied by $\sqrt{2}$.

For multicolor systems, the path deviations at each color will be different due to the spatial separation in the beams. The mean square fluctuation of the path differences between colors i and j due to the turbulence can be written as

$$\langle \Delta L_{ij}'^2 \rangle = 2 \left\{ 1 - \rho_{\Delta L}(\Delta z) \right\} \langle \Delta L'^2 \rangle. \tag{3.39}$$

The correlation coefficient $\rho_{\Delta L}$ can be expressed in terms of $B_{\Delta L}$ by

$$\left\{ 1 - \rho_{\Delta L}(\Delta z) \right\} = 1 - B_{\Delta L}(\Delta z)/\langle \Delta L'^2 \rangle. \tag{3.40}$$

For the VK spectrum, $B_{\Delta L}$ can be found by substituting (3.35) into (3.32) and simplifying. The result is

$$\left\{ 1 - \rho_{\Delta L} \right\}_{VK} = 1 - \left\{ 2^{1/6}/\Gamma(5/6) \right\} (\Delta z/L_0)^{5/6} K_{5/6}(\Delta z/L_0), \tag{3.41}$$

where K is the modified Bessel function. For short to medium length paths, the separation between colors will be less than L_0. Therefore, when $\Delta z << L_0$, (3.41) can be simplified to

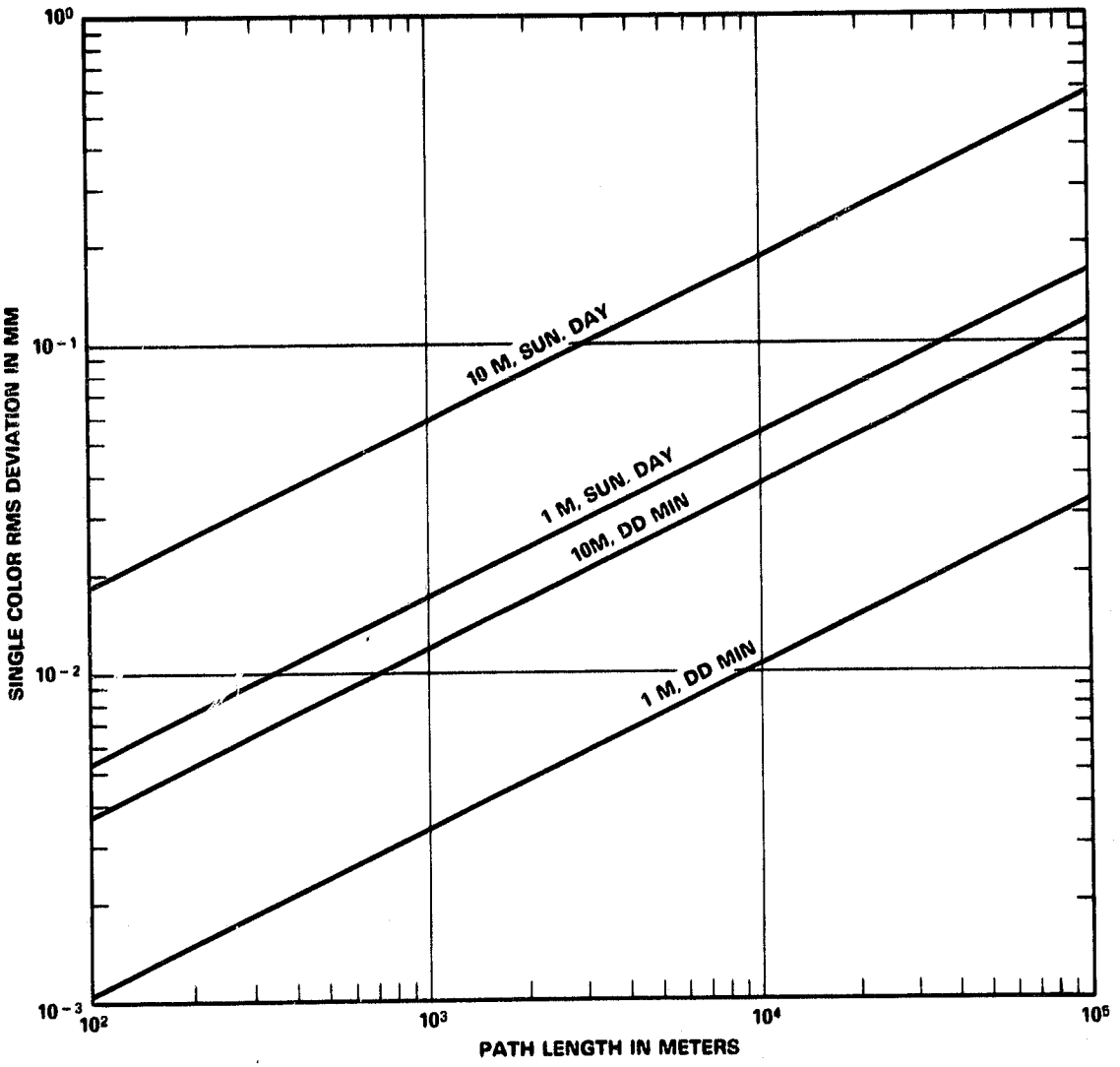

Figure 3.5. Single color turbulence induced rms path deviations versus path length. Values are plotted for a sunny day and the dawn-dusk minimum, and for 1 and 10 meter beam heights above the ground.

$$\left\{1 - \rho_{\Delta L}\right\}_{VK} \approx \left\{\Gamma(1/6)/[2^{5/3}\Gamma(11/6)]\right\} (\Delta z/L_0)^{5/3}$$

$$= 1.864(\Delta z/L_0)^{5/3}. \tag{3.42}$$

For the GT spectrum, $B_{\Delta L}$ can be found by substituting (3.36) into (3.32). The result is

$$\left\{1 - \rho_{\Delta L}\right\}_{GT} = 1 - \pi^{-1} \int_0^{\infty} d\theta \; \frac{U[1/6, -2/3, -i(\Delta z/L_0)\cos\theta]}{U[1/6, -2/3, \theta]}. \tag{3.43}$$

Here U is a confluent hypergeometric function.

For $\Delta z << L_0$, this result can be simplified to

$$\left\{1 - \rho_{\Delta L}\right\}_{GT} \approx 0.2093(\Delta z/L_0)^{5/3}. \tag{3.44}$$

The correlation coefficient decreases more slowly with Δz for the GT spectrum than for the VK spectrum, which results in the smaller numerical coefficient.

The final expressions for the mean square fluctuations in the path differences for $\Delta z << L_0$ can be found by using these intermediate results. For the VK spectrum, using (3.42) and (3.37) in (3.39) gives

$$\langle \Delta L_{ij}'^2 \rangle_{VK} = 5.831 \; (\Delta z)^{5/3} \; C_n^2(0) \; L. \tag{3.45}$$

For the GT spectrum, using (3.44) and (3.38) in (3.39) gives

$$\langle \Delta L_{ij}'^2 \rangle_{GT} = 5.509 \; (\Delta z)^{5/3} \; C_n^2(0) \; L. \tag{3.46}$$

The similarity of the results for the two spectra is at first glance surprising. However, the result is based on the different correlation lengths of the two spectra. The GT spectrum has a longer correlation length than the VK spectrum, and also has a higher single-color mean-square error. However, the longer correlation length also causes the two colors to undergo more highly correlated turbulence. This higher correlation compensates for the larger single color fluctuation, and gives very nearly the same result for the mean square path length difference as the VK spectrum.

The rms differential turbulence error given by (3.45) is plotted versus path length for several temperature lapse rates in Figure 3.6. It shows that the turbulence error can introduce 0.1 to 1 mm differential errors for paths of 20 to 50 km. This error is magnified by the dispersion multiplier when solving (3.26) for L. For the 355 and 1064 nm wavelengths, the multiplier's value is 7.43. For two-way ranging, the values shown in Figure 3.6 should be multiplied by $\sqrt{2}$.

A plot summarizing the curvature and turbulence errors for both single and two color ranging systems is shown in Figure 3.7. The temperature lapse rate chosen for the comparison was -0.10 deg. C/m, and the single color system was assumed to be 1 m above the ground and operating on a sunny day. The errors shown in the figure will increase for higher lapse rates or for higher beam elevations. The path curvature errors are bias errors, and their value should be doubled for two-way ranging. The turbulence errors are rms values, and should be multiplied by $\sqrt{2}$ for two-way ranging. The dashed line shows the accuracy limit of 1 part per million typical of commercial single-color systems. This error limit corresponds to an average path temperature uncertainty of 1 deg. C.

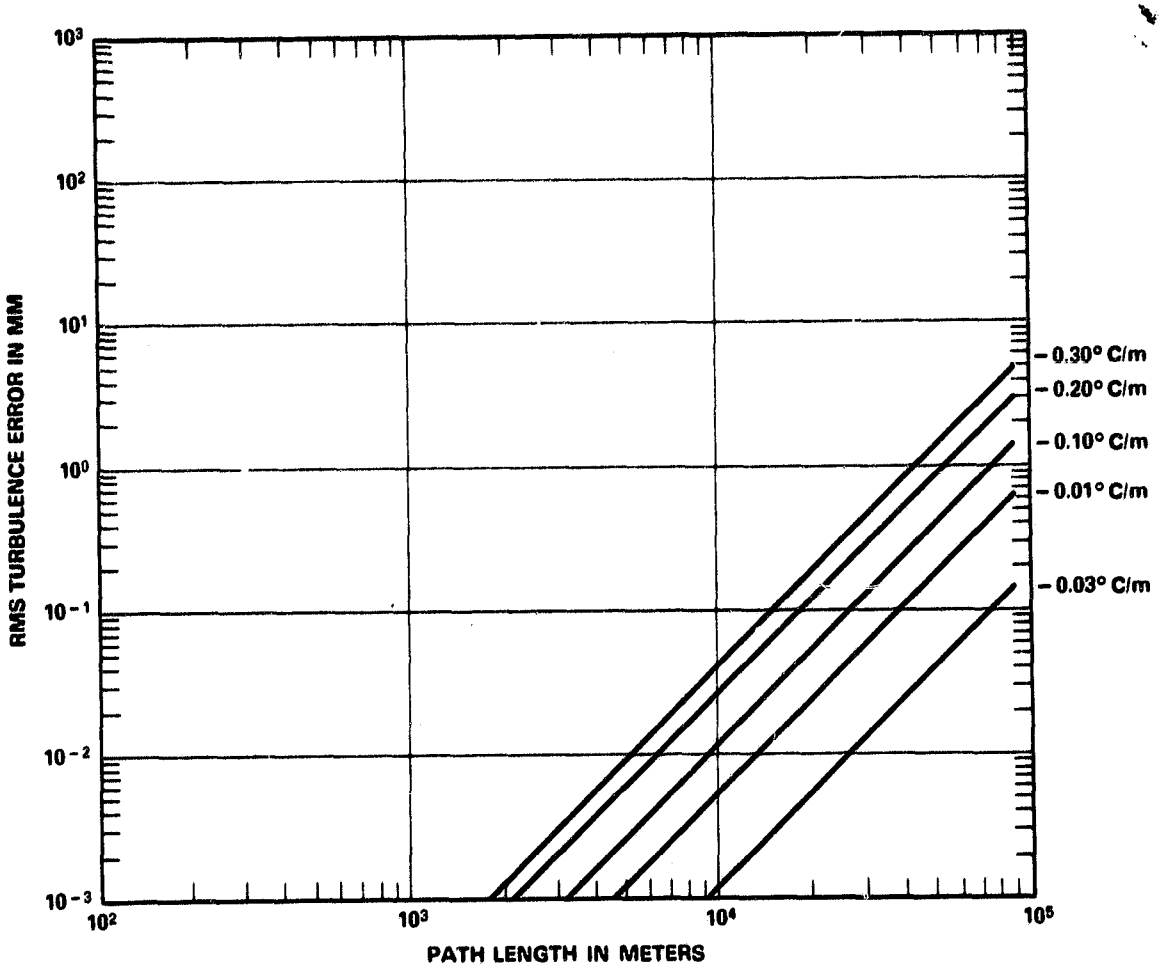

Figure 3.6. Differential path turbulence error versus path length for two color ranging. The wavelengths chosen are 355 and 1064nm, and several temperature lapse rates are considered. These plots are valid for $\Delta z << L_0$.

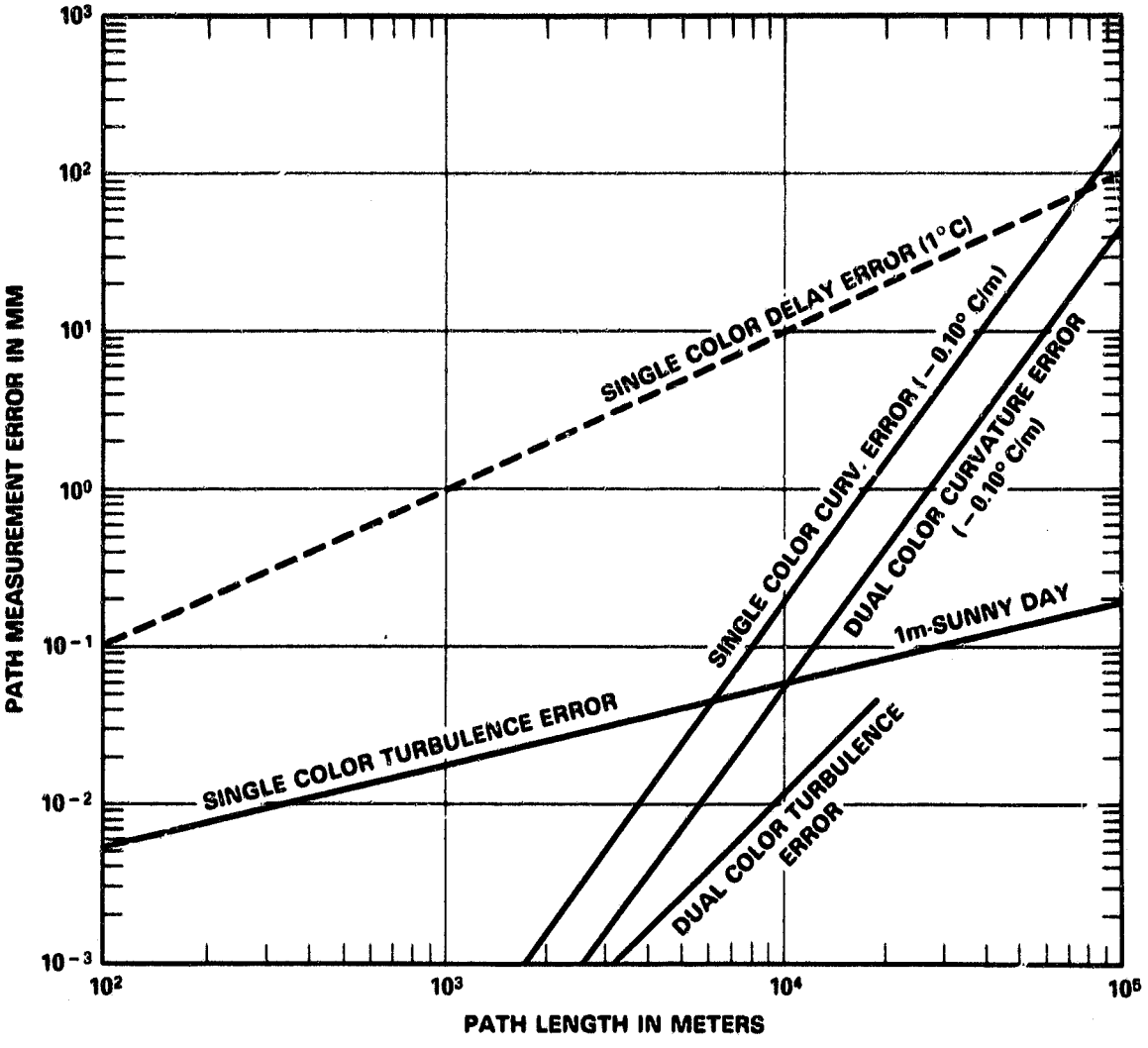

Figure 3.7. Comparison of path curvature and turbulence errors for single and dual color laser ranging systems. When $\Delta z \geq L_0$, the dual color turbulence error is $\sqrt{2}$ · single color turbulence error.

Chapter 3 References

3.1 M. Born and E. Wolf, Principles of Optics, 5th Ed., Pergamon Press, Oxford (1975), Chapter 3.

3.2 V. I. Tatarski, The Effects of the Turbulent Atmosphere on Wave Propagation, (Translation), Keter Press, Jerusalem (1971), Chapter 3.

3.3 G. D. Thayer, "Atmospheric Effects on Multiple-Frequency Range Measurements," ESSA Tech. Rep. IER56-ITSA 53 (1967).

3.4 E. Berg and J. A. Carter, J. Geophys. Res., Vol. 85, 6513 (1980).

3.5 C. S. Gardner, Appl. Opt., Vol. 15, 2539 (1976).

3.6 Tatarski, op. cit., Chapter 1.

3.7 A. Ishimaru, IEEE Trans. Ant. Propagation, Vol. AP-21, 47 (1973).

3.8 R. E. Hufnagel, "Restoration of Atmospherically Degraded Images," Woods Hole Summer Study (1966), Vol. 2, Appendix 3.

3.9 E. Brookner, Appl. Opt., Vol. 10, 1960 (1971).

CHAPTER 4

INSTRUMENT DESIGN AND OPERATION

A pulsed three-color ranging system was constructed and tested for this research. The objectives for building this system were both to verify the theoretical instrument performance analysis and to determine the technical limits in measuring the atmospheric delay. This chapter describes the design and operation of this system in detail.

The prototype system utilized a dye mode-locked, frequency-tripled ND:YAG laser transmitter, a 30cm diameter receiver telescope, and three static crossed-field photomultiplier detectors. The detector outputs were processed by the timing electronics system. This system measured the total path delay for the 532nm pulses and the differential delay between the 1064 and 355nm pulses. This information was used to estimate both the path length and the refractive correction for the path.

4.1 Laser Transmitter

The laser transmitter was the source of the 1064, 532, and 355nm pulses used for the path measurements. The design of the laser is shown in Figure 4.1, and detailed specifications are given in Table 4.1.

When the laser is triggered, its flashlamps are fired, and the 1064nm radiation rapidly increases within the oscillator cavity. This cavity contains both a dye cell to force mode-locking, and an etalon to control the width of the oscillator pulses. The dye used in the cell was Kodak A9740 in a chlorobenzene solution. For these tests the intracavity etalon was adjusted to give pulses of a nominal 65psec width. The optical output from the oscillator contains 6 to 12 of these pulses with a pulse separation time of 7nsec.

The Pockels cell is triggered by the oscillator output pulse train. It and the output polarizer pass only a single output pulse and attenuate the remaining input pulses by 20 times.

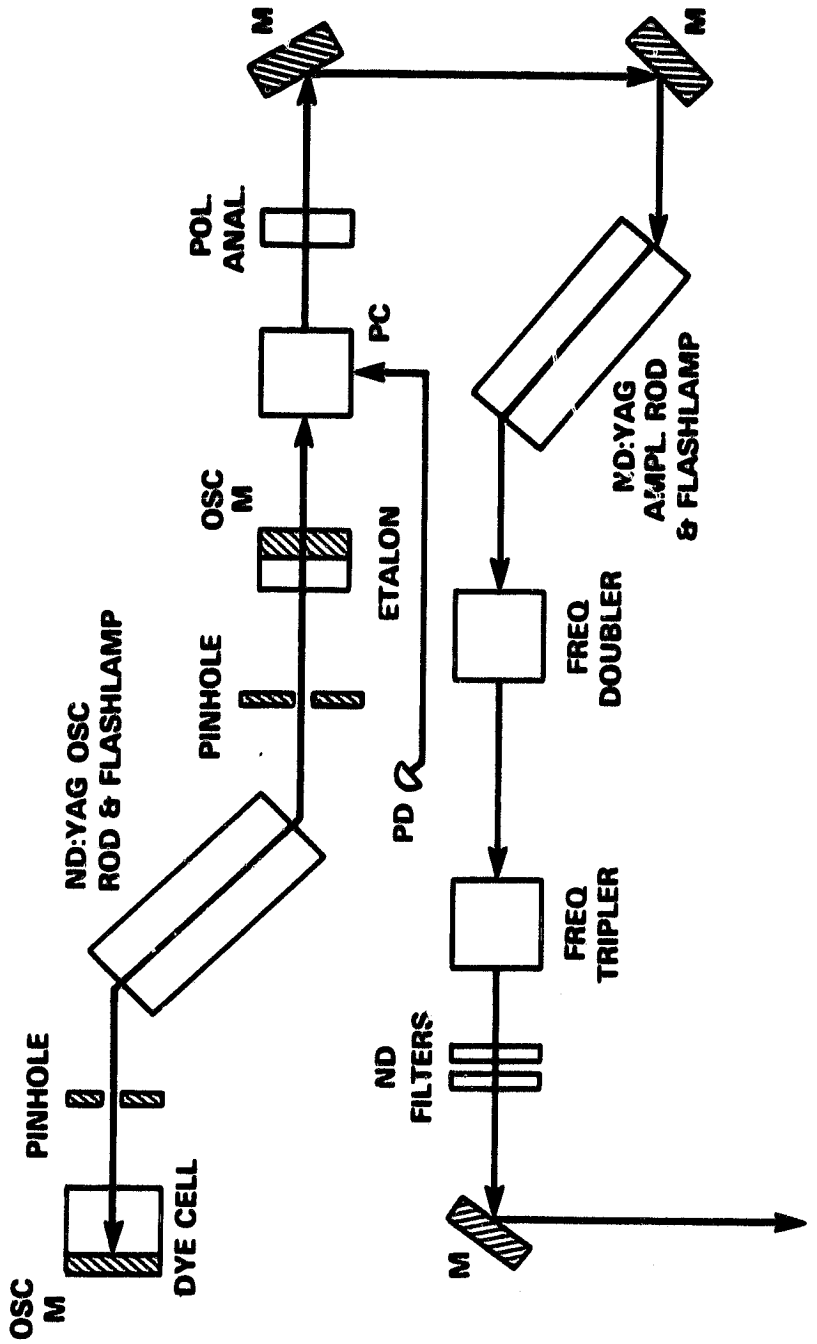

Figure 4.1. Dye modelocked, frequency-tripled ND:YAG laser transmitter.

Table 4.1
Laser Specifications

Manufacturer:	Quantel International, Model YG40.
Dye type:	Kodak Q-Switch-1 A9740.
Dye cell:	40 cm^3 volume with magnetic stirrer.
Laser rods:	ND:YAG, 1% ND ion conc., 6 mm diameter, 65 mm long, ends AR coated and cut at 6 degree angle.
Flashlamps:	Helical, Xenon filled.
Etalon:	1.5 mm thickness.
Oscillator pulses:	7 (nominal).
Oscillator pulse energy:	1 mJ maximum.
Pulse selector:	Krytron driven Pockels cell, triggered on laser optical output.
Amplifier gain:	10 with 1 mJ input pulse.
Harmonic conversion crystals:	KD*P - Type 1.
Output energy:	6 mJ at 1064 nm, 3 mJ at 532 nm, 1 mJ at 355 nm.
Output pulse width:	60 - 70 psec (nominal).
Repetition rate:	36 pulses per minute.

The energy of the selected pulse is then increased ten times in the amplifier assembly. This output pulse, which has approximately 10 mJ energy, is then input to the frequency doubler. This crystal harmonically converts 30% of the 1064 nm pulse energy to 532 nm.

The two pulses which exit this crystal are next input to a frequency tripling crystal. This unit is identical to the doubling crystal. It converts 30% of the 1064 and 532 nm pulse energy to 355 nm. The nominal laser output is 6 mJ at 1064 nm, 3 mJ at 532 nm, and 1 mJ at 355 nm. The three output pulses are coincident in time, since the two harmonic pulses were produced by 2 photon processes from the 1064 nm pulse. To

prevent damage to the final metal turning mirror, the energy in the three pulses is attenuated by a filter before they exit the transmitter assembly. A photograph of the laser is shown in Figure 4.2.

4.2 Optical System

After leaving the laser, the output pulses are first sent into the optical system shown in Figure 4.3. Here a beam splitter reflects approximately 1% of the output pulse energy and directs it into the reference optical path. In this path, a second beam splitter reflects approximately 1% of the energy to a photodiode, which registers the laser firing time in the receiver electronics package. A list of the specifications of the components used in the optical system is given in Table 4.2.

The remainder of the pulse energy is then attenuated, and passes through the reference path shutter. This device is used to block the reference pulses when ranging over horizontal paths. When the shutter is open, the pulses are reflected into the receiver detector assembly. Here the pulses are first reflected from a beam splitter and the 355nm pulse is reflected from a dichroic beam splitter. This pulse is then attenuated and focussed onto the 355nm photomultiplier. A narrow-band filter attached to the detector is used to reject background light.

The 532 and 1064nm pulses are transmitted by the first dichroic splitter, and the 532nm pulse next is reflected by a second dichroic splitter. This pulse is then attenuated and passes through a narrow-band filter. It is then detected by the second photomultiplier.

The 1064nm pulse passes through this second splitter, and is then attenuated, narrow-band filtered, and focused onto the third photomultiplier. All the photomultiplier outputs are processed by the receiver electronics package. The details of this package are given later in this chapter. A photograph of the optical system is shown in Figure 4.4.

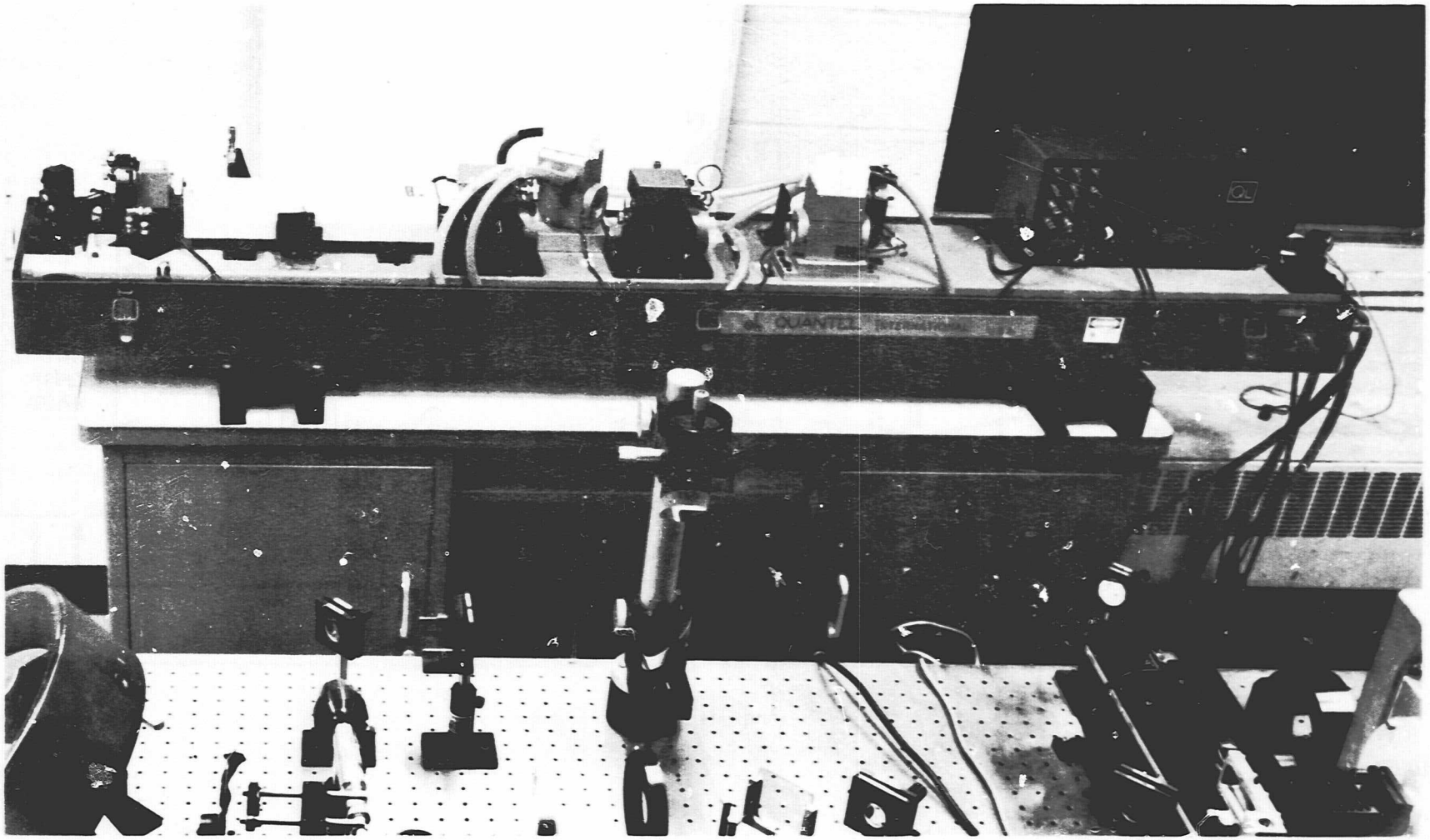

Figure 4.2. Photograph of three color laser transmitter used in the phototype system. The large box in the rear contains the pulse slicer assembly, and the beam exits toward the optical table in the foreground from the mirror at left-front of the laser.

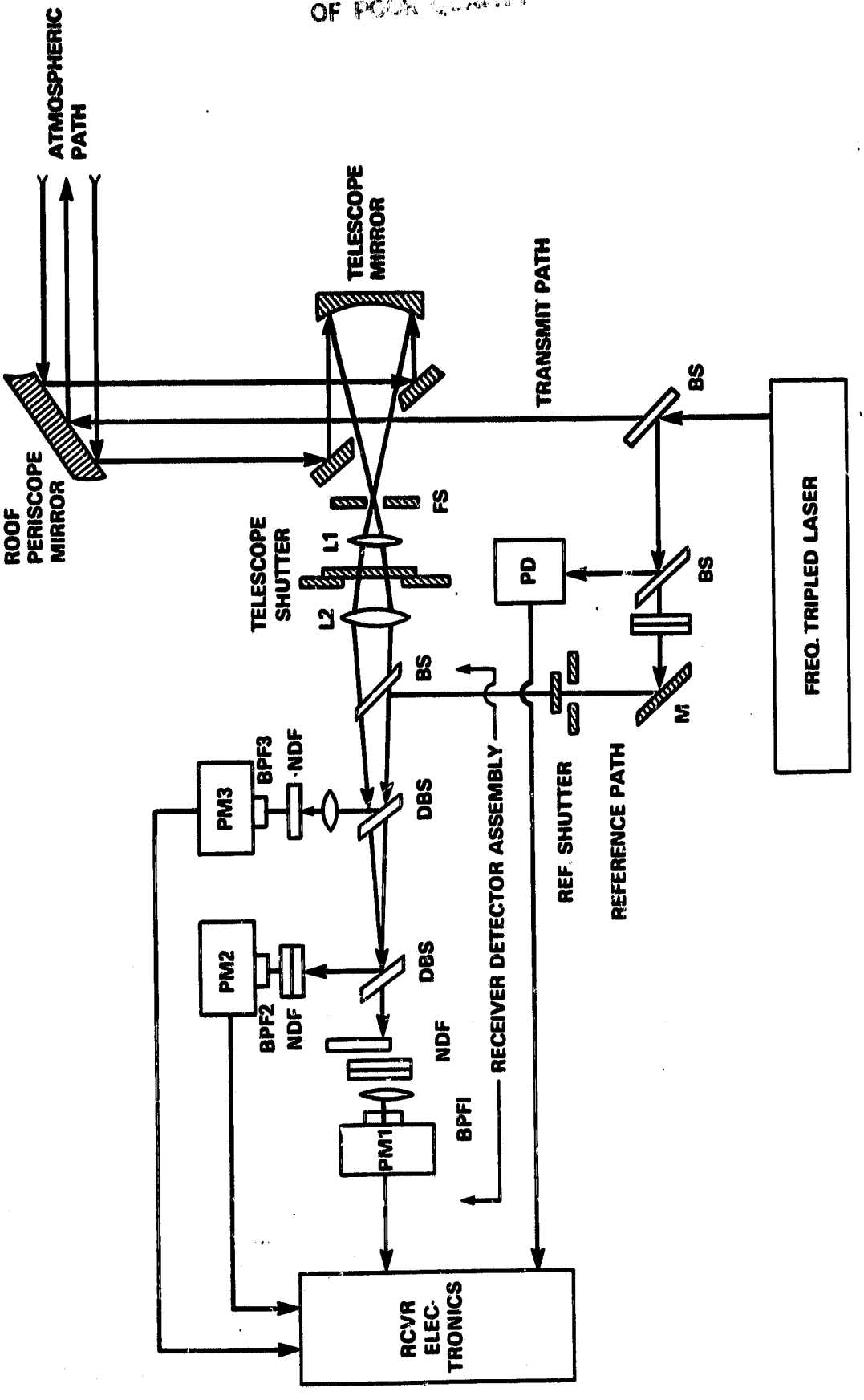

Figure 4.3. Optical system configuration.

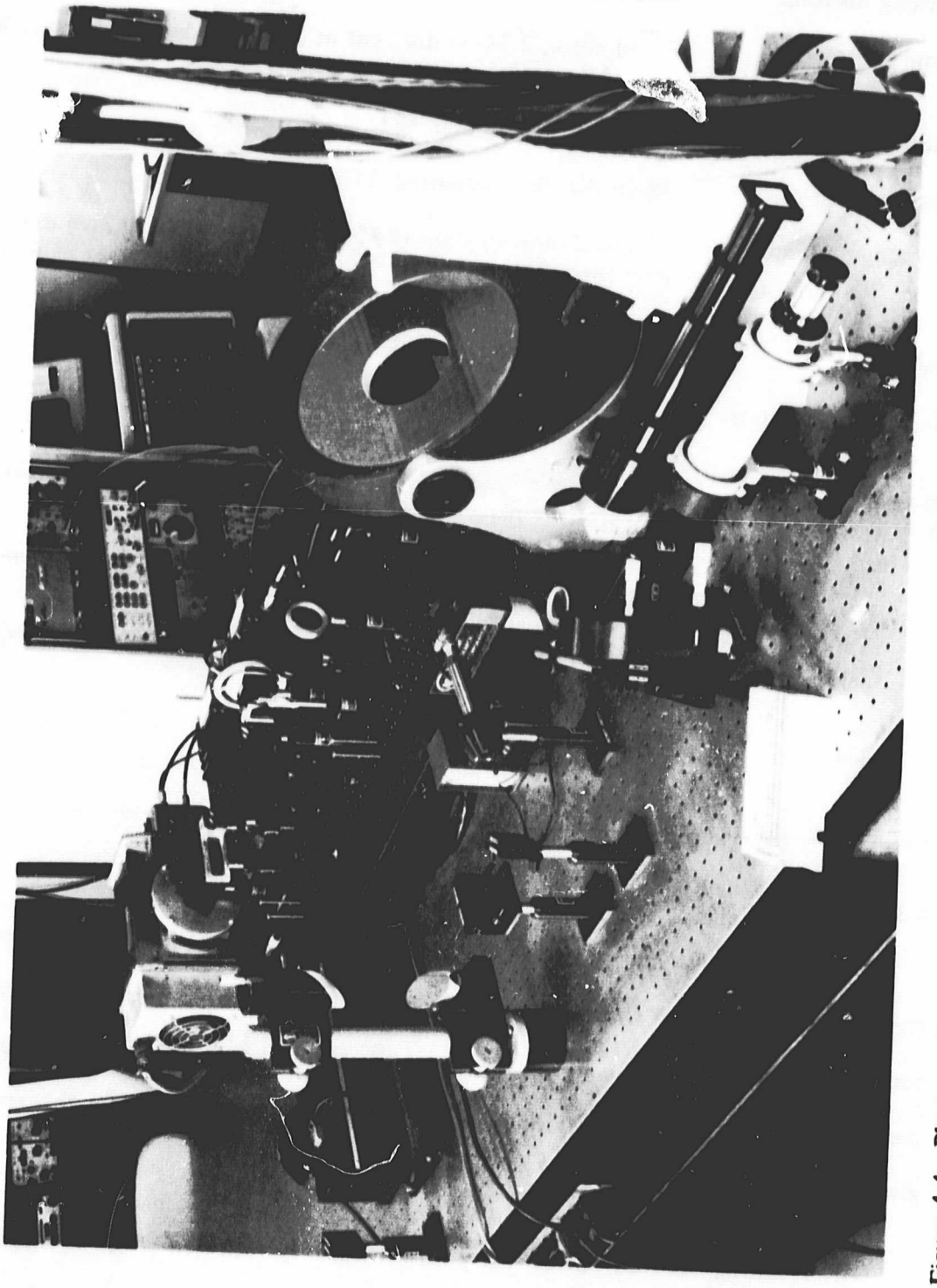

Figure 4.4. Photograph of the optical components of the prototype system. The 1064 nm detector is contained in the light colored cooled housing in the upper left hand corner of the photograph. The receiver telescope mirror is out of the photograph at the right hand edge.

Table 4.2
Optical System Specifications

Turning mirrors:	Enhanced Al surface.
Beam splitters:	Fused silica, 2.54cm dia., cut at 2 deg. wedge, single layer broad-band AR coating on both surfaces.
Photodiode:	Spectra Physics Model 403.
Roof mirror:	38cm dia. flat, enhanced Al surface.
Telescope assembly:	Elliptical cross-section (30.5cm dia. flat with 10.2cm dia. center hole turned at 45 deg.), 459 sq. cm collection area, 91.4cm focal length.
Field stop:	0.16cm dia., restricts telescope FOV to 1.78mrad.
Narrow-band filters:	355nm: 10nm FWHM, 532nm: 2nm FWHM, 1064nm: 2nm FWHM.
Photomultipliers:	Varian static crossed-field, Nominal electron multiplication gain: 2.0 E5 to 5.0 E5, nominal impulse response: 160psec.
PM3:	Model 154D/2.6G, S-20 photocathode, Quantum Efficiency: 17% at 355nm.
PM2:	Model 154A/1.6L, InGaAsP photocathode, Quantum Efficiency: 12% at 532nm.
PM1:	Model 154A/5.6Z, InGaAsP photocathode, Quantum Efficiency: 2.8% at 1064nm, mounted in cooled housing at approx. -10 deg. C.

4.3 Transmitter and Atmospheric Paths

Most of the pulse energy from the laser passes through the first beam splitter. From there the pulses are sent through the transmit path to a periscope mirror mounted on the roof of the laboratory. This mirror was steered to allow atmospheric delay measurements over several available horizontal paths. A list of the paths used for this research is given in Table 4.3.

After exiting the roof mirror, the pulses traverse the selected path. A fraction of the transmitted energy is reflected by a corner reflector at the end of the path. This energy is returned over the path and is reflected by the roof mirror into the receiver telescope

Table 4.3
Horizontal Paths Used for Atmospheric Delay Measurements

Path:	Location:	Round Trip Length:	Elevation Angle:
Receiver calib.	Building roof	193 m	0.00 deg.
Short Atm Meas.	Parking lot	921 m	3.50 deg.
Long Atm Meas.	Park. lot, Woods	4760 m	-0.29 deg.

assembly. The returned pulses next pass through a field stop, and through the receiver shutter into the receiver detector assembly. The receiver pulses traverse this assembly in the same way as the reference pulses.

For best timing performance, the reference and return optical paths are adjusted to be as close to spatially coincident as possible in the receiver assembly. Separations between the paths here cause a bias between the reference and receiver pulse separation times. This bias is caused by the difference in photomultiplier transit times when it is illuminated at different photocathode locations.

4.4 Receiver Electronics

The photomultiplier outputs are processed by the receiver electronics system shown in Figure 4.5. After the laser fires, the photodiode output triggers the start discriminator in this system. It's output signal then starts both the time interval unit and the stop gate generator.

The 532nm detector output is used to stop the time-interval-unit and to trigger the waveform digitizer. A range gate configuration is used after the discriminator to reduce false triggering from the photomultiplier noise pulses. This gating unit operates in two modes. In the reference mode, a short cable delay is used for the gate delay. This allows only the reference output from the photomultiplier to pass through the gate. In the target mode, the generator output enables the discriminator pulse to pass only during the expected return time for the target pulses. This time is preset in the gate delay unit.

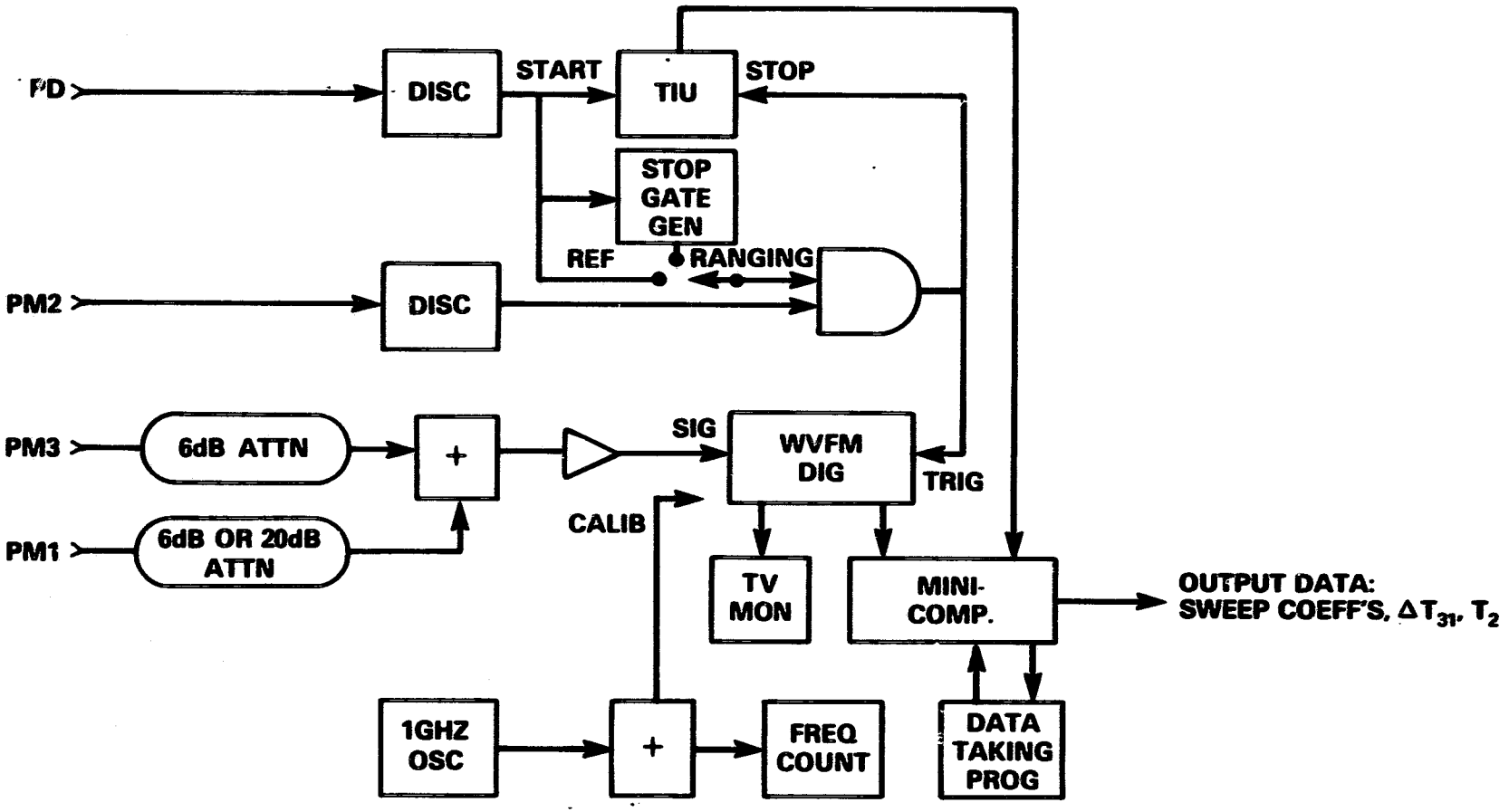

Figure 4.5. Receiver electronics configuration.

The output from the range gate is used to stop the time interval measurement, and to trigger the waveform digitizer. More details on the components used in the receiver electronics package is given in Table 4.4.

The 355 and 1064nm detectors outputs are used for the dispersion measurement. In the system their outputs are first attenuated, and then electrically summed by a power splitter. The fixed optical and electrical delays in the system cause the 1064nm pulse to be delayed in time by approximately 2nsec after the 355nm pulse output. The resulting double peaked waveform at the output of the power splitter is then amplified and recorded by the waveform digitizer. A typical recorded waveform is shown in Figure 4.6. The waveforms input to the digitizer are available for viewing in real-time on a TV monitor, or can be recorded by the system minicomputer through an interface.

The digitizer operates in the same manner as a high speed oscilloscope, except that it writes the recording electron beam onto an array of solid-state detectors instead of a phosphor screen. This detector array is then scanned on the reverse side by a second electron beam to read the stored data. The recording array has 512 elements in the x-direction, which corresponds to 51.2 elements per x-division. There are 480 elements in the y-direction, which corresponds to 60 elements per y-division. For this research, the time base of the digitizer was set at 500psec/div., which corresponds to a time resolution of approximately 9.2psec per digitizer element.

The output data from the digitizer and the time-interval-unit are read by the minicomputer. The ranging program processes the data to extract the total single-color range delay and the differential pulse delay caused by atmospheric dispersion in the path. A photograph of the receiver electronics rack and the minicomputer system is shown in Figure 4.7.

Table 4.4
Receiver Electronics

Calibration source:	1GHz VCO, manually tuned and referenced to frequency counter.
Amplifier:	Hewlett-Packard 8447F, 26dB gain, 0.1-1300MHz bandwidth.
Power splitter:	Weinschel 1515, DC-18GHz bandwidth.
Discriminators:	Ortec 934, constant fraction type.
Time interval unit:	Hewlett-Packard 5370, 100psec accuracy.
Stop gate generator:	Ortec 416A Gate and Delay generator.
Waveform digitizer:	Tektronix R7912 with 7A29 and 7B15 plug-ins, 600MHz bandwidth, used at 500psec/div sweep speed.
Minicomputer:	Digital Equipment Corporation Minc-11, with LSI 11/23 processor and 64K words memory, used with RT-11 operating system.

4.5 Calibration

The dispersion measurement requires timing accuracy at the picosecond level. To permit this accuracy, special calibration procedures were developed for the waveform digitizer. The calibration methods compensated for errors in both the sweep unit and the vertical amplifier response of the digitizer.

The slightly nonlinear digitizer sweep speed profile was measured by using a 1GHz calibration sine wave as an input. The location of the sine wave peaks were found in the digitized data. From this information the number of digitizer elements between successive peaks was computed, and a cubic polynomial was fitted to the sweep-speed profile. A typical calibration waveform and sweep speed calibration data are shown in Figures 4.8 and 4.9. The output data shown in the figure is stored on disk for use by the ranging program after each system calibration. A detailed description of the actions of the calibration program is given in Table 4.5.

The waveform digitizer was also found to have time shifts which were dependent on the input pulse amplitude. If left uncorrected, these effects would introduce up to 66psec

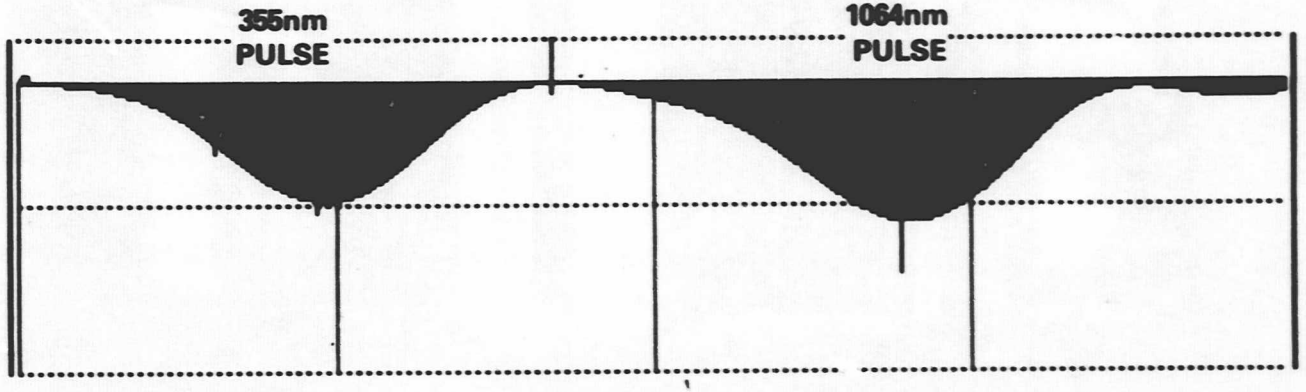

WVFM	50X1	PKX1	SEPX	50X2	PKX2	DT50	DTPK	PKY1	PKY2	#INT	MSEC	USEC	NSEC	PSEC
2	86	129	218	312	360	2052	2122	19	20	13	0	0	17	680
3	80	121	216	308	357	2071	2166	28	33	14	0	0	17	789
4	84	126	218	304	357	1997	2119	27	30	9	0	0	17	750
5	76	118	212	300	349	2035	2111	23	22	12	0	0	17	870
6	84	126	218	304	354	1997	2068	18	37	16	0	0	17	770
7	80	123	217	303	351	2025	2085	20	26	12	0	0	17	809
8	84	128	216	301	353	1969	2059	29	35	11	0	0	17	789
9	90	130	219	315	357	2043	2082	12	24	17	0	0	17	680
10	126	169	259	345	395	1996	2144	29	26	22	0	0	17	809
11	87	130	218	307	355	1996	2061	25	28	11	0	0	17	770
12	84	126	214	306	356	2015	2109	16	35	16	0	0	17	750
13	80	122	215	307	355	2062	2136	23	25	14	0	0	17	709
14	80	122	211	308	358	2071	2167	17	28	6	0	0	17	750

Figure 4.6. Typical waveform and timing data recorded by ranging program. Full scale in X is 5000 psec. Full scale in Y is 8 digitizer divisions (400 mV).

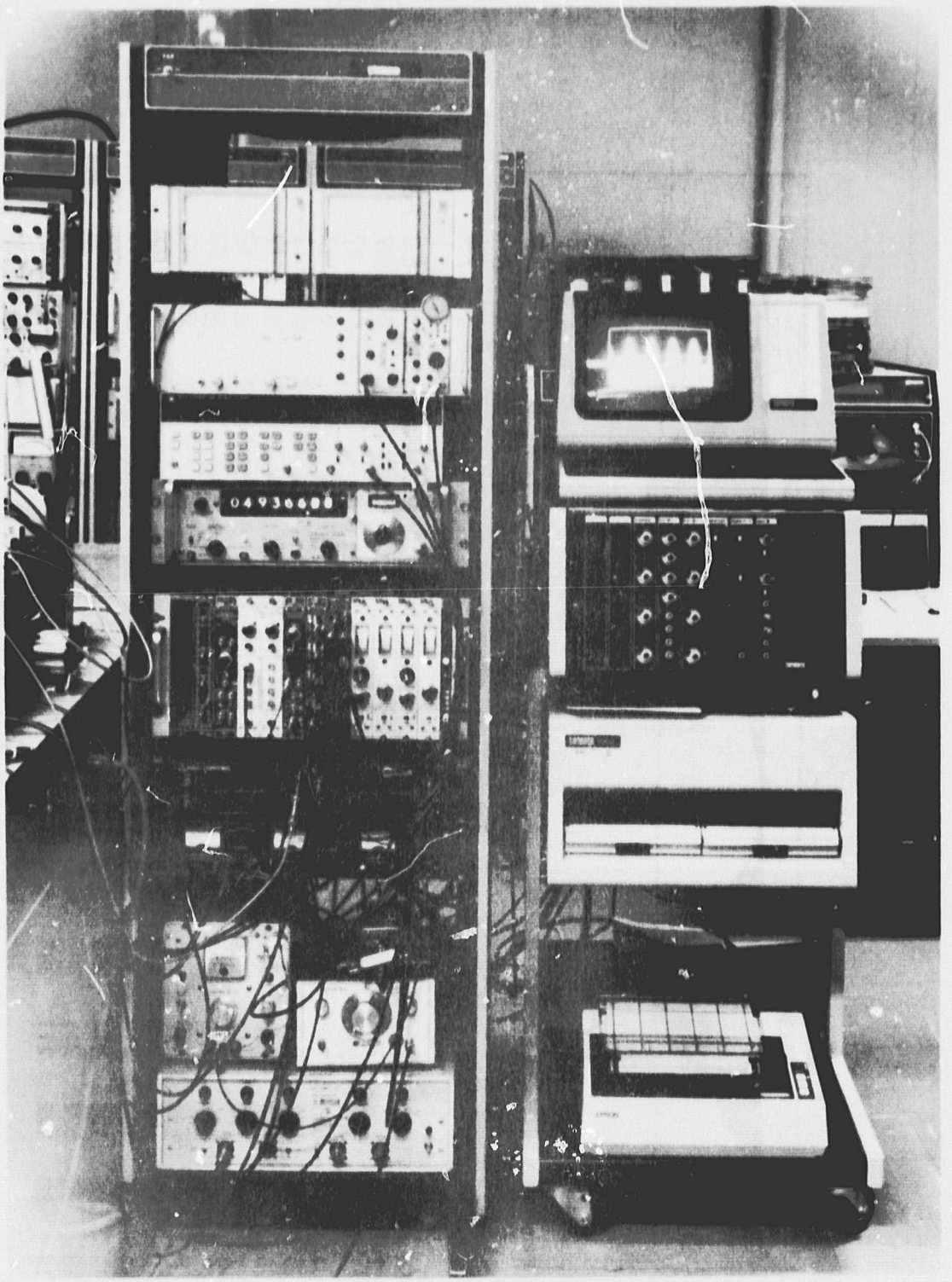

Figure 4.7. Photograph of the electronics and minicomputer of the prototype system. The electronics rack contains the waveform digitizer displays, the digitizer, time-interval unit, frequency counter, and NIM electronics from top to just below table level. The minicomputer contains the display, processing unit, disc drive and printer.

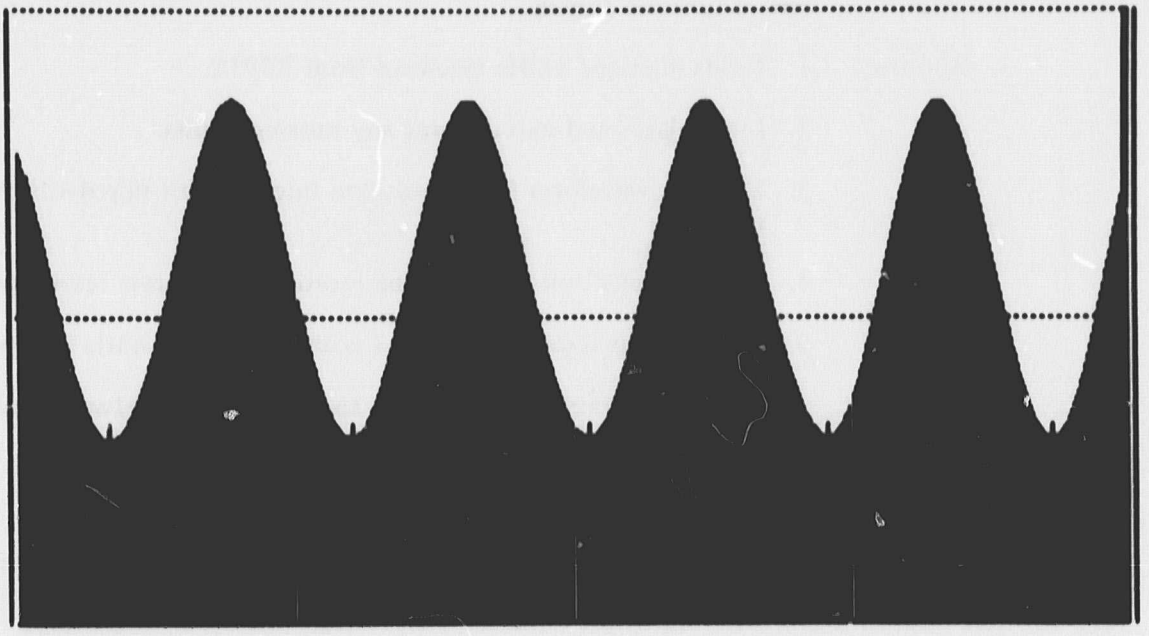

Figure 4.8. Typical 1 GHz calibration waveform as recorded by calibration program.

SWEEP SPEED POLYNOMINAL COEFF'S (0 TO 3) IN PSEC/(DIGITIZER ELEMENT):

8.458189, 1.1455715E – 02, – 5.6947283E – 05, 8.5335920E – 08

Date & Time: 17-NOV-81 15:27

STATISTICS OF PEAK POSITIONS:

MEAN (EL#):	**43.08**	**152.80**	**262.14**	**372.21**	**476.53**
ST DEV (EL):	**0.17**	**0.13**	**0.15**	**0.28**	**0.17**
CENTER POS (EL):	**97.9**	**207.5**	**317.2**	**424.4**	
PSEC/EL:	**9.11**	**9.15**	**9.09**	**9.59**	

AVERAGE AMPLITUDE = 276 ELEMENTS

Figure 4.9. Calibration program analysis of 20 digitized waveforms.

Table 4.5
Receiver Sweep-Speed Calibration Program Specifications

Purpose:	Calibrates sweep speed of waveform digitizer with sufficient accuracy to permit picosecond timing.
Actions:	1. Reads digitized 1 GHz sinewave from R7912.
	2. Interpolates and extrapolates any missing points.
	3. Smooths waveform by convolution integral with raised-cosine impulse response.
	4. Locates waveform minima time locations to nearest resolution element.
	5. Locates high resolution minima positions by quadratic interpolation.
	6. Prints and stores peak positions and sweep rates between peaks, and plots sample waveforms.
	7. Repeats steps 1 through 6, 10 to 20 times.
	8. Computes mean and standard deviations of peak positions and sweep rates, prints and stores data.
	9. Fits third degree polynomial to sweep speed data points, and prints and stores coefficients.

of measurement error when the input pulse amplitude changed from 0.6 to 5.5 screen divisions. In ranging operation, the measured values of time-shift versus pulse amplitude are used to correct for this instrumentation bias. Typical measurements of this error are shown and discussed in Chapter 6.

4.6 Ranging Operation

For ranging, the three color system is used in two modes. In the reference mode, the objective is to measure the fixed electrical and optical delays in both the single color (532 nm) and the dispersion (355 and 1064 nm) channels. This is accomplished by closing the telescope shutter, and setting the range gate to the cable delay setting. The ranging program outlined in Table 4.6 is then started, and it records approximately 200 measurements of the fixed system delays. Comparisons of successive reference measurement sets also are useful indicators of the system timing stability.

Table 4.6
Ranging Program Specifications

Purpose:	**Reads the time interval unit and data waveforms from the digitizer, extracts the pulse separation times, and stores the data.**
Actions:	**1. Reads stored sweep speed coefficients.**
	2. Reads time-interval unit.
	3. Reads newly digitized double-pulse waveform from R7912.
	4. Interpolates and extrapolates missing waveform points, and smooths waveform by convolution integral with 100 psec wide raised cosine pulse.
	5. Finds time occurrence of pulse minima, pulse amplitudes, 50% risetime points, and separation point of pulses.
	6. Computes actual separation time between pulse peaks by using data from step 5, and polynomial sweep speed and amplitude corrections.
	7. Prints and stores waveform timing data.
	8. Repeats steps 2 through 7, 100 to 200 times.
	9. Plots summary histograms of 50% risetime and peak timing points.
	10. Calculates means and standard deviations of plotted timing data.

In the ranging mode, the reference shutter is closed, and the telescope shutter is opened. The delay module output is then used as the range gating signal. Usually the levels of the 355 and 1064 nm signals must be adjusted with the variable attenuators at the entrance to the detectors so that the detected signal levels will fall within the 11:1 dynamic range of the waveform digitizer. The same ranging program is used for this mode as for the reference mode, and 200 measurements of range delay and dispersion are also recorded.

The atmospheric dispersion causes the 355 nm pulses to travel more slowly in the path than do the 1064 nm pulses. Since the system is configured with the 355 nm pulses being recorded first, their pulse position shifts toward the 1064 nm pulses on the digitizer. Therefore the measured pulse separation times are smaller for the atmospheric path than for the reference path.

The difference between the mean values of the ranging and reference values give the dispersion in the atmospheric path, and the total path delay at 532nm. These values are compared against previously recorded ones, and values predicted from endpoint atmospheric measurements to determine the performance of the ranging system. Figure 4.10 shows typical histograms and statistics of 200 system measurements for both the reference and the short atmospheric ranging path. A detailed analysis of the system performance is given in the next chapter.

4.7 Data Analysis

It was necessary to examine the stored timing data in detail for developing the instrumentation system and for monitoring its operation. A special data analysis program was developed for this purpose, and an outline of its operations is given in Table 4.7. This program was used to determine the limitations of dispersion measurements caused by the systematic errors in the timing system.

The capabilities both to examine time drifts in the recorded data and to perform scatter plots were necessary to calibrate the timing system. For example, the basis for the amplitude correction algorithm used in the ranging program was the data from plotting the measured change in pulse separation time versus pulse amplitude. Such a capability was also useful for examining data sets which deviated widely from expected instrument performance.

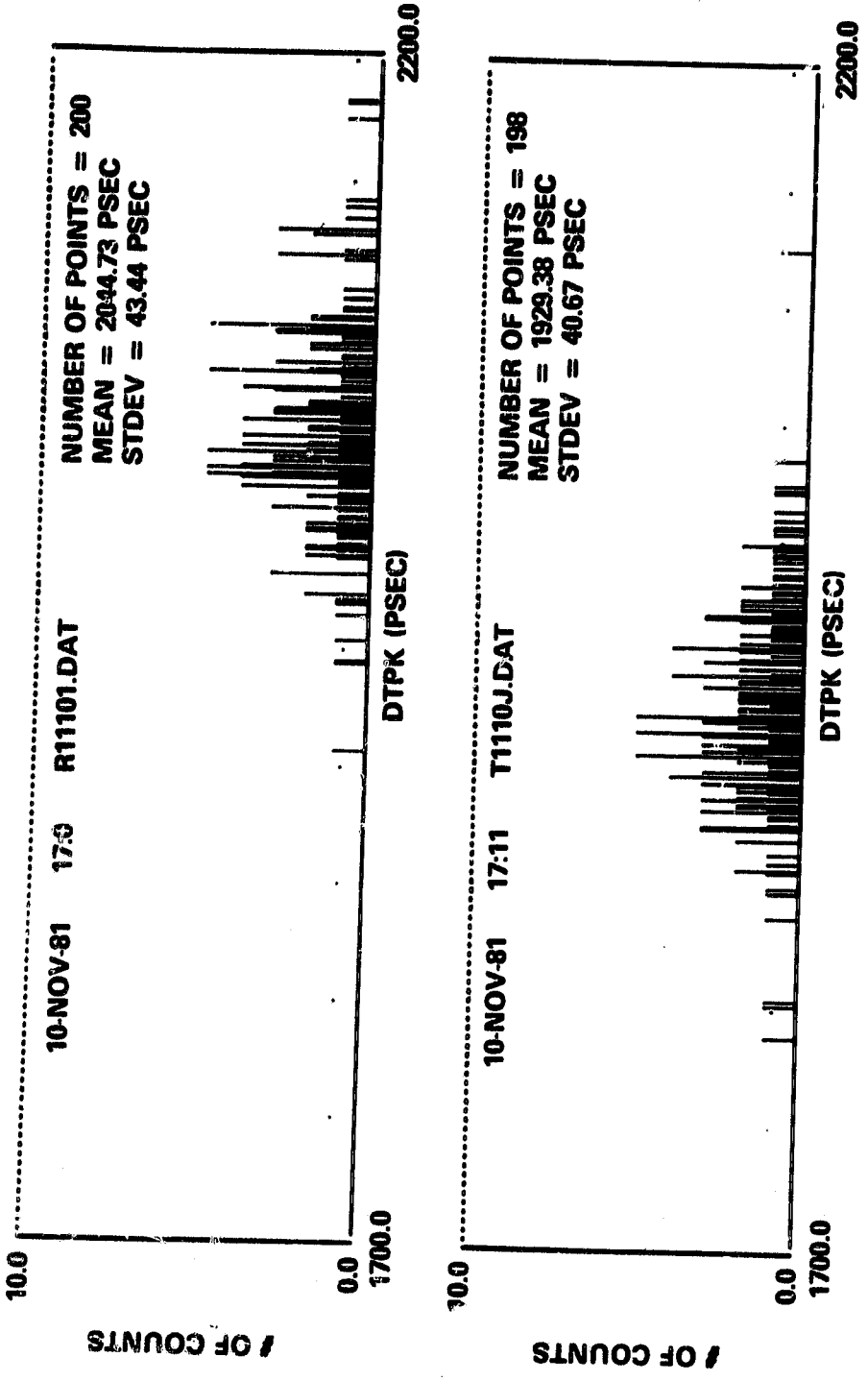

Figure 4.10. Typical histograms for 200 reference and ranging path measurements.

Table 4.7
Data Analysis Program Specifications

Purpose:	Analyzes waveform timing data in order to permit maximum measurement accuracy and to monitor receiver performance.
Actions:	1. Reads stored waveform timing data.
	2. Plots selected columns of stored data as either (a) histogram, (b) time history, or (c) scatter plot.
	3. Computes statistics on values of items selected in options (a) and (b) in step 2.
	4. Fits least-squares polynomial curve to items selected in options (b) and (c) in step 2. Calculates goodness-of-fit statistic and prints polynomial coefficients.

CHAPTER 5

THEORY OF INSTRUMENT PERFORMANCE

The performance of any optical ranging system is determined by several factors. These include the fundamental accuracy limits caused by the statistical nature of the photodetection process, as well as limits imposed by atmospheric turbulence, background light, and instrumentation imperfections. The expressions for the measurement accuracy, maximum range, and detection and false alarm probabilities of the prototype multicolor ranging system are developed in this chapter.

5.1 Ideal Receiver - Single Measurement Accuracy

The accuracy of any optical ranging system is limited by the finite number of received signal photons. Even if the multicolor system were constructed of ideal equipment, these would limit its measurement performance. The performance level of an ideal pulsed optical ranging system is derived in this section.

For a maximum-likelihood optical receiver system [5.1], the expected value of the measured optical pulse arrival time is given by

$$\langle T_m \rangle = T_a. \tag{5.1}$$

Here the actual arrival time of the optical pulse is denoted as T_a. The angle brackets denote averaging over the ensemble of photoelectron distributions possible for the optical pulse shape. Since the expected value of the measured pulse arrival time is equal to the actual optical pulse arrival time, the ideal receiver is unbiased.

This measurement has a finite variance due to the finite number of signal photoelectrons observed. For a raised-cosine optical pulse with full width at half maximum (FWHM) of w, the variance of its time extent is given by

$$\mathrm{Var}(\tau_p) = w^2/\pi^2. \tag{5.2}$$

The variance of a maximum-likelihood receiver [5.1] operating with such a photon limited pulse is given by

$$\mathrm{Var}(T_m) = \mathrm{Var}(\tau_p)/[b + n - \sqrt{b(b + 2n)}]. \tag{5.3}$$

Here n is the expected number of received signal photoelectrons, and b is the expected number of background photoelectrons observed during the full pulse width 2w. For most laser receivers [5.2] operating in the multiphotoelectron regime, $n \gg b$. Under this assumption, (5.3) can be simplified to

$$\mathrm{Var}(T_m) = \mathrm{Var}(\tau_p)/n. \tag{5.4}$$

Therefore the magnitude of the measurement variance is inversely proportional to the number of detected photoelectrons per pulse.

Measurement of the atmospheric delay in the prototype system requires measurement of the differential arrival tim between the 335 and 1064nm pulses. For the ideal receiver, the mean measured arrival time difference is given by

$$\langle \Delta T_m \rangle = \Delta T_a. \tag{5.5}$$

Therefore, it is equal to the actual arrival time difference between optical pulses.

The errors in estimating the arrival times of the two photon limited pulses are independent. Therefore their variances add, and the variance of the differential measurement is given by

$$\mathrm{Var}(\Delta T_m) = \mathrm{Var}(\tau_{p1})/n + \mathrm{Var}(\tau_{p2})/m. \tag{5.6}$$

Here n and m are the number of photoelectrons generated upon reception of pulses p1 and p2. This expression shows that for an ideal receiver system, the error in the differential delay measurement can be made arbitrarily small. This can be accomplished either by decreasing the transmitted pulse widths at each color, or by increasing the number of receiver photoelectrons at each color, or by doing both.

5.2 Actual Receiver - Single Measurement Accuracy

Non-ideal receivers introduce several additional errors to the previously given lower bound. These errors are contributed primarily by the photomultipliers and the external timing system, and both bias the receiver measurement and increase its variance. The expressions for the prototype multicolor system single measurement errors will be developed in this section.

Photomultiplier detectors contribute a bias to arrival time measurements which is equal to the signal delay in the photocathode and dynode chain. The mean measured pulse arrival time for a timing system using such detectors can be written as

$$\langle T_m \rangle = T_a + \langle \tau_{PM} \rangle. \tag{5.7}$$

Here τ_{PM} is the photomultiplier delay. For this derivation, it is assumed that the variance of the photomultiplier output pulse occurrence time can be written as

$$\mathrm{Var}(T_m) = [\mathrm{Var}(\tau_{pl}) + \mathrm{Var}(\tau_{PM})]/n. \tag{5.8}$$

In this equation $\mathrm{Var}(\tau_{PM})$ represents the variance of the timing jitter contributed by the photomultiplier detector. This variance can be assumed to be additive to the detection timing variance if the timing fluctuations in the detector are independent of the statistics of the photodetection process. The photomultiplier timing fluctuations are due to the statistical nature of the secondary electron multiplication process occurring within the detector.

The two color receiver is composed of two such photomultipliers used with an external timing system. For such a system, the measured difference in the mean arrival times of the optical pulses is given by

$$\langle \Delta T_m \rangle = \Delta T_a + \langle \Delta \tau_{PM} \rangle + \tau_c + \langle \tau_d \rangle. \tag{5.9}$$

In this expression τ_c represents the fixed bias in the measured differential arrival time caused by the fixed optical and electrical delays in the prototype system. The timing delay introduced by the digitizer is denoted by τ_d.

The variance of the differential delay measured by the actual receiver is determined by the magnitudes of photomultiplier and digitizer time jitters. By using (5.8), and by assuming that the digitizer timing jitter is independent of the number of detected photoelectrons in each pulse, the receiver timing jitter can be written as

$$\mathrm{Var}(\Delta T_m) = [\mathrm{Var}(\tau_{p1}) + \mathrm{Var}(\tau_{PM1})]/n + [\mathrm{Var}(\tau_{p2}) + \mathrm{Var}(\tau_{PM2})]/m + \mathrm{Var}(\tau_d). \qquad (5.10)$$

For the prototype system, this single measurement timing error is too large to make useful single atmospheric delay measurements. Therefore the system used the average value of several individual measurements to infer a single value of atmospheric delay.

5.3 Averaged Measurement Accuracy

The variance of the measured atmospheric delay can be reduced by data averaging, if the observations are independent, and if the atmospheric delay is stationary over the observation interval. In this section, the expressions for the mean and variance of such an averaged measurement set will be derived under these assumptions.

The mean difference between the measured arrival times of the two pulses can be calculated by taking the expected value of (5.9). Solving the resulting equation for the optical pulse separation time yields

$$\langle \Delta T_a \rangle = \langle \Delta T_m \rangle - \langle \Delta \tau_{PM} \rangle - \tau_c - \langle \tau_d \rangle. \qquad (5.11)$$

Here the angle brackets denote averaging over the N individual instrument measurements.

The variance of the averaged measurement set is related to the single measurement variance by

$$\mathrm{Var}(\langle \Delta T_m \rangle) = (1/N^2) \sum_{i=1}^{N} \mathrm{Var}(\Delta T_{mi}). \qquad (5.12)$$

By using (5.10) in this result, the general expression for the variance of the set of N measurements can be written as

$$\mathrm{Var}(\langle \Delta T_m \rangle) = \mathrm{Var}(\tau_d)/N + (1/N^2) \sum_{i=1}^{N} [\{ \mathrm{Var}(\tau_{p1}) + \mathrm{Var}(\tau_{PM1}) \} /n_i + \{ \mathrm{Var}(\tau_{p2}) + \mathrm{Var}(\tau_{PM2}) \} /m_i]. \quad (5.13)$$

For the prototype system, the optical pulse widths and detector characteristics at both colors were similar. Therefore, to first approximation

$$\mathrm{Var}(\tau_{p1}) + \mathrm{Var}(\tau_{PM1}) \approx \mathrm{Var}(\tau_{p2}) + \mathrm{Var}(\tau_{PM2}) \equiv \mathrm{Var}(\tau_p). \quad (5.14)$$

To further simplify (5.13), an equivalent photoelectron number can be defined by the relationship

$$(1/q) \equiv (1/n) + (1/m). \quad (5.15)$$

This is the number of photoelectrons which would be required in a single color system to give the same timing variance as a two color system which received photoelectron levels n and m in each pulse. By using (5.14) and (5.15), (5.13) can be simplified to

$$\mathrm{Var}(\langle \Delta T_m \rangle) = \mathrm{Var}(\tau_d)/N + [\mathrm{Var}(\tau_p)/N] \left\{ (1/N) \sum_{i=1}^{N} (1/q_i) \right\}. \quad (5.16)$$

One last simplification can be made by introducing an average equivalent photoelectron number, Q, defined by

$$1/Q = (1/N) \sum_{i=1}^{N} (1/q_i). \quad (5.17)$$

By using this, (5.16) can be rewritten as

$$\mathrm{Var}(\langle \Delta T_m \rangle) = (1/N)[\mathrm{Var}(\tau_d) + \mathrm{Var}(\tau_p)/Q]. \quad (5.18)$$

Equations (5.11) and (5.18) describe the theoretical timing performance of the measurement system.

5.4 Averaged Ranging Measurement Accuracy

For the prototype system, the values of the system biases are not known *a priori*. Therefore two sets of averaged system measurements were used to recover the differential

atmospheric delay. In the reference measurement, the pulses traverse the same receiver path as for the atmospheric path measurement. The measured difference between the mean pulse arrival times gives the sum of the offsets between the detector responses. By using (5.11), this mean offset can be written as

$$\langle \Delta T_{m,r} \rangle = \langle \Delta \tau_{PM,r} \rangle + \tau_c + \langle \tau_{d,r} \rangle. \tag{5.19}$$

For ranging over the atmospheric path, the actual differential pulse delay is the difference of the reference delay and that contributed by the atmospheric dispersion in the path. Therefore the measured mean separation time can be written as

$$\langle \Delta T_{m,p} \rangle = \langle \Delta \tau_{PM,p} \rangle + \tau_c + \langle \tau_{d,p} \rangle - \langle \Delta T_{atm} \rangle. \tag{5.20}$$

Since the occurrence time of the 355nm pulse is measured first in the prototype system, the atmospheric dispersion causes the pulse pair to move closer together in time. Therefore the average atmospheric delay can be found by subtracting the path measurement from the reference measurement. The resulting expression for the atmospheric delay value is

$$\langle \Delta T_{atm} \rangle = [\langle \Delta T_{m,r} \rangle - \langle \Delta T_{m,p} \rangle] - [\langle \Delta \tau_{PM,r} \rangle - \langle \Delta \tau_{PM,p} \rangle] - [\langle \tau_{d,r} \rangle - \langle \tau_{d,p} \rangle]. \tag{5.21}$$

The last two bracketted terms represent the difference in the mean differential detector delays and the difference in the digitizer delay between the reference and path measurements. Any changes in these terms over the time period between these measurements will bias the average dispersion measurement.

One cause of detector delay changes is the dependence of the photomultiplier delay upon the optical spot position on its photocathode. Since the reference and atmospheric paths can have different intensity distributions and can illuminate different photocathode positions, these will introduce a bias error. Changes in the digitizer delay can be caused by unmodelled amplitude-dependent biases in the waveform digitizer. Such biases will cause reference and atmospheric path data sets with different average pulse amplitudes

to have different system delays. The difference in these delays will bias the atmospheric delay measurement.

Since the reference and path measurements are independent, the variance of the dispersion estimate is the sum of the variances of the two measurement sets. Assuming the same number of individual measurements in the reference and path data sets, the variance of the average atmospheric delay measurement is given by

$$\mathrm{Var}(\langle \Delta T_{atm} \rangle) = (1/N)[2\mathrm{Var}(\tau_d) + \mathrm{Var}(\tau_p) \{ 1/Q_r + 1/Q_p \}]. \qquad (5.22)$$

This expression indicates that the variance of the atmospheric delay measurement can be reduced in several ways. These include increasing the size of the reference and path data sets, or increasing the average signal levels in both the reference and path measurements. The variance also can be reduced by decreasing the variance of the digitizer and photomultiplier detectors.

5.5 System Maximum Range

The maximum range of the prototype system is determined by the required number of received photoelectrons at the receiver. This in turn is determined by the length of the measurement path and characteristics of the ranging system. The maximum range of the system is computed in this section, assuming that the target is a single corner reflector.

For a pulsed optical ranging system, the average number of detected photoelectrons per laser firing is given by

$$N_{pe} = \eta[E_{tr}/E_{ph}][G_{tr}/(4\pi R^2)][\sigma_{tar}/(4\pi R^2)] A_{rec}\tau_{sys}\tau_{atm}^2. \qquad (5.23)$$

Here η is the detector quantum efficiency, E_{tr} and E_{ph} are the transmitted pulse and photon energies respectively, R is the one-way target distance, A_{rec} is the receiver area, and τ_{atm} is the one-way atmospheric transmission. The system transmission τ_{sys} is the product of the transmissions of the transmitter, the corner reflector, and the receiver.

For Gaussian beam cross-sections, the transmitter gain and target cross section can be approximated by

$$G_{tr} = 32/\theta_{tr}^2, \tag{5.24}$$

and

$$\sigma_{tar} = A_{cc}(32/\theta_{cc}^2). \tag{5.25}$$

Here θ_{tr} and θ_{cc} are the full width at $1/e^2$ points of the transmitter and corner reflector beam patterns, and it has been assumed that the gains are measured at the center of the beam patterns.

Several terms in (5.23) are wavelength dependent, and therefore the expected number of received photoelectrons will be different for each color. For diffraction limited optics, the beam patterns of the transmitter and corner reflector are wavelength dependent. However, the transmitter and corner reflector are not diffraction limited for the prototype system. Therefore the terms in (5.23) which are wavelength-dependent are η, E_{tr}, E_{ph}, τ_{sys}, and τ_{atm}. The system transmission is the product of all mirror reflectivities, r_{mir}, in the beam path, including the corner reflector and the transmission of the bandpass filter. In the prototype system there are a total of 9 reflections from aluminized mirror surfaces. The one-way atmospheric transmission is given for horizontal paths by $\exp(-s_{atm} R)$, where s_{atm} is the atmospheric attenuation coefficient.

Table 5.1 summarizes the values of the wavelength dependent terms in (5.23). It includes measured values or best estimates of the transmitter energy, the detector quantum efficiencies, and system transmission. The values for s_{atm} were taken for a standard-clear sea-level atmosphere [5.3].

The last column in the table represents a figure-of-merit for the system efficiency in each color. It is the maximum number of receiver photoelectrons available for detection, ignoring all path losses. The column shows that the combined effect of fewer

Table 5.1
Values of the Wavelength Dependent Terms Used in the Ranging Equation

Wavelength (nm)	Quant. Effic.	E_{tr} (mJ)	E_{ph} (xE-19 J)	s_{atm} (1/m)	r_{mir}	r_{sys}	Max(N_{pe}) (xE + 12)
1064	0.02	6	1.87	1.2 E-4	0.90	0.27	173
532	0.09	3	3.73	1.7 E-4	0.85	0.16	117
355	0.18	1	5.59	3.1 E-4	0.65	0.014	4.5

transmitted photons and smaller system transmission limit the maximum received signal in the 355nm channel to 2.5% of that of the 1064nm channel. Since both colors must be received for a dispersion measurement, this channel limits the system's maximum range, even in the absence of atmospheric scattering in the path.

The average number of received photoelectrons in each receiver channel is plotted versus range in Figure 5.1 for the system parameters given in the table. The receiver area was given in Table 4.2, and a 12.7cm (5 inch) diameter cube corner with a full beam angle of 25urad (5 arcseconds) was assumed for the reflector. The plot shows the rapid decrease in signal level due to the exponential decrease in atmospheric transmission. This decrease is much more rapid at long ranges than the R^{-4} range dependence. The 1064nm channel has the longest distance capability due to its higher system efficiency and its low atmospheric transmission losses.

Since the 355nm channel has the highest atmospheric losses and the lowest system capability, it has the shortest maximum range of the channels. The maximum range of the system is limited by this channel to approximately 25km, if an average signal level of 10 photoelectrons is required.

In operating the prototype system, variable optical attenuators preceding each detector were used to set the average signal level in each channel. For the short horizontal path tests described in Chapter 6, typical attenuation values of 1000 to 10,000 were used in the

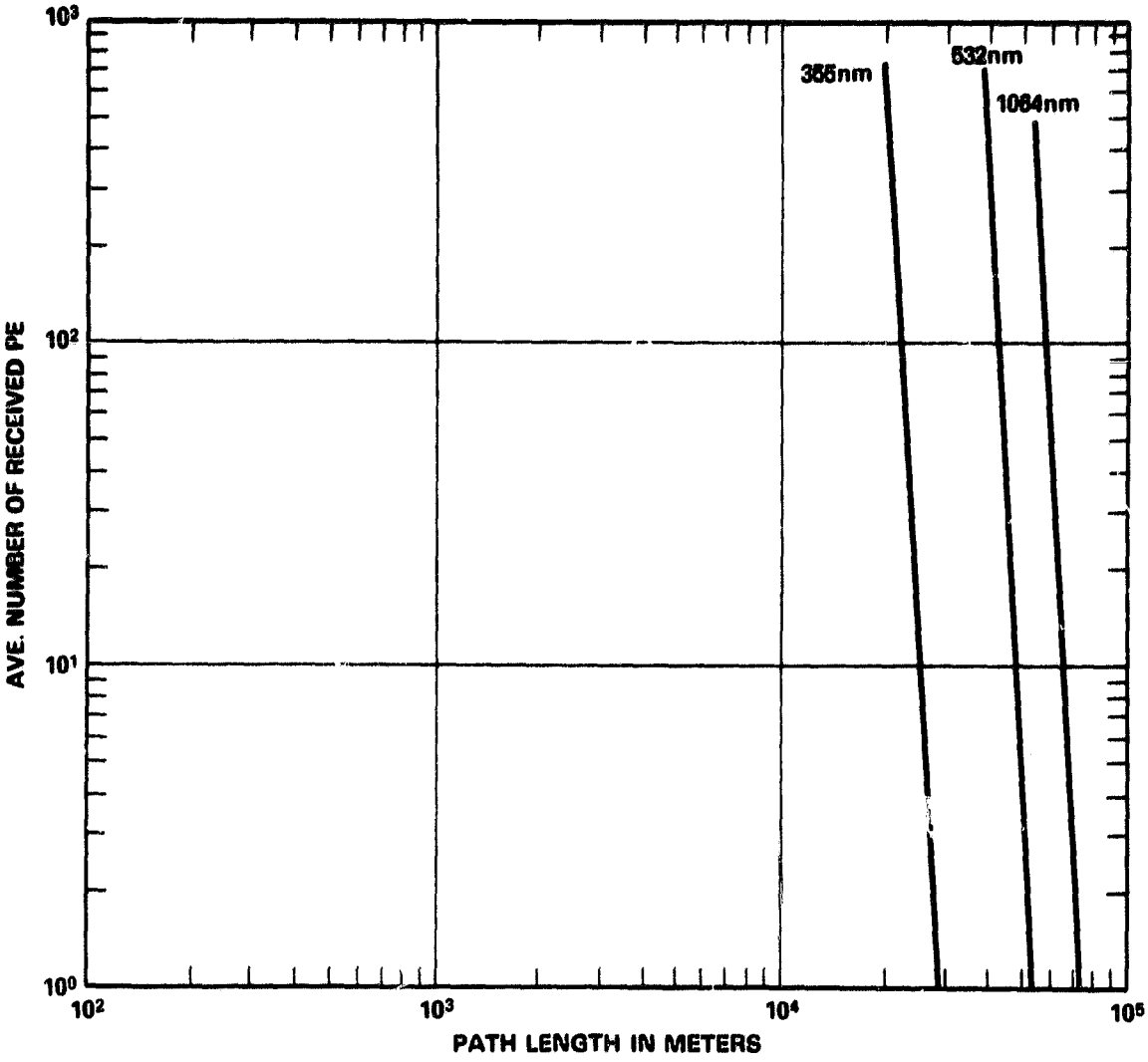

Figure 5.1. Received photoelectron number vs. path length for the three color system ranging to a 5 inch, 5 arcsecond corner cube.

1064nm channel, values of 100 to 1000 were used in the 532 channel, and values of 2 to 100 were used in the 355nm channel.

5.6 Single Channel Detection Probability

The Poisson detection statistics and lognormal atmospheric fading occurring in each receiver channel cause the single-color detection probability to be less than unity. This probability is further limited by the finite dynamic range of the receiver. For the three color receiver, the amplitudes of both the 355 and 1064nm pulses must fall between the receiver's lower and upper thresholds to permit a successful measurement. When the system is properly adjusted, the probability of this occurring is always less than the detection probability in the 532nm channel, and therefore it's statistics dominate the receiver performance. The probability of this event is derived in this section.

For a single channel receiver operating over a free space channel, the detection probability is determined solely by the detection statistics. Assuming an average signal of Q photoelectrons per pulse, the probability of receiving q photoelectrons between the receiver amplitude limits of a and b photoelectrons is

$$\Pr[a \leq q \leq b] = \exp(-Q) \sum_{j=a}^{b} (Q^j/j!). \qquad (5.26)$$

For a receiver with dynamic range D, the upper threshold, b = D · a. Here it was assumed that the receiver can be modelled as a photon counter over the pulse duration w. Recent work by Abshire [5.4] has shown this to be a good approximation for actual maximum-likelihood receivers.

If such a system is operated over an atmospheric channel, the instantaneous signal intensity at the detector also undergoes fading due to atmospheric turbulence. For weak to moderate turbulent strengths (log-amplitude variances ≤ 0.3), it is generally agreed [5.5] that the intensity statistics (and hence the photoelectron levels) of such signals have a lognormal distribution. The probability density is given by

$$f_{LN}(q) = \left\{2q\sqrt{2C_\ell(0)}\right\}^{-1} \exp\left\{-[(1/2)\ln(q/Q) + C_\ell(0)]^2/[2C_\ell(0)]\right\}. \qquad (5.27)$$

Here $C_\ell(0)$ is the log-amplitude variance of the turbulence. For strong turbulence, there is some controversy over the correct form of the probability density [5.6]. Therefore, for sake of simplicity, it will be assumed here that the lognormal distribution is the correct one for turbulent strengths up to saturation.

For a spherical wave transmitter and point detector, it is widely accepted that

$$C_\ell(0) = 0.124\, C_n^2\, k^{7/6}\, L^{11/6}. \qquad (5.28)$$

In this expression, the turbulence was assumed to be homogeneous in the propagation path of length L, k is the wave number of the laser, and C_n^2 is the refractive index structure parameter. Typical values of this parameter are discussed in Chapter 3.

The detection probability for the single color receiver operating over the atmospheric channel is given by

$$\Pr(\text{det } q \mid \text{turb}) = \int_0^\infty \Pr(a \leq q \leq b)\, f_{LN}(q)\, dq. \qquad (5.29)$$

This probability is completely specified by the lower threshold, the system dynamic range, the log-amplitude variance, and the average signal level.

The prototype system has a dynamic range of 11:1, and can operate with its lower threshold as low as 1 to 3 photoelectrons. The single channel detection probabilities for these system parameters are plotted versus mean signal level in Figures 5.2 and 5.3 for several values of $C_\ell(0)$. The figures show that for weak turbulence, the detection probability decreases for mean signals near either threshold.

For stronger turbulence, as Q increases, the detection probability tends to approach a constant value of approximately 0.59 in both figures. This effect is due to the asymmetrical shape of the lognormal distribution, which does not change significantly with Q

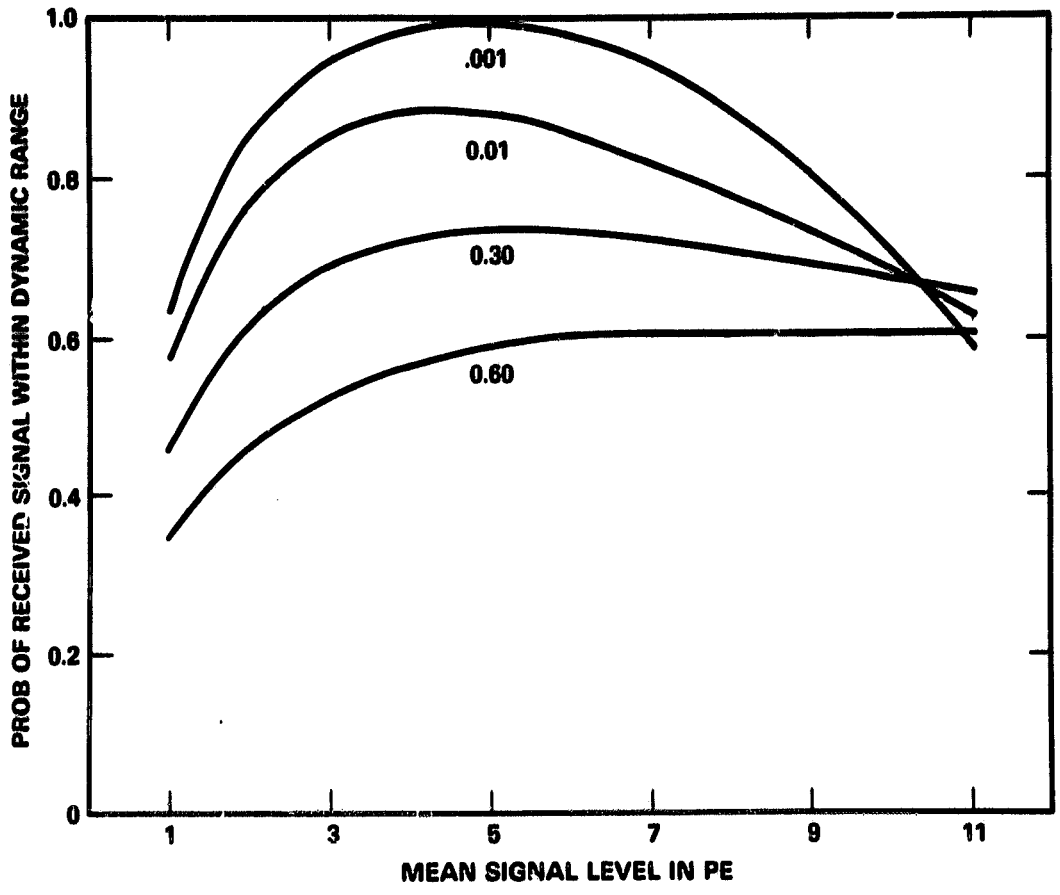

Figure 5.2. Probability of detecting a photon-limited log normally fading signal versus average signal level. The system acceptance range is 1 to 11 photoelectrons, and log-amplitude variance is used as a parameter.

when $C_Q(0)$ is large. However the probability distribution does shift laterally with increasing Q values. In this region, the probability that the signal will exceed the lower threshold when Q is increased is matched by the increased probability that the signal will exceed the upper threshold. Since only the signals which fall between the thresholds will be accepted, the detection probability stays constant in this region. Both figures support the intuitive notion that the mean value of the signal should be placed approximately midway between the threshold values for the highest detection probability.

5.7 Two Channel Detection Probability

In order to measure the pulse separation time on the waveform digitizer, the signal levels of both pulses must have values between the instrument's thresholds. If the

C-2

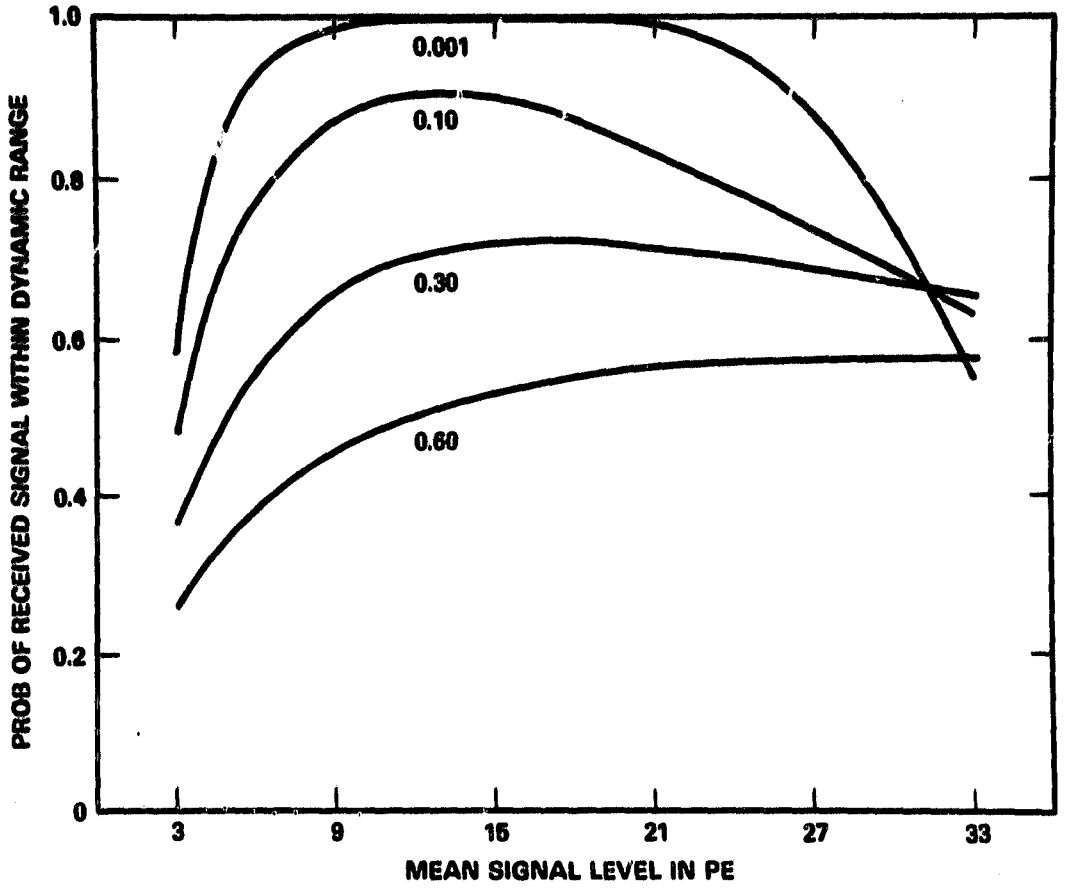

Figure 5.3. Probability of detecting a photon-limited log normally fading signal versus average signal level. The system acceptance range is 3 to 33 photoelectrons, and the log-amplitude variance is used as a parameter.

threshold values of both channels are equal, then the probability of this occurring can be written as

$$\Pr[\text{meas.}] = \Pr[a \leq (q_1 \text{ and } q_2) \leq b] \tag{5.30}$$

$$= \int_0^\infty \int_0^\infty \left\{ \exp(-Q_1) \sum_{j=a}^{b} Q_1^j/j! \right\} \left\{ \exp(-Q_2) \sum_{k=a}^{b} Q_2^k/k! \right\} f_{LN}(q_1, q_2)\, dq_1\, dq_2.$$

Here Q_1 and Q_2 are the expected number of received photoelectrons in each channel, and f_{LN} is the jointly-distributed lognormal probability density. In the above expression, the joint Poisson distribution was written as the product of the marginal distributions, since the detection processes are independent for each channel.

In order to evaluate (5.30), the spectral irradiance correlation coefficient must be examined. This coefficient gives the degree to which the atmospheric turbulence is correlated in the two receiver channels. Fitzmaurice [5.7] has given a convenient form for this coefficient,

$$\rho_{12} = \mathrm{NVAR}[C'_{\ell}(0)\, G(k'')] / \left\{ \mathrm{NVAR}[C_{\ell_1}(0)]\ \mathrm{NVAR}[C_{\ell_2}(0)] \right\}^{1/2}. \qquad (5.31)$$

In this expression, the normalized variance is given by

$$\mathrm{NVAR}[x] = \exp(4x) - 1, \qquad (5.32)$$

and the terms

$$G(k'') = (1 - k''^2)^{7/6}\ (1 - k''^{5/6}), \qquad (5.33)$$

and

$$k'' = |k_2 - k_1|/(k_2 + k_1). \qquad (5.34)$$

In the equations above, $C'_{\ell}(0)$ is the log amplitude variance evaluated at the wave number $k' = (k_1 + k_2)/2$, and the terms $C_{\ell_i}(0)$ are evaluated at wave number k_i.

Equation (5.31) was numerically evaluated for wavelengths 355 and 1064 nm used for the dispersion measurement. The results show that for weak turbulence $\rho_{12} \approx 0.37$, and as the turbulence for wave numbers k', k_1, and k_2 approached saturation, $\rho_{12} \approx 0.11$.

Since the correlation coefficient has a low value, to first order the turbulent fluctuations in each channel can be approximated as being independent. This approximation is somewhat pessimistic, since it slightly underestimates the probability of detection for the two channel system. With this approximation, (5.30) can be written as the product of the individual channel detection probabilities

$$\Pr[\text{meas.}] = \Pr[\text{det } q_1 \,|\text{turb}] \cdot \Pr[\text{det } q_2 \,|\text{turb}]. \qquad (5.35)$$

In this equation, the terms on the RHS are given by (5.29) evaluated at the wavelengths 355 and 1064 nm.

It can be seen from Figures 5.2 and 5.3 that the two color measurement probability is nearly unity for weak atmospheric turbulence when the mean signal levels are centered between the thresholds. For strong turbulence, the measurement probability decreases to a lower bound of 0.36.

5.8 Probability of False Alarm

Background light collected by the receiver causes both false triggering of the receiver, and can degrade the accuracy of the dispersion measurement. The probability of these 'false alarms' occurring in both the trigger (532nm) channel, and in the measurement (355 and 1064nm) channels will be derived in this section.

The false alarm probability can be derived by considering the receiver channel to be a 'sliding window' photon counter. For this receiver model, the receiver is considered to count photoelectron occurrences over the 'window' of its impulse response time, with the window 'sliding' over the receiver observation time. Lee and Schroeder [5.8] have derived the probability of false alarm occurring for this receiver as

$$\begin{aligned} Pr[FA] &= Pr[\text{False Alarm}] \\ &= Pr[(\#\text{ of background counts within w}) \geq L \text{ at sometime during T}] \\ &= 1 - \exp\left\{-[(bT/w)\, b^{L-1}/(L-1)!]/\left[\sum_{k=0}^{L-1} b^k/k!\right]\right\} . \end{aligned} \tag{5.36}$$

In this expression, T is the observation interval, b is the expected number of background counts per pulsewidth w, and L is the receiver threshold. Since for the prototype system, $L \gg b$, (5.35) can be approximated by

$$Pr[FA] = \exp(-b)(bT/w)\, b^{L-1}/\{(L-1)!\} . \tag{5.37}$$

Abshire [5.4] has shown that this approximation was valid for an actual maximum-likelihood laser ranging receiver operating in the region between very low receiver thresholds, where the receiver was saturated with background counts, and high thresholds, where the false alarm probability was dominated by ion-feedback events in the photomultiplier. For the prototype

system, the probability of false triggering can be computed by setting T equal to the range gate window, and b to the noise count number expected for the 532nm channel.

The expected background count in a time interval of the laser pulse width can be computed from

$$b = N_\lambda(\eta/E_{ph})\,\Delta\lambda\,F\,A_{rec}\tau_{rec}\tau_{atm}w. \qquad (5.38)$$

Here N_λ, $\Delta\lambda$, and F are the spectral radiance of the scene, the spectral width of the receiver bandpass filter, and the receiver field-of-view (in steradians) respectively. The remainder of the terms have been defined previously in this chapter. In this equation, it has been assumed that the scattering of light into the receiver from sources outside the receiver field-of-view can be neglected.

The value of N_λ depends upon the scene viewed by the receiver telescope and can be highly variable. For daylight operation, an estimate of the value of N_λ can be computed for several terrain types by considering them to be diffuse Lambertian scatterers. The value of N_λ for each surface then can be computed from tabulated values of the solar spectral irradiance, the spectral dependence of the atmospheric attenuation, the reflectivity of the surface, and the angle between the sun and the receiver line-of-sight.

Table 5.2 contains typical values of solar spectral irradiance and terrestrial surface reflectivities. From these values the terrestrial scene radiance values were computed, which are given in Table 5.3. For these computations, it was assumed that the surface was a 'hillside' at a 30 degree angle from the horizon, and that the sun illuminated the surface at the angle normal to it. The ranging system was assumed to be operating over a horizontal path to a corner reflector mounted on a hillside of the terrian, with the terrian completely filling the receiver field-of-view.

The values of receiver optical power and the expected number of background counts per pulse width computed by using (5.38) are given in Table 5.4 for each channel of the

Table 5.2
Solar Spectral Irradiance and Typical Terrestrial Surface Reflectivities for Wavelengths of Prototype Three Color Ranging System. The * indicates an extrapolated value.

λ (nm)	N_λ (sun) [no atm]	N_λ (sun) [2 air masses]	Diffuse Surface Reflectivity:			
	(mW/sq. m nm)		Snow & Ice	Sand (Quartz)	Alfalfa (June)	Soil After Snow Melt
1064	649	523	0.74*	0.55	0.40*	0.21*
532	1835	1190	0.87	0.29	0.054	0.052
355	1083	213	0.76*	0.12	0.016*	0.015*
Ref:	[5.9]		[5.10]	[5.9]	[5.10]	

Table 5.3
Typical Values of Terrestrial Surface Spectral Radiance Computed from Table 5.2, for a Clear Atmosphere, a 30 Degree Solar Elevation Angle, and a Horizontal Viewing Angle.

λ (nm)	Spectral Radiance [mW/(sq. m ster nm)]:			
	Snow & Ice	Sand	Alfalfa	Soil
1064	107	79	57	30
532	285	95	18	17
355	45	7.0	0.94	0.88

Table 5.4
Calculated Receiver Background Levels for the Prototype System with Field-of-view of an Alfalfa Field. The calculation is the worst case for this scene, since no atmospheric transmission or adjustable receiver attenuator losses were considered.

λ (nm)	N_λ (mW/sq. m ster nm)	Δλ (nm)	τ_{rec}	P_{rec} (nW)	η/E_{ph} (xE + 17)	r_b (pe/nsec)	b (in 0.6 nsec)
1064	57	2	0.51	6.6	1.07	0.71	0.43
532	18	2	0.43	1.8	2.41	0.43	0.25
355	0.94	10	0.19	0.20	3.22	0.065	0.039

prototype system. The values in this table represent worst-case computations for the surface of green alfalfa, since the atmospheric transmission was set to unity, and no adjustable receiver attenuation was assumed. Table 5.4 shows that the expected background counts are maximum for the 1064 nm channel. It also shows that the approximation used in (5.37) is

accurate to better than 10%, for receiver threshold greater than 4 photoelectrons for this channel. The false alarm probability calculated by using the values in Table 5.4 in (5.36) is plotted versus threshold for each receiver channel in Figure 5.4. The plot shows that even for the worst case values, the false alarm probability was less than 10% for thresholds greater than 4 photoelectrons.

With optical attenuation added to the receiver channels, the expected background count rate decreases in proportion to the attenuation value. Since typical attenuation values for the 1064 and 532 nm channels were in the 100 to 10,000 range for the prototype system, the false alarm probability was <0.01 for all receiver channels. Therefore, the false alarm events were not an operational problem for the prototype system.

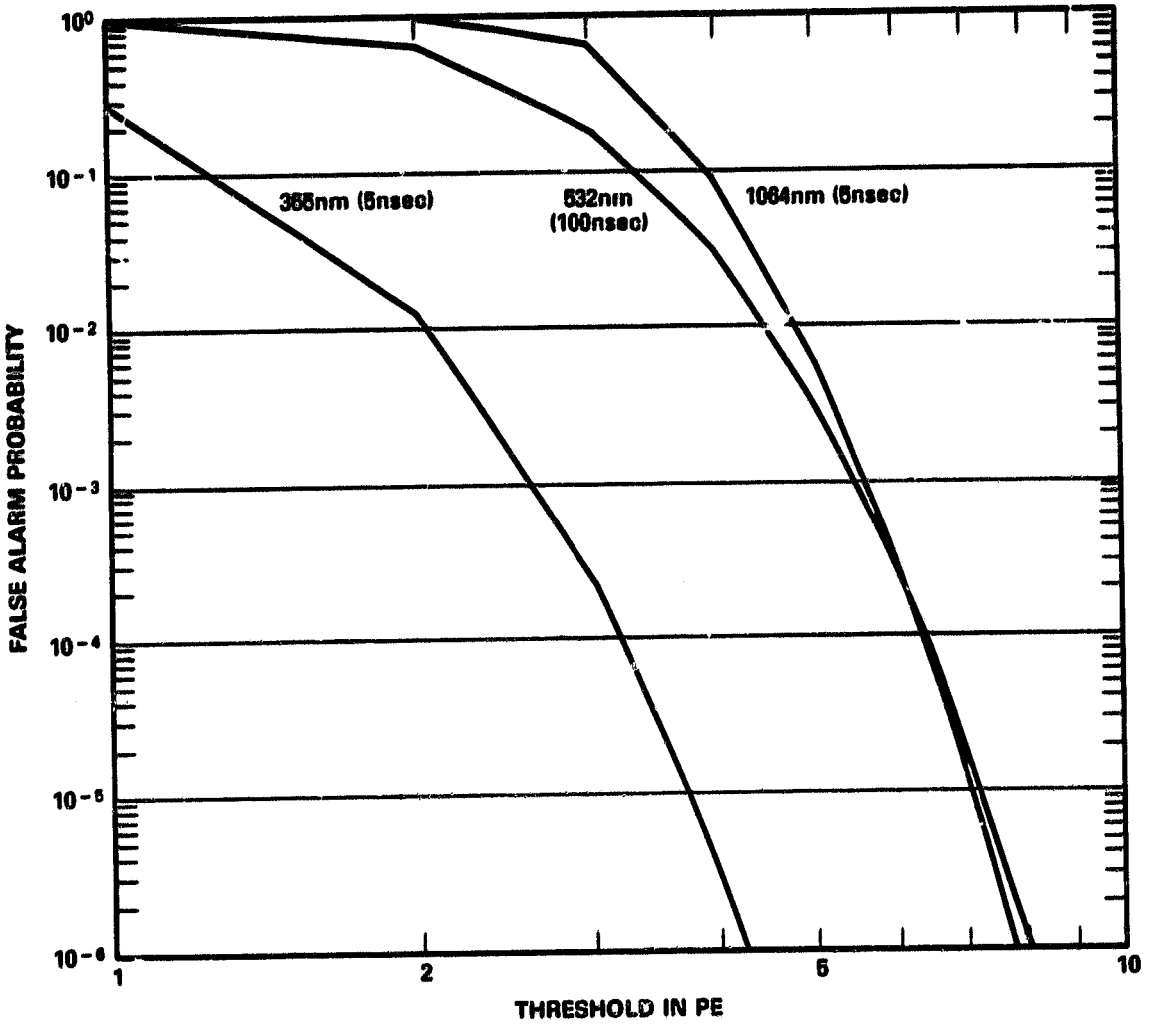

Figure 5.4. Worst case false alarm probability versus threshold for the case of a green alfalfa field completely filling the receiver field-of-view. The values in parenthesis are the observation times.

Chapter 5 References

5.1 I. Bar-David, IEEE Trans. Inf. Thy, IT-15, 31 (1969).

5.2 J. B. Abshire, "A Comparative Study of Optimum and Suboptimum Direct Detection Laser Ranging Receivers," NASA Technical Paper 1315, Sept. 1978.

5.3 RCA Electro-Optics Handbook, (EO-11), Radio Corporation of America, Harrison NJ, 1974, Chapter 7.

5.4 J. B. Abshire, "Comparison of Measured and Theoretical Performance of a Maximum-Likelihood Laser Ranging Receiver," Proc. of the 4th Inter. Conf. on Laser Ranging Instr., Austin TX, Oct. 1981.

5.5 See, for example, R. L. Fante, Proc. IEEE, Vol. 63, 1669 (1975).

5.6 S. F. Clifford and R. J. Hill, J. Opt. Soc. Am., Vol. 71, 112 (1981).

5.7 M. W. Fitzmaurice, "Experimental Investigations of Optical Propagation in Atmospheric Turbulence," NASA Technical Report TR-370, Aug. 1971, Chapter 2.

5.8 G. Lee and G. Schroeder, IEEE Trans. Inf. Thy., Vol. IT-22, 114 (1976).

5.9 W. L. Wolfe and G. J. Zisses, editors, The Infrared Handbook, Office of Naval Research, Arlington, VA, 1978, Chapter 3.

5.10 K. Y. Kondrat'ev, Radiation Characteristics of the Atmosphere and the Earth's Surface, (translation), NASA TTF-678, (1973), Avail. Natl. Tech. Inf. Service, Springfield, VA, pp. 227-229.

CHAPTER 6

MEASURED INSTRUMENT PERFORMANCE

The prototype system was tested to determine its performance limits. First, the system photomultipliers were calibrated in terms of their single photoelectron voltage and time jitter versus photoelectron level. Next, the waveform digitizer was tested for both timing jitter and for calibration stability. Finally, the assembled optical timing receiver was evaluated for both amplitude-dependent time shifts and for timing stability.

The emphasis of the performance tests was on the instrument timing biases and rms jitter. At the beginning of this work, these parameters were the least understood and were judged to be most important of the receiver characteristics. Since the detection probability was found to be greater than 75% when the average optical signal levels were near the midpoint of the receiver's dynamic range, detailed measurements of the detection probabilities were not performed. In practice, this condition was easily achieved by adjusting the optical attenuators preceding the detectors. Detailed false alarm rate measurements also were not performed, since the false alarm probabilities were observed to be very low for the photoelectron levels used in the tests.

The calibrated system timing performance was measured over three horizontal paths of different lengths. The results showed that the instrument bias errors in the differential delay measurements could be reduced to plus or minus 15psec. However, the present design was found to be sensitive to the optical spot positioning in the receiver package. The results also showed that when this is not properly controlled, bias errors as large as 80psec occur. The suboptimum magnetic bias in the static-crossed field detectors is believed to have increased their sensitivity to optical spot positioning errors. With proper magnetic biasing on the detectors, and a redesign of the receiver optics, the bias errors in the receiver should be reduced to those of the waveform digitizer, which is ±5psec. Such bias errors would permit measurement of the atmospheric delay with an accuracy of 1cm over two-way horizontal paths.

6.1 Photomultiplier Calibration

Calibration of the impulse response and photoelectron levels of the photomultipliers was necessary to permit signal level characterization of the receiver package. The calibration consisted of measuring the impulse response and low level pulse-height distribution of the detectors. The results from the tests were the first indication of the magnetic bias problem in the detectors.

A GaAs laser diode pulser (Hamamatsu C1308) was used as the optical source for both detector tests. This pulser emits a 90 to 100 psec wide pulse at approximately 820 nm, at rates as fast as 10 kHz. The nominal energy per output pulse is 0.1 nJ. This laser was preferred to the mode-locked laser transmitter for these tests, since its amplitude stability and its repetition rate are much higher. For these tests, the pulser output was collimated with an external lens, and it was coupled into the reference path in the optical breadboard at the point of the translating beam steerer. The dichroic beam splitter and bandpass filters in the receiver package also were replaced with ones which passed the 820 nm radiation.

The impulse response of the detector and power splitter combination is shown in Figure 6.1. This was measured by connecting the power splitter output to a fast sampling oscilloscope (HP 1811A with 28 psec risetime), and triggering the pulser at approximately a 5 kHz rate. Figures 6.2 and 6.3 show expanded views of the 355 and 1064 nm impulse responses. From these measurements, the FWHM of the 355 and 1064 nm pulses was found to be 460 and 440 psec. These values are considerably broader than the 130 psec impulse response which has been previously measured for static-crossed field detectors [6.1]. In the previous testing, the cause of such broadening was found to be a change in the magnetic field strength of the permanent magnets in the detectors [6.2].

The pulse height distribution of the detector output was measured by triggering the pulser at a 5 Hz rate, and by connecting the power splitter output to the waveform

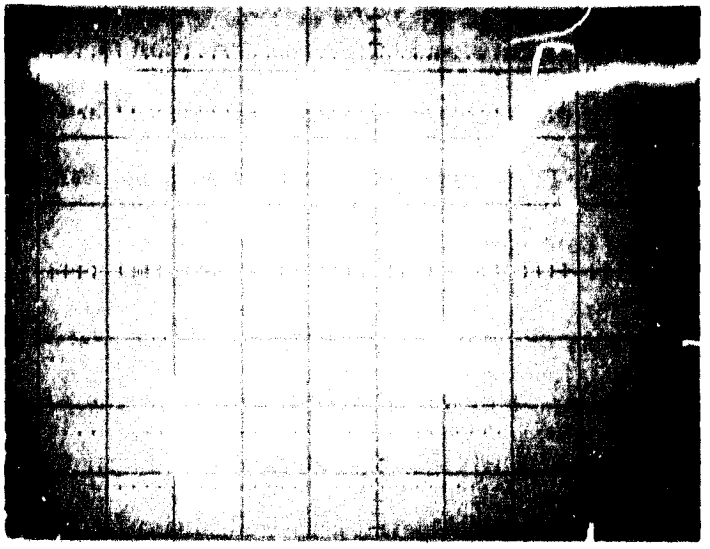

Figure 6.1. Impulse response of detectors and power splitter combination as measured by sampling oscilloscope. The horizontal scale is 500 psec/div.

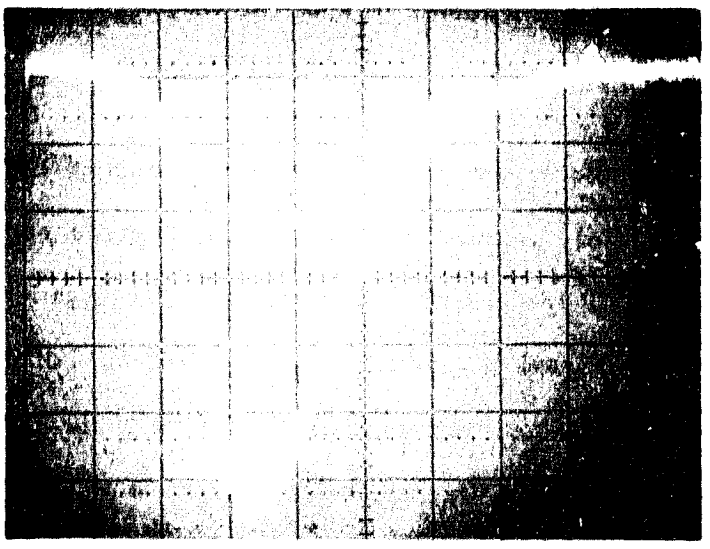

Figure 6.2. Expanded view of 355 nm detector output shown in Fig. 6.1. The horizontal scale is 200 psec/div, and the pulse FWHM is 460 psec.

Figure 6.3. Expanded view of the 1064nm detector output shown in Fig. 6.1. The horizontal scale is 200 psec/div, and the pulse FWHM is 440psec.

digitizer. The digitized waveform output then was analyzed by computer programs which had been previously developed for characterizing GHz bandwidth detectors [6.3].

Figure 6.4 shows the peaked pulse-height and pulse-charge distributions of the 355 nm detector. The figure shows both single and double photoelectron peaks in both histograms. These are similar to those previously measured for static-crossed field detectors [6.1], and are observable due to the high-gain GaP first dynode in the photomultiplier. The most likely single photoelectron voltage and electron gain were measured from this figure to be 4mV and 4.7×10^5.

Figure 6.5 shows similar test data for the 1064 detector. The pulse height and charge distributions were broader for this detector. Such distributions can be caused by improper activation of the GaP first dynode of the detector, which results in both lower dynode gain and a less-peaked photoelectron distribution. From these distributions the single photoelectron voltage and detector gain were estimated to be 11mV and 1.4×10^6, although there is more uncertainty in these values than for the 355nm detector. These voltage and gain values are approximately three times those of the 355nm detector.

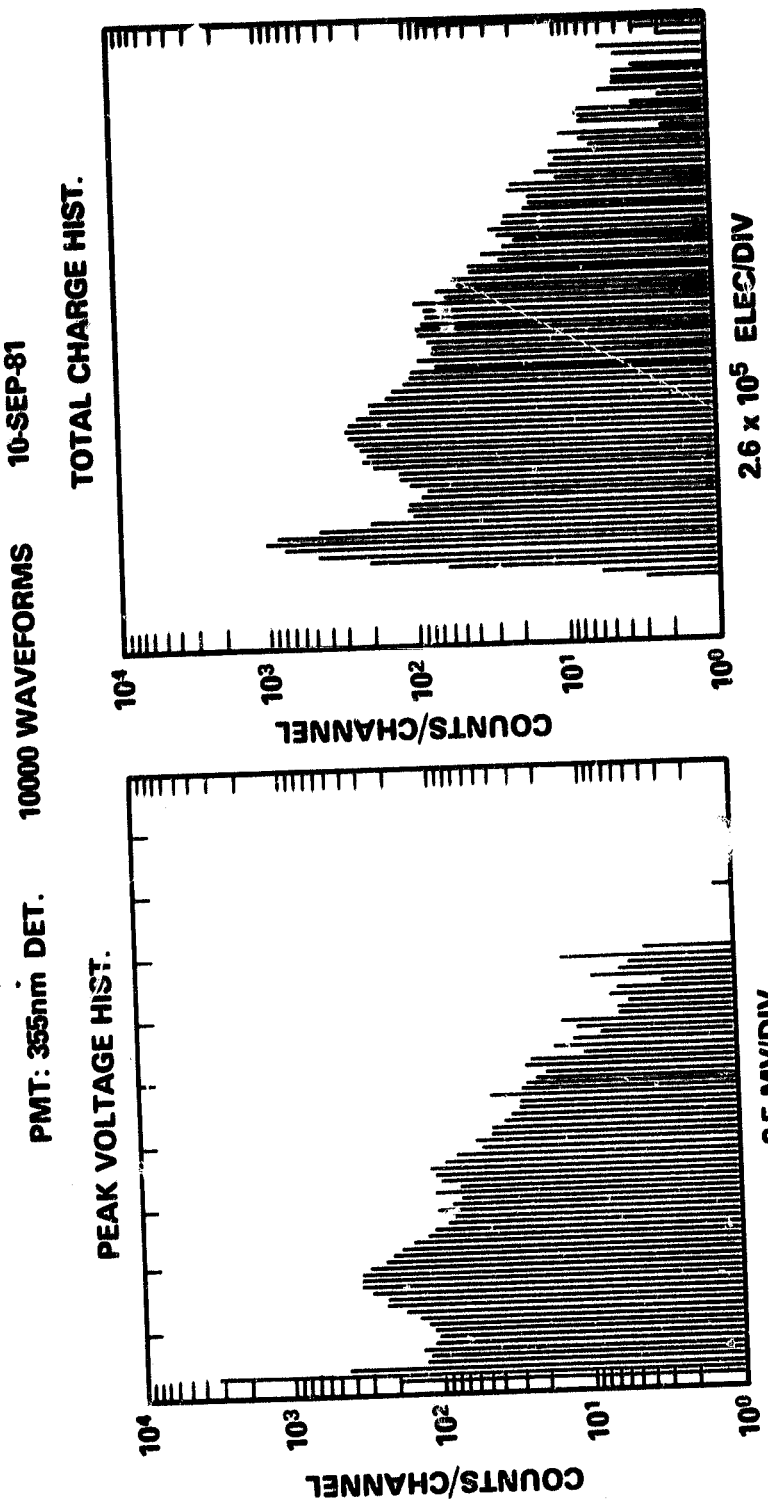

Figure 6.4. Pulse height and pulse charge distributions of the 355 nm detector. The single photoelectron voltage was found to be 4 mV, and the photomultiplier gain to be 4.7×10^5.

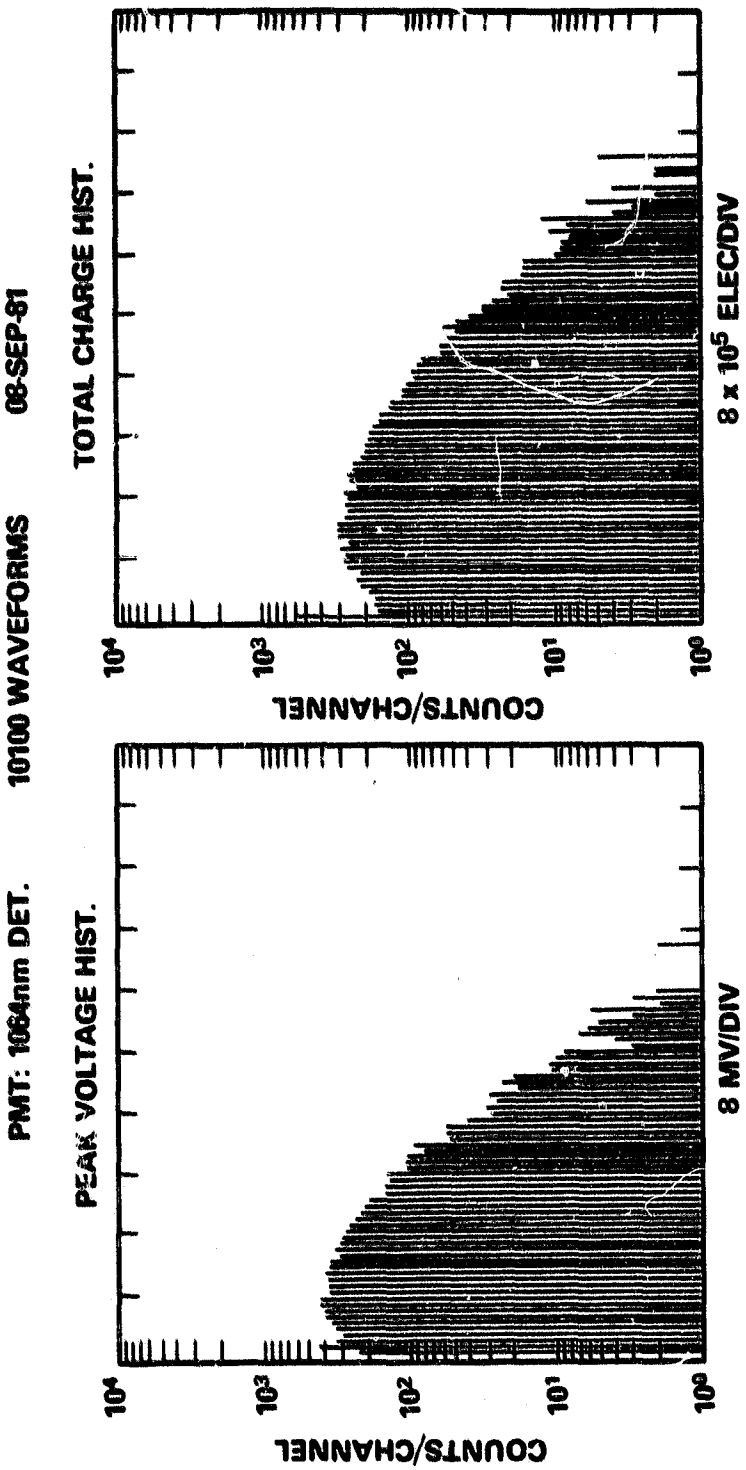

Figure 6.5. Pulse height and pulse charge distribution for the 1064 nm detector. The single photoelectron voltage was estimated to be 11 mV, and the detector gain was 1.4×10^6.

The photoelectron level of both channels in the receiver system was calculated by using this data with the measured system gain. The results of this calibration are shown in Table 6.1. The results show for most of the data sets, the receiver operated with 355 nm optical pulses of 3 to 34 photoelectrons, and with 1064nm pulses of 6 to 63 photoelectrons.

6.2 Waveform Digitizer Timing Performance

The timing stability and resolution of the waveform digitizer were measured to determine their contribution to the total system error. These measurements were performed with an electrical pulse generator, so that the digitizer timing errors could be separated from timing errors contributed by the photomultipliers.

The equipment configuration used for these tests is shown in Figure 6.6. The FWHM of the electrical generator (Avtech AVH-S1) output was approximately 120 psec and the generator was triggered at a nominal 5 Hz rate by an external source. The output pulse was split into two paths by a power splitter, with one path containing an adjustable coaxial delay line. The delay line output and the undelayed splitter output then were summed by a second power splitter. Its output was connected to the waveform digitizer. In the tests, the undelayed pulse was used to simulate the 355 nm detector output, while the delayed pulse simulated

Table 6.1
Photoelectron (pe) Level Calibration of the Prototype Receiver System.
Values are given for the 1064 nm detector operating both with the 6 dB attenuator, which was used in the earlier receiver tests, and with the 20 dB attenuator, which was used in the later receiver tests. Since the distribution of the detector amplitudes is expected to be Poisson, the ratio of the mean value to the standard deviation is equal to the standard deviation.

Signal Level	355 nm (pe)	1064 nm (6 dB) (pe)	1064 nm (20 dB) (pe)
Lower thresh.	3.1	1.1	5.7
Upper thresh.	34	13	63
Mid Level	16	5.7	28
Std. dev. @ mid level	4	2.4	5.3

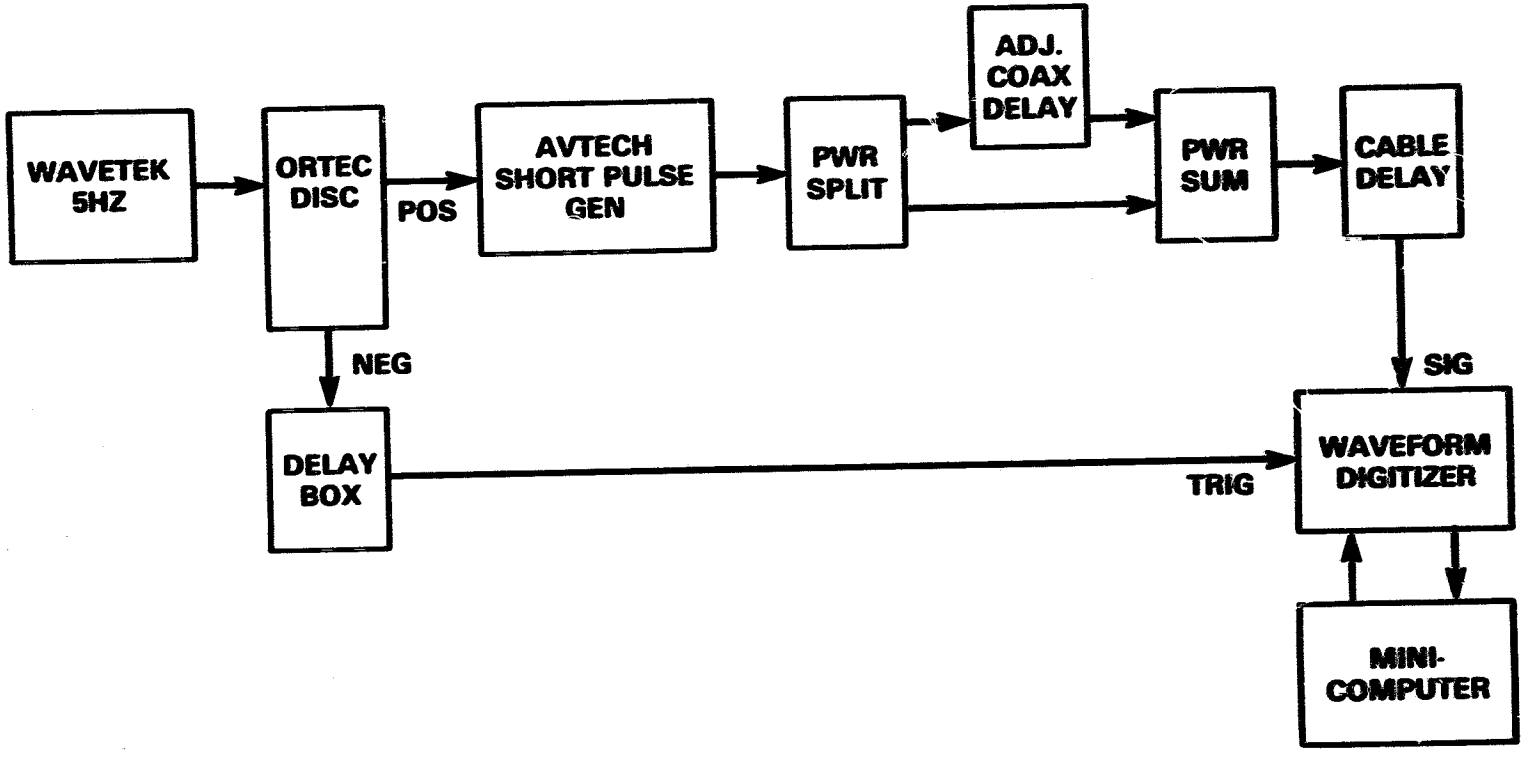

Figure 6.6. Configuration used to measure the timing performance of the waveform digitizer with electrical inputs. The coaxial phase shifter was adjusted to simulate dispersive delay shifts.

output, while the delayed pulse simulated the 1064 nm pulse. The digitizer was externally triggered by the discriminator used to drive the pulse generator. The same computer programs were used to measure the separation time of the pulses in the digitized waveform as were used in the optical pulse timing.

Typical results from the stability test are shown in Figure 6.7. The dashed lines in the figures represent the average values of measured pulse separation time for three different delay line settings. Each point plotted in the figure is the average value of 50 individual measurements taken by the timing program. The figure shows that the waveform digitizer system has a stability of ±5 picoseconds over a time interval of 90 minutes. Changes in the delay line setting also were repeatable within 10 picoseconds over the same 90 minute interval. The standard deviations of the sample means were in the 2 to 3 psec range.

These tests were repeated on the next day, and the mean values between the two days were found to agree within ±5 psec. This result confirmed the stability performance of both the calibration and the pulse timing measurements. The conclusion drawn from these results was that the waveform digitizer measuring system is sufficiently stable over 90 minute periods to permit two-way single color atmospheric delay predictions with an accuracy of 1.5 cm.

6.3 Optical Timing Performance

The photomultipliers next were connected to the system, in order to calibrate the entire receiver. These tests were performed using the laser diode pulser in the same configuration used for the photomultiplier calibration, and included measurement of the amplitude dependence of the optical pulse timing and the stability of the mean timing values versus time. Measurements of the receiver timing jitter also were made as a function of signal level, to permit calibration of the photomultiplier jitter.

The mean signal delay of the photomultipliers and the waveform digitizer combination can be amplitude dependent if either instrument is operating in a slightly saturated region.

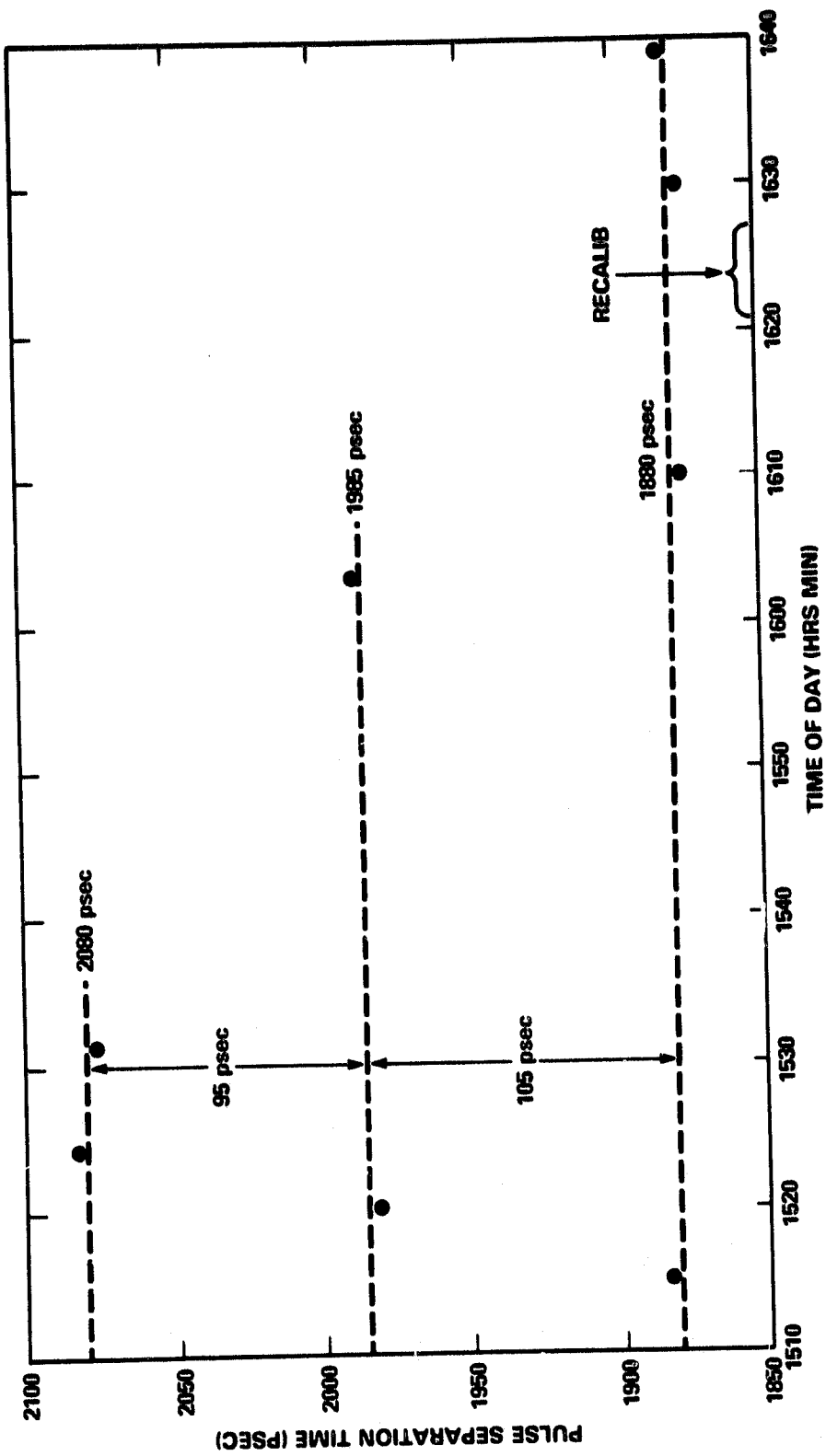

Figure 6.7. Electrical pulse separation times measured by the waveform digitizer in stability tests. The plotted data points are the mean values of 50 individual measurements. The standard deviations of the sample means were 3 psec.

At the beginning of the tests, the photomultiplier outputs were observed versus signal level with the sampling oscilloscope. No amplitude-dependent shift was noticed for either detector. Therefore, any system time-walk was believed to occur in the waveform digitizer.

These time-walks were measured versus peak pulse-height by first fixing the optical signal level on one detector. Then the input signal level of the detector under test was changed with a continuous neutral density wheel during the recording of one set (200 measurements) of waveform digitizer data. The recorded differential delay times next were plotted versus the amplitude of the detector under test, and a polynomial was fitted through the data points. Subsequently, the same test procedure was applied to the other detector in the receiver.

Typical measured time-walk curves for the 355nm channel are shown in Figure 6.8. The plots show a nearly linear time-shift versus amplitude, with an average time-shift of -64psec when the signal amplitude is increased from 0.5 to 5.5 divisions on the waveform digitizer. Since the larger amplitude pulses are delayed more than smaller ones, they are closer to the 1064nm pulses. Therefore the time difference measured between the pulses decreases with the amplitude of the 355nm pulses.

Similar data for the 1064nm channel is shown in Figure 6.9. The time-walk curves measured for this detector channel had an average time-shift of 65psec over the full receiver channel dynamic range. Since the 1064nm pulse follows the 355nm one in the pulse pair, increases in its signal delay increase the time difference between the pulses. Therefore the time-walk values increase with signal level.

Both time-curves were nearly linear and had the same magnitude time shift for full scale amplitude change. Therefore, to correct for this instrumentation characteristic, a linear time-walk compensation with a magnitude of 6.6psec per division was used on subsequent data sets. The sign of the time-walk compensation was positive for the 355nm pulse, and negative for the 1064 pulse.

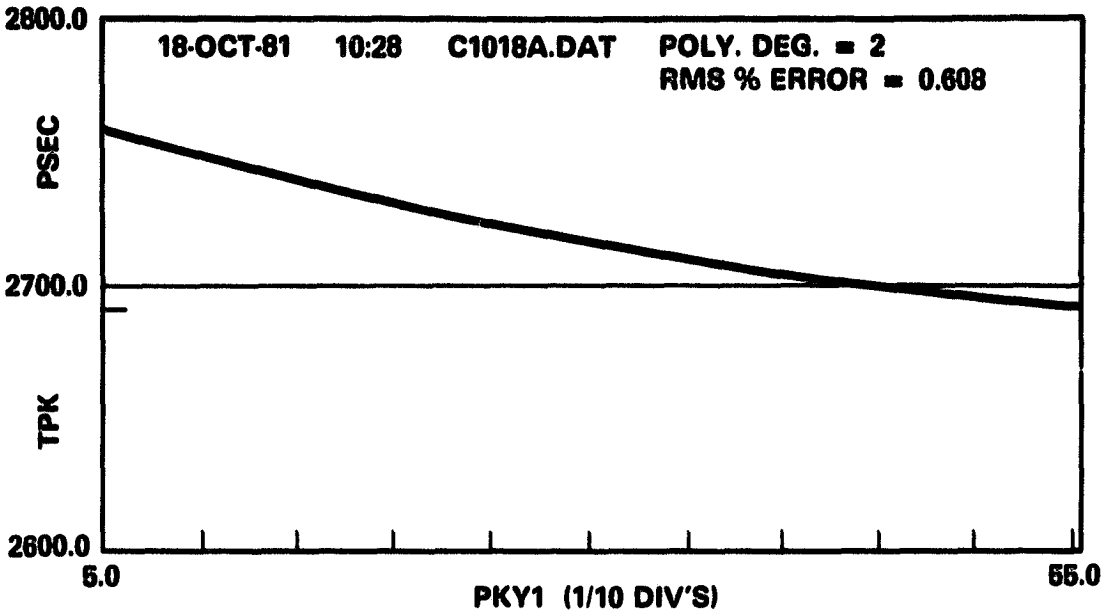

COEFFICIENTS = 2.769E + 03, −2.195E + 00, 1.483E − 02

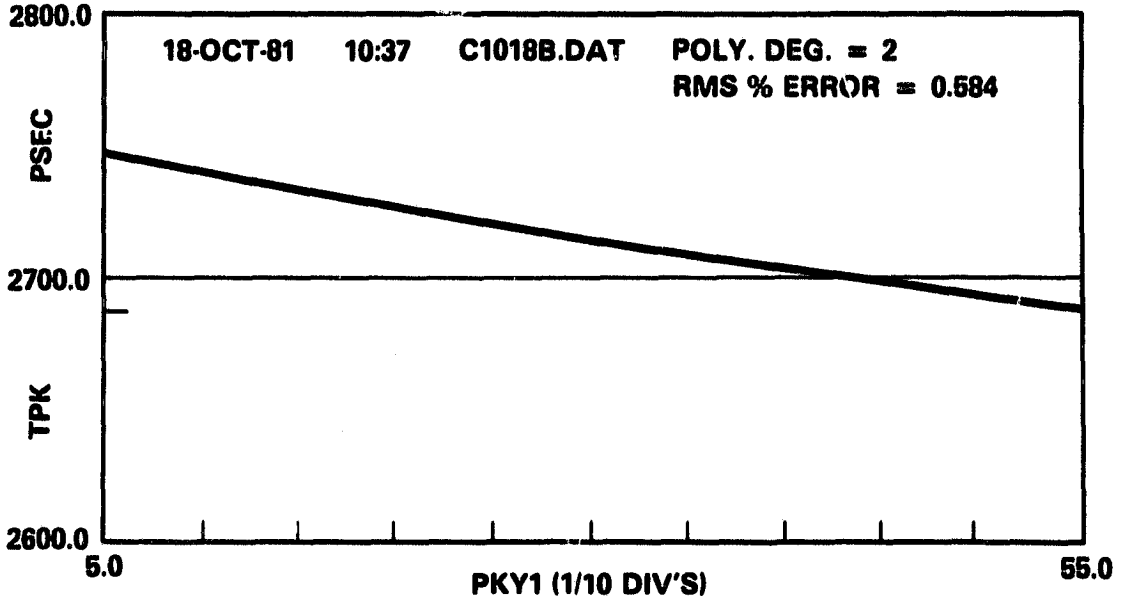

COEFFICIENTS = 2.753E + 03, −1.358E + 00, 3.130E − 03

Figure 6.8. Time shift in the first (355 nm) channel versus amplitude for two successive sets of measurements. Over the 11:1 dynamic range, the receiver time walk was −64 psec.

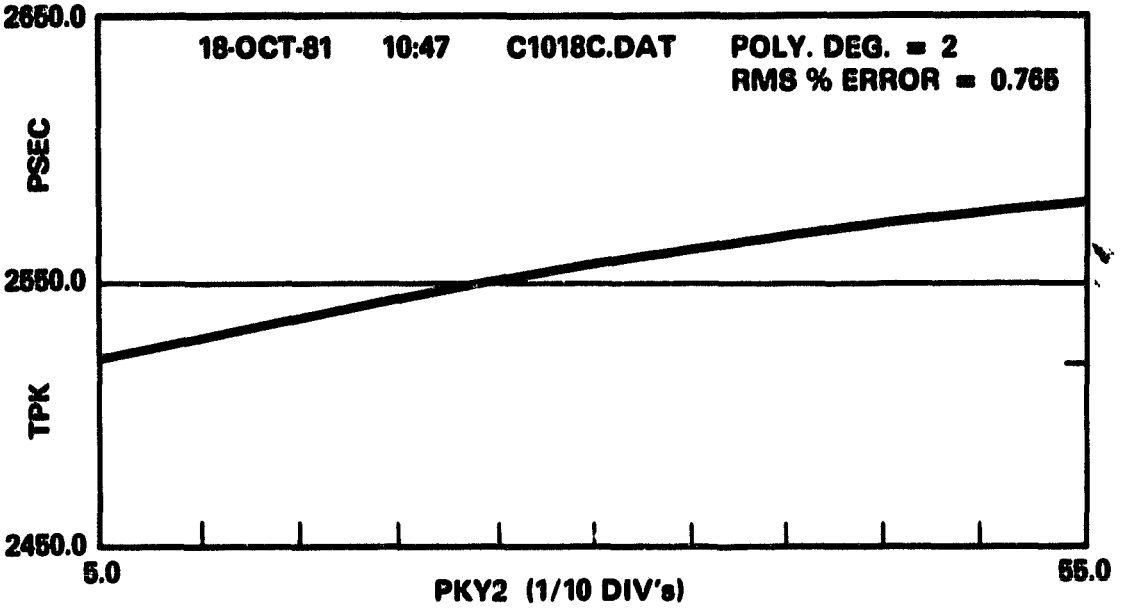

COEFFICIENTS = 2.514E + 03, 1.704E + 00, − 8.031E − 03

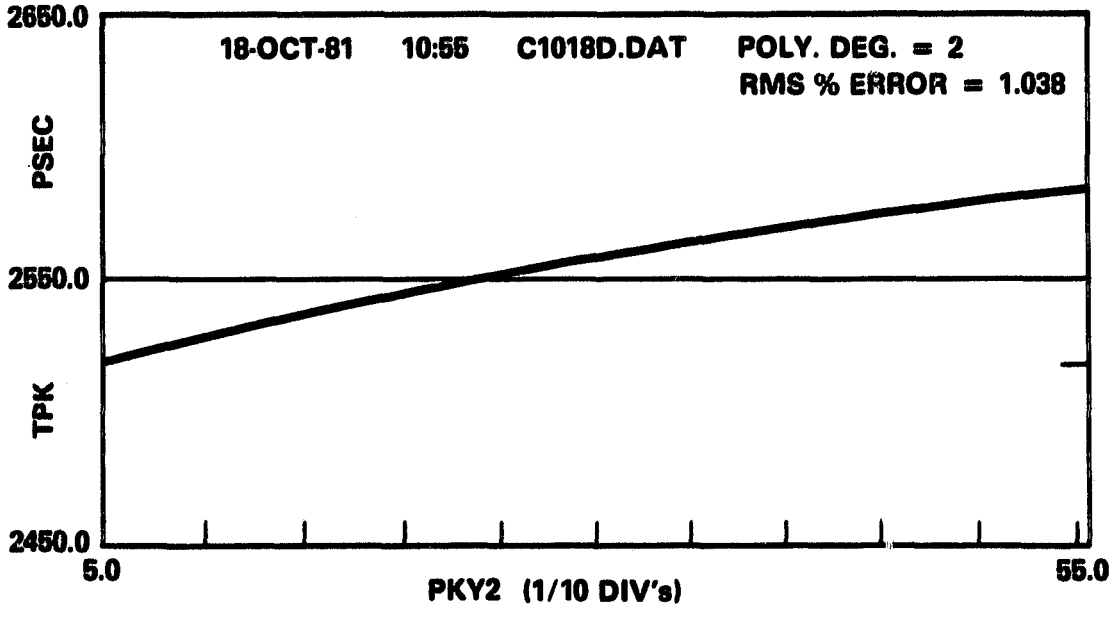

COEFFICIENTS = 2.510E + 03, 1.887E + 00, − 1.029E − 02

Figure 6.9. Two successive time walk calibrations with optical pulsar for 1064 nm detector. Over the 11:1 dynamic range of the receiver the time walk was 65 psec.

The stability of the optical receiver channel was measured by operating the ranging system repetitively in the reference mode. Since the optical path delays are fixed in this configuration, any measured changes in the pulse separation time were caused by changes in the receiver system delays. Several sets of representative data from these tests are shown in Figure 6.10, where the measured reference delay was plotted versus the time-of-day when the data set was taken. The error bars around the data points are plus and minus one standard deviation of the plotted sample mean value. Several of the data sets show 25 psec changes in the pulse separation time over 40 minute time intervals. During other periods, the data shows much smaller drift rates. Since the waveform digitizer drift was much smaller over this time period, the delay shifts measured were due to changes in the detector signal delays. These changes could have been caused either by slow voltage drifts in the detector supplies, or by temperature changes in the laboratory.

The rms fluctuations in the photomultiplier delays were calculated from measured values of the system timing jitter. For these tests, the laser diode pulser also was used as the optical source. In Chapter 5, the total timing jitter of a measurement was shown to be the sum of the jitters of both receiver channels plus that contributed by the digitizer itself. The derivation showed that if the jitters of both receiver channels were equal, and that of the digitizer was known, then the photomultiplier jitter could be calculated from the measured system jitter. For these calculations, the system jitter must be measured as a function of photoelectron level in each detector. Also, the width of the optical test pulse must be known, so that the jitter of an ideal detector can be calculated.

For the calculations used for this measurement, however, the equivalent photoelectron number derived in Chapter 5 was not calculated for each individual measurement. Instead the average photoelectron number for each channel was computed for each data set, and the equivalent photoelectron number was computed from this average. This approximate calculation is accurate for signal level fluctuations which are small relative

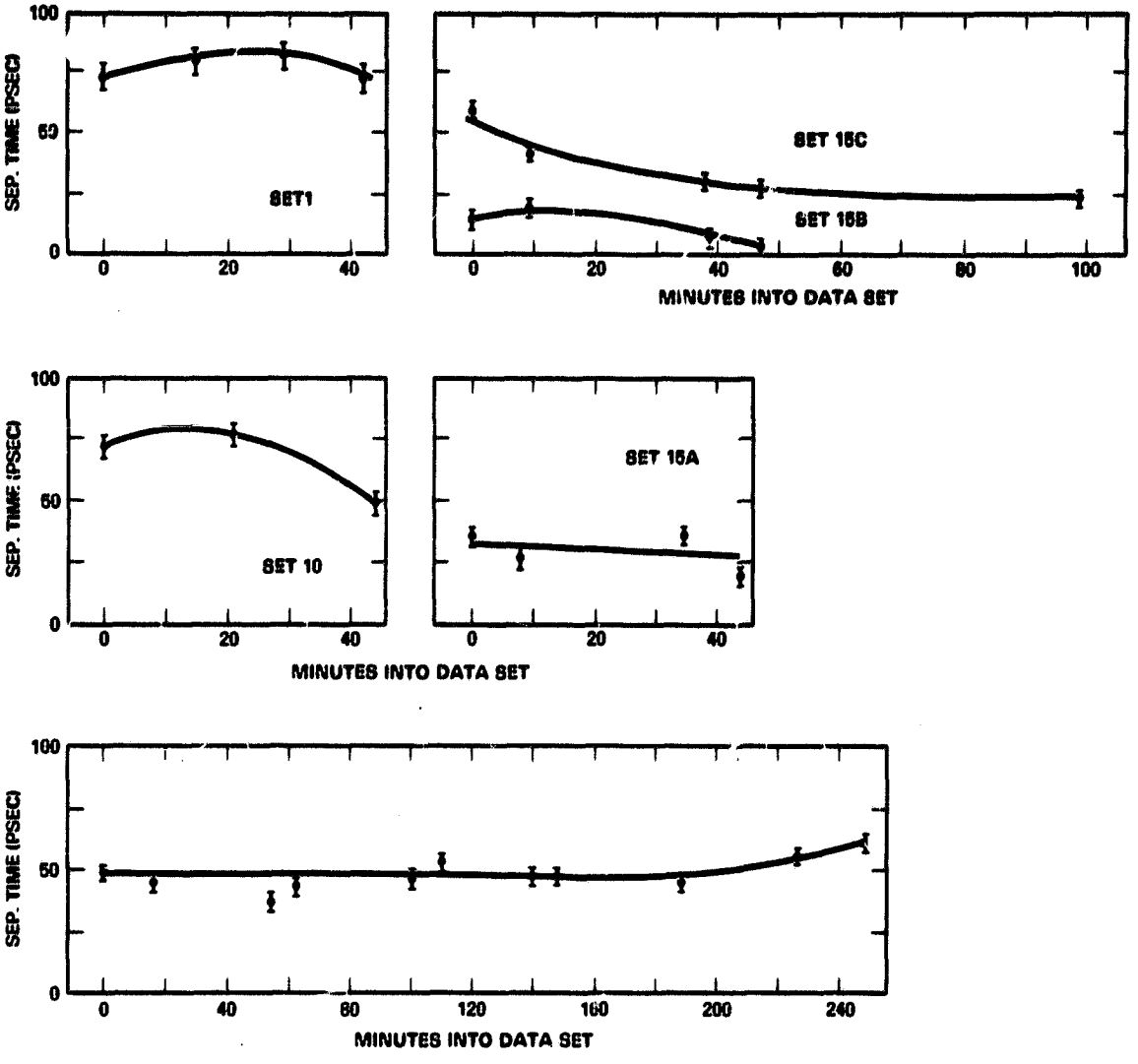

Figure 6.10. Plots of measured changes in the mean optical pulse separation time versus elapsed time in the data run. Each point represents the mean value of approximately 200 measurements, and the error bars are plus and minus one standard deviation about the sample mean.

to the mean signal value. Since the measured average signal levels extended as low as 4 photoelectrons, the approximation was not as accurate for the low level measurements. However, it was adequate for the majority of the data points, which were above the 10 photoelectron level.

A plot of the measured signal-dependent timing variance versus the average equivalent photoelectron number is shown in Figure 6.11. Some of the scatter in the data points for the lowest signals is due to the approximation mentioned above. The standard deviation of photomultiplier timing jitter was calculated from this curve to be 100 psec at the single photoelectron level. The linear decrease of the jitter values with the equivalent photoelectron in the figure verifies the system timing jitter formulas derived in Chapter 5.

The magnitude of the single photoelectron detector time jitter is approximately 2.5 times larger than earlier measurements [6.1] for static crossed-field detectors. The most likely cause of this increase also was the suboptimum magnetic-field bias on the detectors. This condition would allow the electrons emerging from the photocathode to follow more widely separated trajectories for each pulse. These then would broaden the detector impulse response and cause an increase in timing jitter above the detectors nominal values.

The rms timing jitter for the dispersion measurement can be computed by using the formulas developed in Chapter 5 with the computed value for $\mathrm{Var}(\tau_p)$ and the measured values for $\mathrm{Var}(\tau_d)$ and $\mathrm{Var}(\tau_{PM})$. For optical signals centered in the receiver's dynamic range, Q = 10. The single measurement rms time jitter computed by using (5.14) and (5.18) for this signal level is 36 psec. For averaging 200 measurements, the rms jitter of the average is reduced to 2.6 psec.

6.4 Horizontal Path Test Results

The prototype system was tested over the three horizontal paths listed in Chapter 4. These tests were performed in order to verify the system operation and to assess the magnitude of the system biases. For these tests, the reference and the atmospheric path

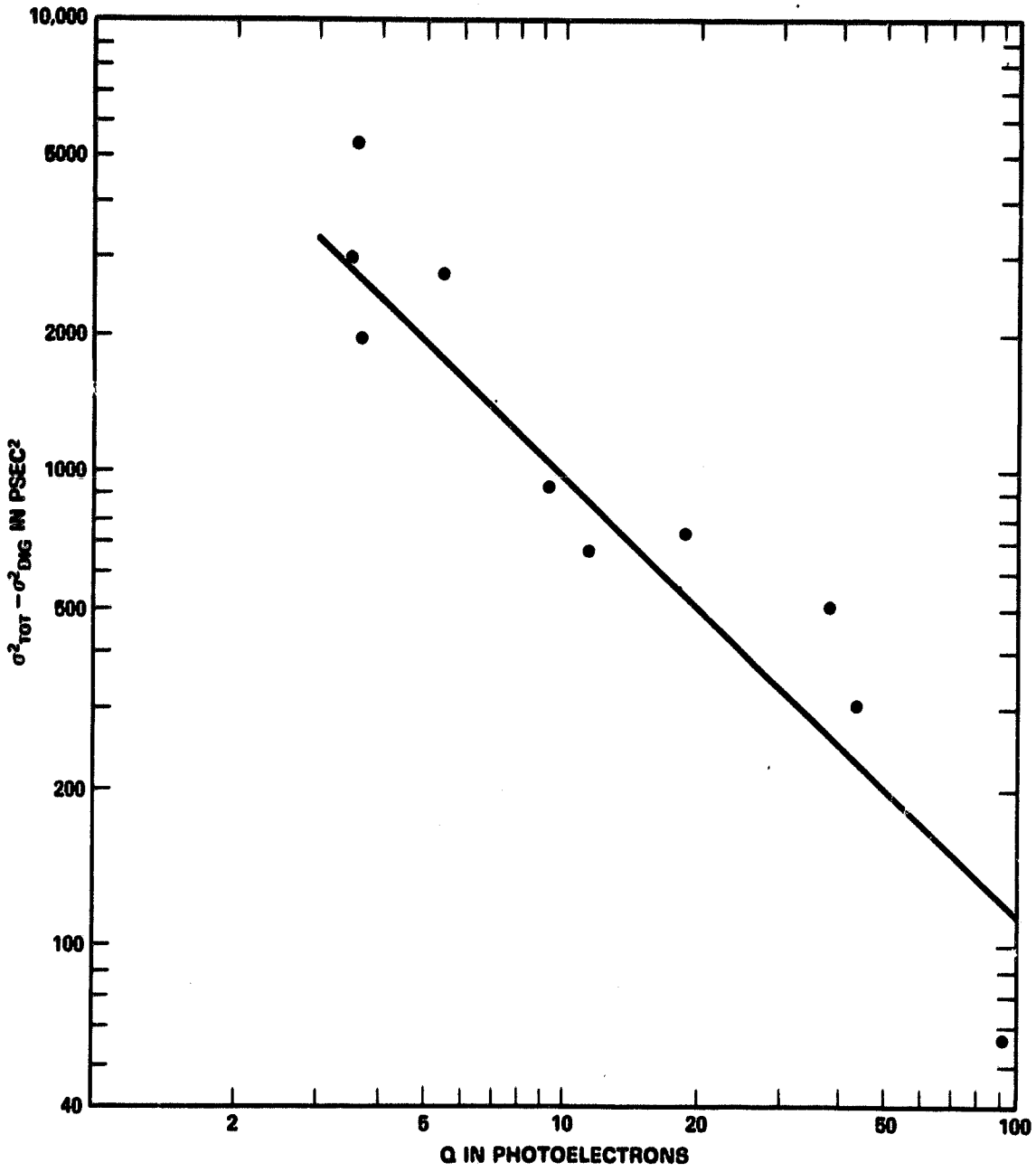

Figure 6.11. Plot of photoelectron dependent timing variance versus equivalent average photoelectron number. The data points are values obtained from tests with the laser diode pulsar, and the straight line is the best fit through the points.

measurement sets were taken in close succession. The theory developed in Chapter 5 shows that the difference between the average measured pulse separation times was the sum of the atmospheric path dispersion and changes in the instrumentation delays (instrumentation biases).

In order to estimate the instrumentation biases, measurements of the atmospheric pressure, temperature and relative humidity were made at the path endpoint nearest to the system's periscope mirror during the ranging measurements. When necessary, the pressure reading was extrapolated upward or downward by using a pressure lapse rate of -0.12 mbar/m, so that it would correspond to the pressure at the midpoint of the slant path. These meteorological values then were substituted into the group refractivity formula given in Chapter 2. The resulting values were used with the measured 532 nm path delay to predict the differential dispersive delay. The formulas used were

$$L = cT_2 \, [1 - r_{g2}(0)]$$

and

$$\Delta T_{31} = (L/c) \, \Delta r_{g31}(0),$$

where T_2 is the measured 532 nm delay, and $r_{gi}(0)$ is the endpoint group refractivity at wavelength i.

Over the horizontal paths used for the tests, systematic errors in the meteorological measurements contributed only a small error to the dispersion prediction. A typical temperature error of 1°C results in an error of 1 part in 300 of the dispersive delay. Over the longest path used, this error causes a dispersive delay error of slightly less than 2 psec. A worst-case barometric pressure error of 2 mbar causes a dispersive delay error of approximately 1 part in 500. An error of 50% in relative humidity causes a dispersion error of 1 part in 1400. Since this error was so small, a constant value of 50% relative humidity was assumed in the calculations. Therefore, meteorological sensor errors would have been significant only if a more accurate instrument was being tested or much longer test paths were used.

Table 6.2
Measured Instrument Performance Over the Rooftop Calibration Path. The mean difference and instrument bias values are plus and minus one standard deviation of the mean difference measurement, and the horizontal bars separate measurement sets made on different days. The larger bias values on the first and last days are believed to be caused by misplaced optical beam positioning on the 1064nm detector assembly.

Time of Day (Hrs:Min)	Mean Ref. (psec)	Mean Path (psec)	Mean Diff. (psec)	Pred. Diff. (psec)	Bias (psec)
9:44	2068	2062	6 ± 5	24	-18 ± 5
10:12	2065	2072	-7 ± 6	24	-31 ± 6
13:40	2071	2049	22 ± 5	23	-1 ± 5
13:55	2076	2057	19 ± 6	23	-4 ± 6
14:20	2049	2012	37 ± 5	23	11 ± 5
9:00	2035	2028	7 ± 6	24	-17 ± 6
9:10	2026	2033	-7 ± 5	24	-31 ± 5
9:35	2036	2027	9 ± 6	24	-15 ± 6
9:45	2019	2040	-21 ± 6	24	-45 ± 6

Test results for the shortest calibration path are given in Table 6.2. The results show the instrument readings were biased by as much as -45 psec relative to the dispersion predicted from endpoint meteorological measurements. However, the values for the second day of the data set showed smaller instrument biases of up to 11 psec. The optical spot position on the 1064nm detector had been adjusted between these two data sets.

Similar results for the short atmospheric path are shown in Table 6.3. Here values for the first day also contained large biases, while subsequent biases were much smaller. The optical beam position in the receiver assembly also had been adjusted between these two data sets. The difference between the bias values suggests that the delay in the system's photomultipliers is sensitive to the optical spot position. This increased sensitivity probably was caused by the suboptimum magnetic field conditions in the detectors which were mentioned earlier.

Table 6.3
Measured Instrument Performance Over the Short Atmospheric Path. The mean difference and instrument bias values are plus and minus one standard deviation of the mean difference measurement, and the horizontal bars separate measurement sets made on two different days. The large bias values on the first day are believed to be caused by misplaced optical beam positioning on the 1064 nm detector assembly.

Time of Day (Hrs:Min)	Mean Ref. (psec)	Mean Path (psec)	Mean Diff. (psec)	Pred. Diff. (psec)	Bias (psec)
11:01	2015	1950	65 ± 6	112	-47 ± 6
11:12	2019	1951	68 ± 6	112	-44 ± 6
11:40	2007	1977	30 ± 7	112	-82 ± 7
11:50	2004	1974	30 ± 7	112	-82 ± 7
15:30	2059	1961	98 ± 5	113	-15 ± 5
15:40	2042	1946	96 ± 5	113	-17 ± 5
16:20	2031	1917	113 ± 5	113	0 ± 5
16:29	2029	1924	105 ± 5	113	-8 ± 5

The reference and slant path data taken on a subsequent day for the short atmospheric path is plotted versus time-of-day in Figure 6.12. The reference values show good instrument stability until near the end of the measurement period. Just before the data values started increasing, the building air conditioning was turned off. Therefore the ensuing rise in room temperature probably was responsible for the change.

The path timing data shows a nearly cyclical change in the differential delay values. The dispersion value measured half way through the data set was 110 psec, while the value predicted from endpoint measurements was 116 psec. Therefore during this time period the instrument was nearly unbiased.

The changes in the measured tower delay values near the end of the day probably were caused by changes in the temperature lapse rate near dusk. These change the atmospheric beam curvature as was discussed in Chapter 3. In turn, this causes the position of the target corner reflector image on the detector photocathode to move. Since the

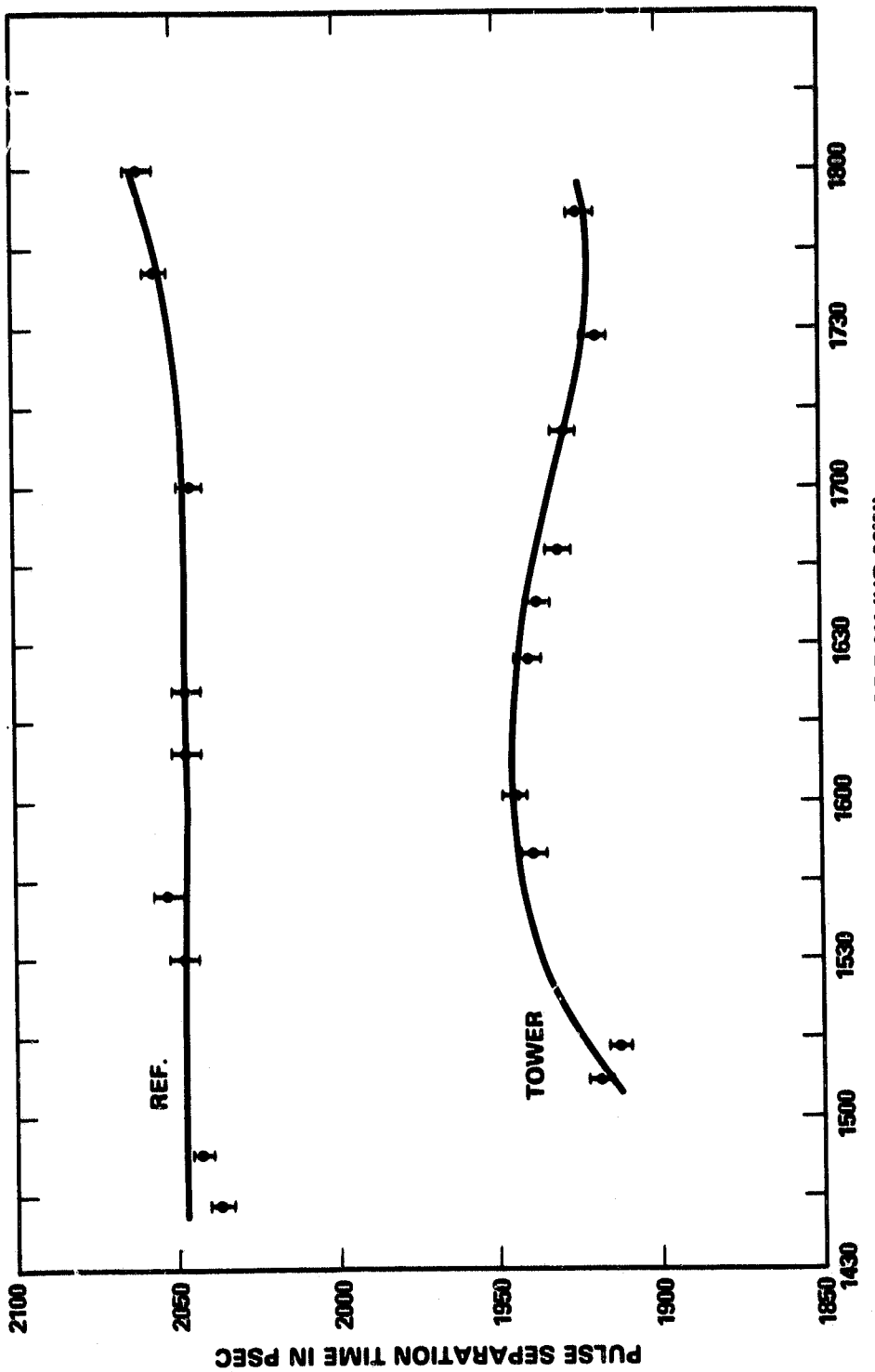

Figure 6.12. Plot of measured pulse separation times over reference and short atmospheric paths versus time of day. The fluctuations in the atmospheric path separation times were most likely caused by the optical beam shifts photodetector, and not by atmospheric changes. The average of the mean measured difference in separation times is 110 psec for the center part of the data set, while the dispersion value calculated for the path from end point meteorological measurements was 116 psec.

photomultiplier delay was found to be sensitive to the optical spot position, this would result in changes in the receiver delay.

Measurements of the dispersive delay over the long atmospheric path are summarized in Table 6.4. These measurements were made using an earlier computer program which timed to the 50% risetime points rather than to the peaks of the pulses. During the earlier system development stage, this detection strategy performed more accurately than peak detection. Subsequent development work improved the peak detection accuracy to beyond the 50% risetime level. Unfortunately, in the interim period, the retroreflector mounted on the water tower was stolen. Therefore, the data given will have to stand as the best data available for this path.

The measurements show that the values of the instrument biases over this path were roughly equal to the average bias magnitude for the outer paths. Therefore, to within the measurement accuracy, the observed system bias levels did not depend on the path length. This finding gives further support to the hypothesis that the bias errors observed were caused by additive receiver timing biases.

Table 6.4
Measured Instrument Performance Over the Long Atmospheric Path. The mean difference and instrument bias values are plus and minus one standard deviation of the mean difference measurement, and the horizontal bars separate measurement sets made on different days. The biases in the values are believed to be caused by misplaced optical beam positioning on the 1064 nm detector assembly. These values were measured earlier in the system development and are for 50% risetime detection timing.

Time of Day (Hrs:Min)	Mean Ref. (psec)	Mean Path (psec)	Mean Diff. (psec)	Pred. Diff. (psec)	Bias (psec)
15:45	2563	1983	580 ± 4	570 ± 2	10 ± 4
17:30	2462	1874	588 ± 6	600 ± 2	-12 ± 6
15:35	2105	1562	543 ± 11	582 ± 2	-39 ± 11
15:50	2101	1539	562 ± 9	582 ± 2	-20 ± 9

Chapter 6 References

6.1 J. B. Abshire and H. E. Rowe, "Characterization of Gigahertz Bandwidth Photomultipliers," NASA Technical Memorandum 78028, Dec. 1977.

6.2 R. Klein, Varian - LSE Division, private communication, Jan. 1982.

6.3 J. B. Abshire and H. E. Rowe, "Systems for Measuring the Response Statistics of Gigahertz Bandwidth Photomultipliers," NASA Technical Memorandum 78029, Dec. 1977.

CHAPTER 7

DISCUSSION AND CONCLUSIONS

In this dissertation, a pulsed multiwavelength system for measuring atmospheric delay has been described, and its performance limits have been calculated. A prototype system also was constructed and its performance was measured over short horizontal paths. These tests were used to quantify the theory of instrument performance and to investigate the current technological limits in measuring atmospheric delay with such a system.

7.1 Summary and Conclusions

The physical principles underlying the refraction of gases were reviewed first. The resulting Lorentz-Lorenz equation expressed the functional relationship between the refractivity and the gas density. The derivation also showed that the electromagnetic wave incident into the gas was extinguished inside it and was replaced by a wave traveling with a phase velocity c/n. These results then were extended to review the refractive properties of mixtures. The resulting equations were evaluated with measured densities and refractivities of the gases which compose air in order to compute its refractive index. Finally, this equation was used to derive the formula for the group refractive index of air. The result was accurate to a few parts in 10^9, which is more than sufficient for multiwavelength ranging systems.

The measurement theories for single and multiple wavelength ranging systems operating over horizontal paths were derived next. The performance of both single and multicolor systems was shown to be limited by both path curvature and atmospheric turbulence. The path curvature errors were shown to be bias errors, and increase with the cube of the target distance. Turbulence was shown to cause random fluctuations in the measured single color range, and in the atmospheric correction measured by multicolor systems. Its rms level was shown to increase with the square-root of the target distance.

The dominant error source in single wavelength systems was shown to be the error in estimating the integrated path air densities. Path curvature was shown to limit performance only over paths with long lengths and with large temperature lapse rates.

Optical three color systems were shown to be capable of measuring both the wet and the dry atmospheric delay. However, they also were shown to require the most accurate differential path length measurements. For the wavelengths of the prototype system, the required differential path length accuracy was shown to be 240 times the single color ranging accuracy. Ranging with two colors was shown to be sufficient for measuring the dry part of the atmospheric delay, but it requires the integrated path water vapor to be estimated by an endpoint measurement. Although this technique was shown to be susceptible to water vapor estimation errors, it requires less accurate differential path measurements (7.5 times the single color accuracy) than the three-color system. The atmospheric turbulence was shown to cause fluctuations in the refractive correction in multicolor systems, since the spatially separated beams of each color can traverse regions of independent turbulence.

A prototype pulsed multicolor ranging system was constructed as part of this research. The transmitter was a modelocked ND:YAG laser, and was equipped with a frequency doubler and tripler. Since only the 355 and 1064nm output pulses were used for measuring the atmospheric dispersion, the system used the two-color technique. The dispersive delay was measured by using two static crossed-field photomultipliers connected to a waveform digitizer. The path length at 532nm was measured by a photodiode, a third static-crossed field detector, and a time-interval-unit. The data from the digitizer and the time-interval-unit were collected and processed by a minicomputer connected to the receiver electronics. Special calibration and timing programs were developed and used to compensate for the nonuniformities in the digitizer sweep-speed and amplitude response.

Next, the ideal receiver timing accuracy for a single laser firing was derived. The rms timing accuracy was shown to be directly proportional to the laser pulse width and

inversely proportional to the square root of the equivalent received photoelectron number. This limit and those imposed by the atmosphere itself are the fundamental ones when measuring the atmospheric delay with pulsed multicolor ranging systems.

The additional timing biases and jitters from the photomultipliers and external timing equipment of the prototype system were shown to increase the timing errors above the theoretical limit. These single measurement results then were extended for observation sets which were the average of many single measurements. Subsequently, the accuracy of estimating the atmospheric delay from the mean difference between the reference and atmospheric path delay data sets was calculated. This measurement technique was used in the prototype system. The results showed that the rms jitter of the mean delay estimate was inversely proportional to the square root of the number of data points averaged. However, the measurement biases were not reduced by averaging. Therefore, identification and reduction of the biases was the most important part of the system calibration.

Link calculations showed that the maximum range of the prototype system was limited to 25 km by the atmospheric and mirror transmission losses in the 355 nm channel. Further calculations gave typical detection and false alarm probabilities of the prototype system. The finite probability of missing a measurement was shown to limit the rate at which measurements can be made under weak signal or heavily turbulent conditions.

Performance measurements of the prototype system were presented last. They showed that the photomultiplier jitter was 100 psec at the single photoelectron level, which was three times larger than expected. Suboptimum magnetic-field conditions within the detectors were postulated as the most likely cause of this effect. The theoretical model for the system's timing jitter was confirmed by making measurements at several photoelectron levels. The mean photomultiplier signal delay also was found to be sensitive to the optical spot position on the photocathode. This was found to cause bias errors as large as 80 psec in the dispersion measurements.

When the optical spot position was more accurately controlled, the system bias errors reduced to the 10 to 15 psec range. These biases cause atmospheric delay estimation errors at the 2 cm level in the prototype system. Correction of the detector problem should permit reduction of the bias errors to ±5 psec, which is the residual bias level of the waveform digitizer. Such errors would permit the atmospheric correction to be made at slightly better than the 1 cm level.

7.2 Suggestions for Future Work

Several topics in both the theoretical and experimental areas should be investigated further. The theory of horizontal path optical ranging should be extended to include both diffraction and multipath effects. Multipath effects are commonly observed when viewing images through heavy turbulence. In general, the lengths of the multiple paths will not be equal, and this will cause further degradation of ranging accuracy.

The theory of the instrument performance and the experimental work presented here were concentrated on the horizontal path ranging performance. Once the prototype system is sufficiently accurate, it should be used to verify the ranging theory given in Chapter 3. This could be done by making single color ranging measurements over various path lengths, and under different temperature lapse rates and levels of atmospheric turbulence. Simultaneous measurements of differential delay, pulse amplitude statistics, and angle-of-arrival should allow the atmospheric delay, the turbulence strengths, and the changes in path curvature to be calculated. Comparison between changes in these values with the measured range should permit verification of the ranging theory.

Additionally, the theory describing the prototype system's performance should be extended to include an exact calculation of the jointly-distributed detection probabilities in the dispersion measurement channel. Such an extension also should include the effects of the pulse-to-pulse energy fluctuations at each transmitter wavelength. Since the shorter

wavelength pulses are produced from the 1064 nm pulse via nonlinear processes, the intensity statistics of the different wavelength transmitter pulses should be partially correlated.

Several design changes also should be made in the prototype system. The detector magnetic-bias problem should be corrected. This would decrease both the timing jitter and the bias contributed by the detectors to the dispersion measurement. Also, it should substantially decrease the photomultiplier's sensitivity to optical spot positioning. Redesigning the receiver optics to permit more frequent monitoring of the alignment between the reference and return optical paths should further reduce the magnitude of the receiver bias. Replacing the aluminized mirrors with dielectrically coated ones which are optimized for 355 nm also should enhance the system's maximum range.

Finally, the optical magnification in the receiver should be reduced. A lower magnification will reduce the optical spot movement on the photomultipliers caused by changes in the apparent target position. This will minimize changes in the detector delay caused by changes in atmospheric bending or by actual target motions.